UCC

University College Cork, Ireland
Coláiste na hOllscoile Corcaigh

Simulated Wave Hydrodynamics and Loading on an Offshore Monopile

UCC
Coláiste na hOllscoile Corcaigh, Éire
University College Cork, Ireland

A Dissertation Presented

by

Ariel J. Edesess

for the degree of

Doctor of Philosophy

in

Civil and Environmental Engineering

University College, Cork

Head of School: Prof. Liam Marnane

Supervisors:

Dr. Denis Kelliher, Prof. Alistair G. L. Borthwick,
Dr. Gareth P. Thomas

August 2018

Thesis Declaration

This is to certify that the work I am submitting is my own and has not been submitted for another degree, either at University College Cork or elsewhere. All external references and sources are clearly acknowledged and identified within the contents. I have read and understood the regulations of University College Cork concerning plagiarism.

Signed:

_____

Date:

_____

Acknowledgements

If people do not believe that mathematics is simple, it is only because

they do not realize how complicated life is.

- John von Neumann

Dissemination of Research

Published

- A. J. Edesess, D. Kelliher, A. G. L. Borthwick and G. P. Thomas. Improving global accessibility to offshore wind power through decreased operations and maintenance costs: a hydrodynamic analysis. *Energy Procedia: 2017 International Conference on Alternative Energy in Developing Countries (AEDCEE)* 138: 1055–1060, October 2017. doi: doi/10.1016/j.egypro.2017.10.107

- A. J. Edesess, D. Kelliher, A. G. L. Borthwick, G. P. Thomas. Offshore monopile in the southern North Sea: Part 1, calibrated input sea state. *Proceedings of the Institution of Civil Engineers - Maritime Engineering*, 170(3+4):122–132, 2017. doi: doi/10.1680/jmaen.2017.14

Accepted for Publication

- A. J. Edesess, D. Kelliher, A. G. L. Borthwick, G. P. Thomas. Offshore monopile in the southern North Sea: Part 2, simulated hydrodynamics and loading. *Proceedings of the Institution of Civil Engineers - Maritime Engineering.* 2018.

Selection of Oral Presentations

- "Improving Global Accessibility to Offshore Wind Power through Decreased Operations & Maintenance Costs: A hydrodynamic analysis". Presented at the 17th International Conference on Alter-

native Energy in Developing Countries and Emerging Economies (AEDCEE), Bangkok, Thailand. 25-26 May 2017

- "OpenFOAM simulations of irregular waves and free surface effects around a monopile offshore wind turbine". Presented at the UK-Ireland OpenFOAM User Meeting. Dublin, Ireland, 16-17 January 2017

- "Offshore wind farm maintenance operations: Analysis of free surface flow around a surface-piercing monopile". Presented at MaREI Symposium, Galway, Ireland. 1 November 2016.

- "Maintenance of Offshore Wind Farms: Crew Transfer Vessel Motion Analysis". Presented at EDF Renewables R&D Offshore Wind; London, United Kingdom. 5 August 2016.

- "Maintenance of Offshore Wind Farms: Crew Transfer Vessel Motion Analysis"; presented at the National Wind Technology Centre, National Renewable Energy Laboratory; Louisville, Colorado, USA. 27 July 2016.

- "Maintenance of Offshore Wind Farms: Crew Transfer Vessel Motion Analysis"; presented at the 11th OpenFOAM Workshop; Guimarães, Portugal. 26-30 June 2016.

- "Crew Transfer Vessel Motion Analysis: Maintenance of offshore wind farms". Presented at the VI International Conference on Computational Methods in Marine Engineering - Marine 2015; Rome, Italy. 15-17 June 2015.

Abstract

Maintenance costs of offshore wind power, where fixed monopile support columns make up the majority of wind turbine types, are up to three times higher than those associated with onshore wind power. High costs are exacerbated by difficulties accessing the turbines in their marine environment. Safe transfer by crew transfer vessel (CTV) requires prediction of vessel motion whilst in contact with the turbine monopile. Future vessel motion prediction first requires analysis through analytical and numerical methods of the local hydrodynamic wave field and wave loading on the monpile turbine in ocean waves.

A location-dependent unidirectional sea state is represented by superposition of periodic waves with amplitude components a_n, obtained from the spectral distribution of free surface displacement data from a single wave buoy located at the Teesside Offshore Wind Farm in the southern North Sea. Wave buoy data was obtained for each season during the 2015/2016 time period, providing a record of seasonal changes that occur in the spectral distribution. Wave loading in the local irregular sea state was predicted using the Morison equation and the linear diffraction formulation. Numerical predictions were obtained using OpenFOAM and a modification of the multiphase *interFoam* solver for generating free surface waves, where a boundary condition for inputting irregular waves based on the local wave spectra was developed for the purpose of this thesis.

For unimodal spectral distributions, which occur in 50% of the data sets with a third data set displaying a small secondary peak, the analytical solutions for the diffracted hydrodynamics and wave loading show

satisfactory agreement with the numerical predictions, provided a slip boundary condition is applied on the cylinder. Comparisons were made between analytical solutions and numerical predictions for each of the four data sets, where the irregular wave field was simulated first in a numerical wave tank and then interacting with a fixed cylinder representative of a monopile wind turbine. Simulations were run using both a slip and non-slip cylinder wall boundary conditions in order to determine the effects of viscosity.

OpenFOAM can potentially provide better predictions of the diffracted water particle kinematics resulting from the interaction between the sea state at Teesside Offshore Wind Farm and the turbine monopiles, but with a significantly increased computational overhead. The analytical solutions provide satisfactory and relatively fast solutions, although at the expense of neglecting higher-order terms. Both methods presented in this thesis provide practitioners with enhanced knowledge of the season-specific local hydrodynamics and wave loading based on actual sea state data, rather than relying on a parametric location-specific representation. Enhanced knowledge of the hydrodynamic field affecting vessel motion will give a better prediction of vessel motion under operating conditions, and eventual determination of the limiting conditions under which the vessel will remain steady.

Contents

List of Figures

xiv

List of Tables

Nomenclature

α Scalar field fluid volume fraction

α_R Relaxation zone scalar fluid volume fraction

α_S, β_S Constants required for Pierson-Moskowitz and JONSWAP spectrum formulation

$\bar{x}$ Parameter in JONSWAP spectrum, equal to gx/u

β Frequency parameter in oscillating flow

χ_R Location within the relaxation zone

Δt Time increment   s

Δx Cell element length   m

Δz Cell element height   m

$\dot{u}$ Horizontal acceleration component m/s^2

$\dot{u}_\infty, \dot{v}_\infty, \dot{w}_\infty$ 3D irregular velocity components m/s^2

ϵ Bessel function parameter, $\epsilon = 1$ when $m = 0$ and 2 otherwise

η Location of free surface   m

η_D Diffracted surface elevation   m

η_∞	Irregular surface elevation	m
γ	Peak enhancement factor	
Γ_ξ	Rate of diffusion of field ξ	
Γ_T	Surface tension coefficient	
κ	Turbulent kinetic energy per unit mass	
κ_α	Surface curvature	
λ	Wavelength	m
$\mathbf{a}$	Arbitrary vector of interest	
$\mathbf{d}$	Vector connecting adjacent cell centres	
$\mathbf{g}$	Vertical acceleration due to gravity	m/s^2
$\mathbf{S}_T$	Strain rate tensor	
$\mathbf{u}$	Flow velocity vector	m/s
$\mathbf{U}_p$	Velocity vector at centroid point P	
$\mathbf{x}$	Location within cell	
$\mathbf{x}_p$	Location of cell centroid point	
μ	Dynamic viscosity	Pa.s
μ_T	Dynamic eddy viscosity	Pa.s
∇p	Pressure gradient	
∇	Nabla operator, $\nabla = \mathbf{i}\frac{\partial}{\partial x} + \mathbf{j}\frac{\partial}{\partial y} + \mathbf{k}\frac{\partial}{\partial z}$	

ν	Coefficient of kinematic viscosity	$\mathrm{m^2/s}$
ω	Angular wave acceleration	$\mathrm{rad/s}$
ω_n	n-th angular wave frequency component	$\mathrm{rad/Hz}$
ω_u	Parameter needed in Borgman force spectrum	
ϕ	Wave potential	$\mathrm{m^2/s}$
ϕ_D	Diffracted velocity potential	$\mathrm{m^2/s}$
ϕ_I	Incident velocity potential	$\mathrm{m^2/s}$
ϕ_R	Refracted velocity potential	$\mathrm{m^2/s}$
$\boldsymbol{\Delta}$	Orthogonal term in discretised diffusion term	
$\boldsymbol{\kappa}$	Non-orthogonal corrector term	
Ψ	Wave phase	
ψ_n	n-th randomly sampled phase value within the range $0 \leq \psi \leq 2\pi$	
ρ	Fluid density	$\mathrm{kg/m^2}$
σ	Spectral width parameter dependent on f_n	
σ_T	Surface tension	$\mathrm{kg/s^2}$
σ_η^2	Variance of free surface elevation	$\mathrm{m^2}$
τ	Reynolds stress tensor	
Θ	Wave direction, measured positive anti-clockwise from midpoint	
ξ^0	Old value of ζ	

ξ^n	New value of ξ	
ξ^t	Value of $\xi(t)$ at time t	
ξ_b	Boundary value of ζ	
ξ_N	Value of $\xi(x)$ at point N	
ξ_P	Value of $\xi(x)$ at point P	
ζ	Relaxaton zone value	
ζ_f	Face value of ζ	
a	Wave amplitude	m
a_{N}	Function of $\mathbf{u}$ at point N	
a_{P}	Function of $\mathbf{u}$ at point P	
a_n	$n - th$ amplitude component	m
C_d	Drag coefficient	
C_m	Inertia coefficient	
Co	Courant number	
D	Cylinder diameter	m
$D(f,\theta)$	Directional spectral function	
df	Frequency step size	Hz
F	Mass flux through the cell face	
f	Frequency	Hz

F_D	Diffracted force	N
f_d	Morison drag force	N
F_m	Force calculated with the Morison equation	N
f_m	Morison inertia force	N
f_n	n-th frequency component	Hz
f_p	Modal frequency	Hz
F_s	Sampling frequency	Hz
f_x	Ratio of distance $\overline{fN}$ and $\overline{PN}$	
f_z	Zero-crossing frequency	
$F_{p,D}$	Drag force due to in-line unsteady pressure gradient	N
$F_{p,L}$	Lift force due to transverse unsteady pressure gradient	N
$G(kR)$	Diffraction solution parameter	
H	Wave height	m
h	Mean water depth	m
$H_m^{(1)}$	Hankel function of 1st kind, of order m	
H_s	Significant wave height	m
$H_T(f)$	Transfer function	
$H_{s,D}$	Diffracted significant wave height	m
J_m	Bessel function of 1st kind, of order m	

k	Wave number	rad/m
k_n	n-th component wave number	rad/m
KC	Keulegan-Carpenter Number	
l	Submerged cylinder length	m
L_x	Computational domain length	
L_y	Computational domain width	
m	Bessel function order	
m_0	Zeroth moment	m
m_2	Second moment	m^2
N	Number of sampling points	
p	Total wave pressure	N/m
p^*	Pressure in excess of hydrostatic	Pa
Q	Any specific parameter value in the volume of fluid	
q_b	Gradient on the bounary	
R	Cylinder radius	m
Re	Reynolds number	
$S_u(f)$	u velocity spectrum	m^2/s^3
$S_w(f)$	w velocity spectrum	m^2/s^3
$S_{\dot{u}}(f)$	u acceleration spectrum	m^2/s^4

$S_{\dot{w}}(f)$ w acceleration spectrum m^2/s^4

$S_{\eta,D}$ Diffracted wave elevation spectrum   m² Hz

$S_\eta(f)$ Frequency spectrum of surface elevation m^2/Hz

$S_\xi\xi$ Source term

$S_{F,B}$ Borgman force spectrum N^2/Hz

$S_{F,D}$ Diffracted force spectrum   N² Hz

$S_{F,M}$ Morison force spectrum   N² Hz

S_{SM} Smoothed spectrum $unit/Hz$

T Wave period   s

t Time   s

t^* Normalised time

T_p Modal period   s

u Horizontal velocity component m/s

u_D Diffracted horizontal velocity component m/s

$u_\infty, v_\infty, w_\infty$ 3D irregular velocity components m/s

w Vertical velocity component m/s

w_D Diffracted vertical velocity component m/s

x, y Cartesian planar wave directions, in-line and transverse respectively   m

Y_m Bessel function of 2nd kind, of order m

z Location measured vertically upwards from mean water level   m

$[\xi]$ Column vector of dependent variables

$[A]$ Square matrix

$[R]$ Column vector of source terms

$\mathbf{H(U)}$ Matrix operator

$\mathbf{S}$ Outward pointing face area vector

$A.R.$ Cell aspect ratio

CV Control volume

A,B   Constants required in general spectral calculation

BBC   Bottom boundary condition

CFD   Computational fluid dynamics

CPU   Central processing unit

CTV   Crew transfer vessel

DFSBC Dynamic free surface boundary condition

DFT   Abbreviation for Discrete Fourier Transform

f   Cell face

FD   Finite difference

FE   Finite element

FFT   Abbreviation for Fast Fourier Transform

FIR   Finite impulse response

FV   Finite volume

FVM   Finite volume method

HPC   High-performance computer

ITTC   International Towing Tank Conference

KFSBC Kinematics free surface boundary condition

MA   Moving average

MAC   Marker-and-cell

MULES Multidimensional universal limiter for explicit solutions

N   Neighbour cell centroid point

NWT   Numerical wave tank

O & M Operations & Maintenance

P   Owner cell centroid point

PDE   Partial differential equation

PISO   Pressure implicit splitting operator

RANS   Reynolds averaged Navier-Stokes

SIMPLE Semi-implicit method for pressure linked equations

SOV   Service operations vessel

SWATH Small waterplane area twin hull

SWL   Still Water Level

VOF   Volume of fluid

WK   Wiener-Khinchin

Chapter 1

Introduction

1.1 Introduction

One of the greatest challenges facing society today is how to reduce the negative environmental impact due to CO_2 emissions entering the Earth's atmosphere. Global efforts to reduce CO_2 emissions necessitate a decline in energy production by large coal and gas power plants, accompanied by increasing development of clean energy production methods. By June 2015, 164 countries had adopted some form of renewable energy target to decrease carbon emissions (Kieffer and Couture, 2015).The European Union, for example, has set a target that 20% of energy must be obtained through renewable sources by 2020 (Sawin et al., 2015).

The marine environment provides a promising portfolio of renewable energy sources for coastal populations, which have an average population density three times that of the average global density (Small and Nicholls, 2003). The fastest growing is offshore wind power. Not only did offshore wind power exhibit a 17% increase in the year from 2013 to 2014, up to $\sim$433 GW worldwide, but also wind power was found to be a larger supplier of new power generation than any other technology (Kieffer and

Couture, 2015). As of January 2016, more than 3,000 offshore wind turbines (3.4 GW) were connected to the European grid (Pineda, 2016), bringing the global total to 12 GW. Of the available global capacity, 91% of offshore wind power presently commercially available is in Europe and the remaining 9% is located mostly in China, Japan, and South Korea (GWEC, 2016). China has set an ambitious goal to produce 30 GW of offshore wind energy by 2020 (Hong and Möller, 2012). However, due to increasing costs and insufficient marine spatial planning, Hong and Möller (2012) estimate that only 1 GW out of the target of 5 GW wind turbine capacity has been achieved to date.

Noting that estimates vary widely, offshore wind power nonetheless has huge potential: Krewitt et al. (2009) assessed the net exploitable potential to be about 16,000 TWh per year by 2050 and Capps and Zender (2010) calculated the overall global value of offshore wind energy to be approximately 340,000 Twh per year. Notwithstanding the technical potential for offshore wind power, current cost estimates put the investment cost per kilowatt hour for offshore wind to be approximately three times the investment per kilowatt hour for onshore wind (Taylor et al., 2016).

1.1.1   Operations & Maintenance Overview

Safe access to offshore wind turbine monopiles, which may be located 30-50 km from the shore (or onshore base) and in water up to 30 m deep (Corbetta et al., 2014, Sperstad et al., 2014), is essential to reducing the total energy cost of offshore wind power. Maintenance difficulties can occur even for near-shore wind farms; it was estimated recently that, for a wind farm off the coast of Ireland, the turbines were only accessible for repairs for 50-75% of the year (Breton and Moe, 2009, van Bussel et al.,

2001). Additional costs are incurred by hiring repair workers and vessels to transport the workers to the turbines. Operations and maintenance (O&M) costs can account for 25-50% of total energy production costs (Kostecki, 2014, Dalgic et al., 2015a, Maples et al., 2013). It has been estimated that costs could decrease by as much as 35% (Taylor et al., 2016) by 2025 with continued technological improvements and improved turbine access methods.

The rapid development and construction of offshore wind farms has outpaced research and there is a lack of consensus on the best methods for access and maintenance (van Bussel et al., 2001, Baagøe-Engels and Stentoft, 2016, Browell et al., 2016). In the context of global offshore wind farm capacity, Dalgic et al. (2015a) report that access for repairs is only possible on average for 200 days of the year, and reduces in areas with harsher climates. Access is by helicopter, service operations vessel (SOV), or crew transfer vessel (CTV) (Nielsen and Sorensen, 2011, Scheu et al., 2012). Helicopters have the advantage that they are not affected by wave conditions, but cannot be used to transport bulky equipment and are limited by the number of personnel that can travel aboard. Additionally, helicopters have a hire cost that is at least five times greater than a CTV (Auckland and Garlick, 2015). SOVs are useful for carrying heavy equipment and transporting a larger number of repair workers but again have the disadvantage over other access methods such as CTVs of increased cost.

The smaller CTVs, such as monohulls, catamarans or Small Waterplane Area Twin Hull (SWATH) type vessels, are more economical and account for 41% of the access methods used (Dalgic et al., 2015a). According to the National Renewable Energy Laboratory (NREL) report on

3

the development of offshore wind by Maples et al. (2013), the estimated availability of CTVs is between 61%-95%. The same report advises that the O&M strategy with the greatest potential to increase availability of the turbines and decrease costs is to improve the crew transfer system for the CTVs. By improving this system, total O&M costs can be decreased by an estimated $24.8M per year while increasing the average availability to 93% (Maples et al., 2013).

The only limiting sea state factor for CTV access is typically that $H_s \leq 1.5$ m, where H_s is the significant wave height (Dalgic et al., 2015a, Halvorsen-Weare et al., 2013). In general, the use of the significant wave height parameter as the main access criterion introduces additional uncertainty because H_s depends on *in situ* wind and wave conditions and also on the near-wake of the turbine monopile (Sperstad et al., 2014). Using H_s as the sole limiting factor provides no information on the modality of the sea state, which is subject to seasonal changes. These additional variables imply that the significant wave height alone may not provide sufficient information from which to determine the safety of the crew members and the stability of the CTV under operational conditions. Moreover, methods of determining H_s vary between wind farms and no regulation appears to exist whereby H_s can be determined. A survey conducted by Hoffman (2011) found a total of 49 different models were used by offshore wind energy companies for maintenance strategies.

1.1.2 Offshore Wind Turbine Access Method

Fixed monopile offshore wind turbines make up 80% of offshore wind turbine types (IEA, 2013). The remaining 20% are made up of foundation types such as a tripod or floating wind turbines. In order to access

the turbine for repairs, the CTV is driven towards the turbine monopile and, under steady thrust from the engine, contact between the turbine transition piece and the CTV is maintained by frictional forces. Representative monopiles have a single turbine transition piece, ideally located downstream, into which the vessel is driven upwind and illustrated in figure 1.1. The CTVs in use are approximately 8-25 metres long and are manoeuvred to allow for the vessel fender to be in direct contact with the boat landing (Dalgic et al., 2015a). Note that figure 1.1 implies that the incident waves $\vec{u}$, are unidirectional, whilst in practice there is a likelihood of multi-directional waves (see Section 2.3.1 and Chapter 7 for an in-depth discussion into wave directionality). The assumption of wave unidirectionality is made throughout this thesis.
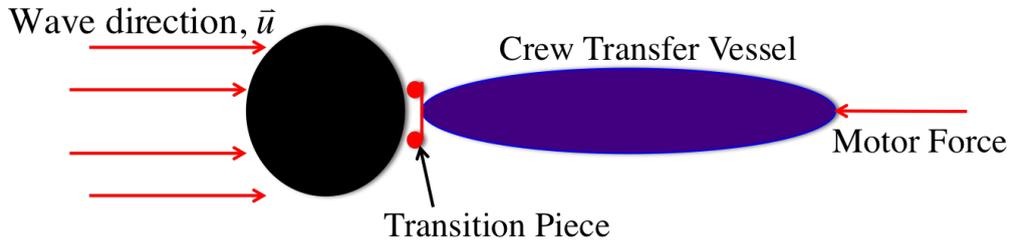
Figure 1.1: Illustration of crew transfer system with CTV abutted against monopile

This benchmark problem has attracted previous interest in the context of fatigue-induced damage to the support column under wave loading (see e.g. Chen et al. (2014), Agarwal and Manuel (2011), Finnegan and Goggins (2012)). Only very limited research has considered the influence of local hydrodynamics on CTV motion. No known experimental data exist concerning typical vessel motions during crew transfer; there are few research studies having considered the hydrodynamic forces on a floating body located within the wake of a fixed body, where frictional

forces instead of mooring lines are used to maintain contact.

Josse et al. (2011) presented a system in which hydrodynamic forces were ignored and the angle of the vessel against the turbine monopile was assumed to be the only parameter affecting the frictional contact. Although this approach was not validated, Josse et al. (2011) nevertheless found that wave frequency was a critical factor affecting motion and commented on the need for an improved hydrodynamic analysis of the effect of incident wave frequencies on vessel loading. König et al. (2017) also emphasised the necessity of calculating the hydrodynamic forces incident on the vessel and presented the results for two wave frequencies. This study found, as expected, that the influence of the monopile on the flow field decreases as the wave period increases. However, König et al. (2017) did not determine a limiting wave period for which the CTV could no longer operate. Moreover, this work focused primarily on the influence of the monopile in monochromatic wave fields in an experimental setting.

1.1.3   Turbine Access: Hydrodynamic limiting Conditions

Changes in the near-wake flow field where the CTV lies can result in a weakening of the frictional force and CTV "slippage", wherein the vessel becomes dislodged from the turbine monopile. When the CTV slips away from the monopile, crew members in transition are potentially endangered or there is a risk of incomplete maintenance leading to large economic losses. Eventually, it becomes necessary to predict the CTV motion under operating conditions, which requires detailed knowledge of the hydrodynamics and water particle kinematics within the vicinity of a turbine monopile. The hydrodynamic forces in the region, which are a

function of the incident wave period and monopile diameter, aid in identifying the limiting conditions under which the vessel remains in contact with the monopile turbine. The limiting condition occurs when the total vertical hydrodynamic forces on the vessel overcome the frictional contact force between the vessel fender and the transition piece on the monopile turbine (König et al., 2017). When the frictional contact is overcome, the vessel is prone to slipping away from the turbine monopile.

Figure 1.2 presents screen shots from a video filmed from the vessel during crew transfer. The time stamp shows that figure 1.2a and figure 1.2f are only 30 seconds apart, but during this period the vessel is seen to slip away from the turbine and the repair worker is unable to move onto the vessel. Sea conditions in the video appear to show small-amplitude waves with no evidence of nonlinearity or large breaking waves. This implies that vessel slippage is due to the unobservable local hydrodynamic force incident on the vessel. Thus, an improvement here would be the determination of the local hydrodynamic force in an irregular sea state representing the conditions at an operational offshore wind farm.

1.2   Research Methods

The focus herein is on constructing an accurate representation of a specific local sea state measured at an offshore wind farm and analysing the hydrodynamic response of the sea state interacting with a turbine monopile support column.

Predictions for the local hydrodynamic wave field are useful for engineers and vessel operators and common techniques for determining the wave field include both analytical and numerical methods. Analytical

7

Figure 1.2: Images taken from a video documenting crew transfer between vessel and monopile. Video provided by Alexis Billet, Managing Director of Resilience Energy Consulting.

methods can be fast to solve and require minimal computational effort, but often neglect important hydrodynamic features such as nonlinearity or viscous effects. Numerical methods using computational fluid dynamics (CFD) are capable of resolving nonlinearities for more accurate flow field representations, but at a high computational overhead. Hence, this project aims to formulate both numerical and analytical methods capable of approximating the local wave field at a turbine monopile.

1.2.1 Analytical Wave Formulation

Wave motion, using linear wave theory, is first described for time-dependent monochromatic waves. Assuming that the principle of superposition applies, waves in the open ocean are then represented as the sum of many periodic waves, each component with its own amplitude, frequency and phase. The wave amplitudes are acquired from a statistical analysis of the wave field in the frequency domain. Raw *in situ* data refers throughout to the time series of sea surface displacement, provided by EDF Energy Renewables from a single wave buoy located at Teesside Offshore Wind Farm. The *in situ* data is analysed and the local undisturbed sea state is formulated analytically.

Analytical methods are also applied to determine the total incident wave force on the monopile, in which the geometry is simplified by neglecting the transition piece. The monopile is modelled herein as a surface-piercing bottom-fixed circular cylinder in a regular, long-crested, small-amplitude wave field where the ratio of wave height to water depth is small and the waves are non-breaking. Hydrodynamic force loading is calculated typically depending on the wavelength-to-diameter ratio. Force calculation methods for both small- and large-diameter cylinders

are examined and the forces computed. For small-diameter cylinders, the Morison Equation (Morison et al., 1950) provides a good approximation for the wave loading in a viscous-dominant flow regime. The total linear diffraction force, derived by MacCamy and Fuchs (1954), provides a solution for large-diameter cylinders when diffraction effects occur and inertia forces are large. Wave force calculation methods are first presented for a monochromatic wave field, and then the formulation is extended to a unidirectional polychromatic wave field. In an irregular sea state, the wave force spectrum can be used to compare the forces in the frequency domain.

The wave field around the turbine monopile can also be determined analytically using the linear diffraction solution, again making the assumption that superposition applies in an irregular wave field. The time-dependent solution for the linear diffracted surface elevation values is converted to the frequency domain for analysis, from which the diffracted wave amplitudes are obtained. As with the undisturbed sea state, the diffracted wave particle velocity components are derived from the diffracted amplitude spectrum. Once formulated, this solution is fast to compute and provides values of the local sea state at an offshore wind farm; conversion to the frequency domain can also give information on the modality of the wave field. In addition to providing values for an undisturbed sea state, the analytical method also provides satisfactory approximations of the interaction of the local sea state with a turbine monopile, and the wave kinematics within this region that would influence vessel motion.

1.2.2 Numerical Methods

Numerical predictions are generated using the open-source CFD C++ library of solvers, OpenFOAM (version 2.4.0). OpenFOAM has been developed by the CFD community to simulate many types of fluid flow, including multi-phase. OpenFOAM is employed here to simulate numerically the interaction between a cylinder representing the monopile support column and the local wave field.

The numerical model is validated for an undisturbed linear wave field, where waves are simulated with four different wave period values and a single wave height in a numerical wave tank. Following Feuchtwang and Infield (2012) and Dalgic et al. (2015b), the representative operating wave conditions are equivalent to $H_s \leq 1.5$ m in the vicinity of a support column of diameter ~ 5 m. These values are chosen in order to model the type of conditions that prevail at a specific offshore wind site, Teesside Offshore Wind Farm off the east coast of the United Kingdom, where the key wave periods are in the range $4 \text{ s} \leq T \leq 10 \text{ s}$ and the mean water depth $h \approx 15$ m.

The analytically calculated wave force incident on the cylinder for a regular wave field, where well-documented solutions for the force loading exist, allows the numerical model to be verified in a regular wave field. Altering the wave period also means that the wavelength-to-diameter ratio changes and the effect on the flow due to the presence of the monopile becomes more apparent with decreasing wavelength. Diffraction and viscous solutions for the force calculation are employed and compared to numerical solutions, through application of no-slip and slip cylinder wall boundary conditions that coincide with viscous- or inertia-dominant

regimes.

Finally, following verification of the numerical model against the analytical solutions for regular waves, the model is extended to incorporate an irregular wave field using statistical analysis of *in situ* data tracking the ocean surface. To accomplish this, the *in situ* displacement data must be converted to the frequency domain, from which important statistical parameters, such as the significant wave height and modal wave period, can be determined from the spectrum. Additionally, although the assumption is made throughout that the wave field is unidirectional, a statistical representation of the displacement data can provide information on the modality of the wave spectra.

To simulate the irregular wave field numerically, a boundary condition is developed for the purpose of this research for use with OpenFOAM. The boundary condition is capable of generating a specific sea state, dependent on the spectral values (see Section 2.3). Simulating the exact sea state at an offshore wind farm provides a method with which the interaction of a specific sea state with a turbine monopile may be determined numerically. OpenFOAM is a fully nonlinear model and can resolve higher-order effects neglected by the linear methods.

The work undertaken for this thesis has produced two methods for determining the detailed linear wave kinematics found locally at an offshore wind farm, based on data obtained from the location. With knowledge of the wake kinematics within this region and the measured sea state found at an offshore wind farm, practitioners can decide whether to attempt turbine access with much greater detail of the hydrodynamics, in addition to knowledge of the significant wave height.

1.3　Purpose of Research

The purpose of this thesis is to provide operators of companies employing offshore wind turbine repair workers, and engineers tasked with improving the O&M process, a method of resolving the sea state at specific offshore wind farms. Current repair vessel access limits rely solely on the significant wave height, an observable parameter which provides no information on the directionality of a sea state. Access methods, in which the vessel operator manoeuvres the vessel into the turbine and continuously runs the vessel motor, thereby driving the vessel into the turbine and relying on frictional contact, cannot account for hydrodynamics within the wave field or non-negligible wave diffraction.

By computing both numerical and analytical solutions to the wave-monopile interaction, it can be shown that the analytical linear diffraction solution for irregular waves provides a good approximation to the wave field in the vicinity of a turbine monopile, when compared to the fully nonlinear numerical solution. Analytical solutions are beneficial to engineers or consultants who do not have access to large supercomputers or significant computational resources.

The results provided by the current analytical method can give practitioners a good initial approximation of the wave field that a CTV will enter. When available, improved results for the wave field can be provided through numerical methods capable of resolving nonlinearities. The open-source numerical method used here is freely available, making it an affordable option for engineers or consultants without access to powerful computers with multi-core processors. By developing the boundary condition for generating any unidirectional wave field from a given spectral

data set, many additional numerical simulations of the interaction of an actual sea state with offshore structures can be examined.

Both analytical and numerical calculation methods are employed to present two sets of solutions for the local hydrodynamic wave field. Each solution method has advantages and disadvantages. The analytical solution has the advantage that it can produce approximate results of the wave kinematics around a monopile quickly, but is restricted to linear solutions of an inviscid flow. The numerical solution has the advantage that it can resolve nonlinearities and other complicating flow factors, with the obvious drawback of a large computational overhead. Nevertheless, both methods utilise field information obtained as wave buoy data and lead to sensible approximations of the local wave field.

1.4   Aim and Objective

The aim of this thesis is to provide offshore wind farm practitioners with a method for determining the sea state at an offshore wind farm, the wave loading on a turbine monopile and the accompanying local hydrodynamics. This thesis describes the following steps:

1. A statistical analysis of the spectral distribution of the surface elevation from data obtained from an *in situ* wave buoy measuring surface displacement at Teesside Offshore Wind Farm in the southern North Sea.

2. Utilisation of the verified spectral distribution values as input, to formulate the undisturbed surface elevation and wave particle kinematics analytically.

3. Reproduction of the sea state numerically through application of a boundary condition developed for this project. This boundary condition, developed for use with OpenFOAM, allows for the calculation of in-line and horizontal velocity values on the boundary of the computational domain from spectral values.

4. Formulation of analytical solutions for the spectrum of wave forces on the turbine monopile in the irregular sea state represented by the wave buoy data. The solution methods reflect the influence that the presence of the monopile has on the passing wave field. For shorter wave periods, wave diffraction is expected to occur, thereby affecting the local hydrodynamics.

5. Employ application of linear wave diffraction solutions in an irregular sea to calculate the diffracted surface elevation and its spectrum. Obtain the diffracted significant wave height and local diffracted hydrodynamics relevant to vessel motion, such as velocities, accelerations, and forces, analytically in the vicinity of the turbine monopile.

6. Examine numerically the interaction between the simulated sea state and the turbine monopile; compare and contrast wave forces and diffracted hydrodynamics to solutions obtained analytically.

1.5 Thesis Outline

Chapter 2 describes the analytical formulation of a linear wave field, in which wave motion in a regular wave field is first discussed, followed by the statistical formulation used for the sea state in the open ocean.

Chapter 3 examines wave loading on a cylinder in unidirectional and in oscillating flow, together with the spectral representation of forces on a cylinder in irregular waves. Chapter 4 considers the numerical model, meshing and discretisation methods, and solution algorithms used in OpenFOAM. Chapter 5 describes the preliminary tests, including the interaction between a steady current and a surface-piercing cylinder; linear progressive wave loading on a cylinder is also considered. This chapter also discusses simulation of an undisturbed regular wave field and the interaction between the regular wave field and surface-piercing cylinder. Details are given of an investigation into the effect that the wave absorption zone has on the computational domain length, and whether the absorption zone length can be reduced through an adjustment of relaxation zone parameters. Chapter 6 describes an extension of the regular wave model to represent an irregular wave field based on wave buoy data from Teesside Offshore Wind Farm during each of the four seasons throughout 2015/2016. From this *in situ* data, the analytical and numerical methods outlined in the previous chapters are applied to generate the sea state at Teesside offshore wind farm and calculate the interaction between the local sea state and a wind turbine monopile. Chapter 7 summarises the overall conclusions, challenges and suggestions for future work.

Chapter 2

Mathematical Theory

Chapter Summary

The mathematical theory presented in this chapter focuses on determining the water particle kinematics in an undisturbed wave field. Wave motions are described for regular linear waves and for an irregular wave field. Statistical methods are outlined for determining the water particle amplitudes, velocities and accelerations in an irregular wave field. A brief discussion of wave directionality is also provided.

2.1 Introduction

An analytical approximation to the wave particle kinematics around an offshore wind turbine support column can provide important information about the waves incident on a CTV under operating conditions. The undisturbed wave field far from the monopile is modelled using linear wave theory for small-amplitude long-crested waves; a brief discussion of linear wave theory is given in Section 2.2. In the ocean, where waves of many different frequencies and amplitudes contribute to the wave field,

the undisturbed sea state is often described by the superposition of linear sinusoidal waves (Faltinsen, 1990). It is usually assumed in linear theory that the waves are long-crested and of small-amplitude, with the fluid incompressible and inviscid and the flow is irrotational.

As a consequence of the irregular properties of the ocean sea state, a statistical spectral representation of the wave elevation in the frequency domain can also be used to approximate the entire wave field and provide summary statistics. The undisturbed wave amplitudes and water particle kinematics incident on the turbine monopile are computed from the wave elevation spectrum (Sarpkaya, 1986). For engineering applications, it is usual that wave displacement data is obtained from *in situ* wave buoys, which in this case are located at the relevant wind farm. Statistical representations of the wave buoy displacement data can be used to model the sea state and verify that the correct sea state has been produced. Further details describing sea state representation are given in Section 2.3. Treatment of waves in a multidirectional sea state is briefly considered in Section 2.3.1, although this thesis will restrict the later analysis to unidirectional waves.

2.2   Linear Wave Theory

Typically, CTV access to a turbine monopile is limited by the significant wave height H_s, which for most vessels currently in use must be below 1.5 m for operation (Dalgic et al., 2015a, Halvorsen-Weare et al., 2013). At the site of interest herein, Teesside Offshore Wind Farm, the average water depth is 15 m. For the small-amplitude waves required for CTV access, it can be assumed that for all relevant wave fields, the operating

wave height-to-depth ratio is ≤ 0.1.

Assuming that the fluid is incompressible and inviscid, with the motion irrotational, a velocity potential ϕ may be employed, which satisfies Laplace's equation

$$\nabla^2\phi = 0, \qquad (2.1)$$

in which

$$\nabla = \mathbf{i}\frac{\partial}{\partial x} + \mathbf{j}\frac{\partial}{\partial y} + \mathbf{k}\frac{\partial}{\partial z}, \qquad (2.2)$$

where x and y are Cartesian distance components in the horizontal plane and z the vertical distance measured vertically upward from the still water level. Figure 2.1 illustrates the wave direction and other parameters defining the wave field and cylinder properties.
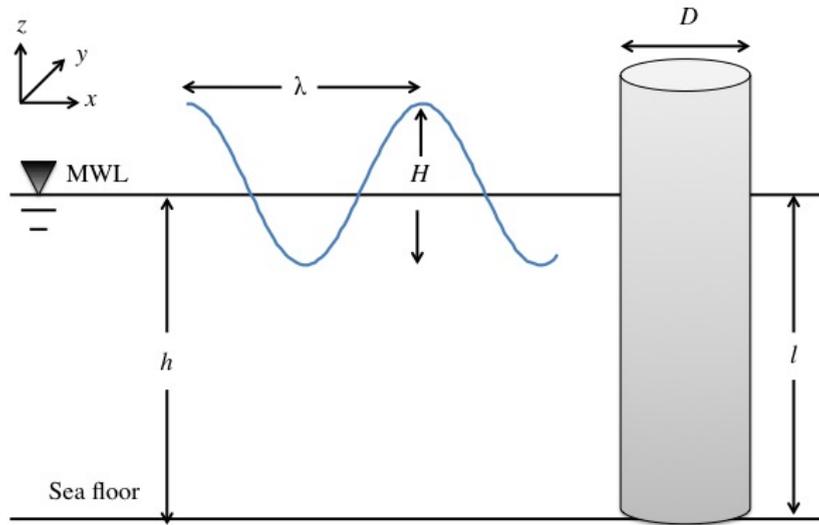
Figure 2.1: Diagram indicating the wave parameters for a linear wave moving past a cylinder

It is assumed that the waves are regular and long-crested with am-

plitude a. Boundary conditions on the bottom and at the free surface must be applied to determine the velocity potential ϕ that satisfies (2.1). On the bottom, located at $z = -h$, where h is the water depth, no flow should pass through the boundary and the bottom boundary condition (BBC) is

$$\left.\frac{\partial \phi}{\partial z}\right|_{z=-h} = 0. \tag{2.3}$$

Bernoulli's equation for unsteady flow is then used to determine the pressure condition on the free-surface. The unsteady Bernoulli equation provides the dynamic free-surface boundary condition (DFSBC), given by

$$\frac{1}{2}(u^2 + v^2 + w^2) + \frac{p}{\rho} + gz + \frac{\partial \phi}{\partial t} = 0, \tag{2.4}$$

where u, v and w are the velocity components, g is acceleration due to gravity, p is the dynamic pressure, ρ is the fluid density and t is time. Assuming that u^2, v^2 and w^2 are small, the linearised form of the DFSBC is given by

$$\left.\frac{\partial \phi}{\partial t} + g\eta\right|_{z=\eta} = 0, \tag{2.5}$$

where η is the free-surface elevation above the still water level. From the boundary conditions above, the solution of (2.1) is given by (see e.g. Dean and Dalrymple (1991))

$$\phi = -\frac{a\omega}{k}\frac{\cosh k\,(h+z)}{\cosh kh}\sin\Psi \tag{2.6}$$

where $\mathbf{k} = (k_1, k_2, 0)$ is the wavenumber vector, $k = |\mathbf{k}|$ is the wavenumber, ω is the angular wave frequency and $\Psi\,(\mathbf{x}, t)$ is the phase function,

given as a function of position vector $\mathbf{x}$ and time t as

$$\Psi(x,t) = (\mathbf{k}.\mathbf{x} - \omega t), \qquad (2.7)$$

where ω is the frequency in radians/sec. The linearised kinematic free surface boundary condition (KFSBC) ensures that the vertical velocity component is equal to the rate of displacement of the free surface, such that

$$\left.\frac{\partial \phi}{\partial z}\right|_{z=0} = \frac{\partial \eta}{\partial t}. \qquad (2.8)$$

The value for η when no cylinder is present can be given as a sinusoidal motion of constant amplitude $a = H/2$, where H is the wave height, given by

$$\eta = a\cos(\mathbf{k}.\mathbf{x} - \omega t). \qquad (2.9)$$

From (2.8) and (2.9), k (where the subscript 1 has been dropped for simplicity) is related to ω by the linear dispersion relation,

$$\omega^2 = gk\tanh kh, \qquad (2.10)$$

in which g is acceleration due to gravity. The linear dispersion relation describes the change in wave properties with respect to physical parameters; the wavelengths become shorter and the speed is decreased with increasing depth and constant wave period (Sarpkaya and Isaacson, 1981). The wave period T and wave length λ are related to ω and k, respectively, by

$$\omega = \frac{2\pi}{T} \tag{2.11}$$

and

$$k = \frac{2\pi}{\lambda}. \tag{2.12}$$

The system is considered to be linear if it satisfies properties of scaling and superposition. Equation (2.10) is usually solved iteratively using a standard technique, such as the Newton-Raphson method or bi-section.

The water particle velocity components in the horizontal x and y directions and vertical z are obtained directly from the velocity potential as

$$u = \frac{\partial \phi}{\partial x}, \quad v = \frac{\partial \phi}{\partial y}, \quad w = \frac{\partial \phi}{\partial z}. \tag{2.13}$$

Similarly, the water particle accelerations are defined as

$$\dot{u} = \frac{\mathrm{D}u}{\mathrm{D}t}, \quad \dot{v} = \frac{\mathrm{D}u}{\mathrm{D}t}, \quad \dot{w} = \frac{\mathrm{D}u}{\mathrm{D}t}. \tag{2.14}$$

From (2.6) and (2.13) and by applying the linear dispersion relation (2.10), the undisturbed in-line and vertical velocity components in a regular wave field can be written

$$u = \frac{H}{2} \frac{gk}{\omega} \frac{\cosh k \, (h + z)}{\cosh(kh)} \cos \Psi \cos \Theta \tag{2.15}$$

$$v = \frac{H}{2} \frac{gk}{\omega} \frac{\cosh k \, (h + z)}{\cosh(kh)} \cos \Psi \sin \Theta \tag{2.16}$$

$$w = \frac{H}{2} \frac{gk}{\omega} \frac{\sinh k \, (h + z)}{\cosh kh} \sin \Psi \tag{2.17}$$

and similarly the accelerations can be written as

$$\dot{u} = \frac{\mathrm{D}u}{\mathrm{D}t} = -\frac{H}{2}gk\frac{\cosh k\,(h+z)}{\sinh kh}\sin\Psi\cos\Theta \qquad (2.18)$$

$$\dot{v} = \frac{\mathrm{D}v}{\mathrm{D}t} = -\frac{H}{2}gk\frac{\cosh k\,(h+z)}{\sinh kh}\cos\Psi\sin\Theta \qquad (2.19)$$

$$\dot{w} = \frac{\mathrm{D}w}{\mathrm{D}t} = \frac{H}{2}gk\frac{\sinh k\,(h+z)}{\sinh kh}\cos\Psi. \qquad (2.20)$$

By applying the linearised form of the Bernoulli equation from (2.5), the pressure underneath a progressive wave, written in terms of the potential, is

$$p = -\rho\frac{\partial\phi}{\partial t} - \rho g z. \qquad (2.21)$$

In (2.21), the first term on the right-hand-side describes the dynamic pressure component due to the motion of the fluid and the second term is the hydrostatic component from gravity, acting in the $-z$ direction. The static pressure is a function of depth only and does not contribute to the time-dependent loading. Only waves in a regular wave field with a single wave frequency have been considered thus far. Extension to an irregular wave field with multiple wave frequencies will be discussed in Section 2.3. Henceforth, the wave formulation will be given for a 2-D wave field, where the angle of approach $\Theta = 0$.

2.3 Ocean Statistics

For small-amplitude waves, the unidirectional sea state can be represented as the linear superposition of waves with a range of frequencies and amplitudes where the random phasing ψ is between 0 and 2π and

represents the random distribution of wave phases inherent in an irregular sea. In the ocean, it is common to define the stationary sea state in the frequency domain by its spectral function $S(f)$ (Dean and Dalrymple, 1991), where f is frequency in Hz and $f = \omega/2\pi$.

To compute the wave spectrum, a Fourier analysis of the wave field is conducted. Fourier analysis permits any continuous or piecewise-continuous function to be represented in the time domain as the sum of periodic functions with varying frequencies and Fourier coefficients, corresponding to the individual wave amplitudes (Sarpkaya and Isaacson, 1981). For the greatest accuracy, the wave field is ideally extracted from multiple wave buoys contemporaneously measuring surface displacement over a prolonged length of time (McAllister et al., 2017). Whilst a Fourier transform can be computationally demanding and time-consuming to calculate, a Fast Fourier Transform (FFT) is an algorithm that can very quickly compute a Discrete Fourier Transform (DFT), which converts a finite sequence of samples of a function into same-length equidistant discrete samples. The spectral function is then related to the FFT by

$$S(f) = \frac{1}{F_s N}|\text{FFT}|^2, \tag{2.22}$$

where F_s is the sampling frequency and N is the total number of frequency bins.

It can be difficult to obtain displacement data from a specific location and it is common to apply established wave spectra when the relevant data are not available. Wave spectra are depth- and location-dependent and a number of models have been developed to describe the characteristics of a wave spectrum for key parameters including wave period,

wind direction and fetch; the fetch determines whether the sea state is fully developed or not. Spectral equations for wave spectra measured at a specified point are typically of the form

$$S(f) = \frac{A}{f^5} e^{\left(-\frac{B}{f^4}\right)}, \tag{2.23}$$

where A and B are constants that represent parameters needed for calculating the spectral values.

The key parameters and representative wave spectrum are location-dependent. Common wave parameters are the significant wave height H_s, which is an observational measurement of the average of the highest one-third of all waves, and the mean wave period T_p (Chakrabarti, 1987). For fully-developed unidirectional seas, the Pierson-Moskowitz Spectrum is often applied. The single-sided Pierson-Moskowitz spectrum is formulated from either one (spectral wave height or windspeed or peak period) or two (significant wave height and peak parameter) known parameters (Pierson and Moskowitz, 1964). The Pierson-Moskowitz Spectrum, defined from zero to infinity, is given by

$$S(f) = \frac{1}{(2\pi)^4} \alpha_s g^2 f^{-5} e^{\left(-\beta_s \left(\frac{f_p}{f}\right)^4\right)}, \tag{2.24}$$

where $\alpha_s = 0.0081$ and $\beta_s = 0.74$ are empirically determined numerical constants controlling the intensity and shape of the spectra, respectively, and peak frequency $f_p = \frac{1}{2\pi} 0.4 \sqrt{g/H_s}$ (Pierson and Moskowitz, 1964). The Pierson-Moskowitz Spectrum was originally the recommended spectral formation by the International Towing Tank Conference (ITTC), but due to its dependence on fully developed seas, two-parameter spectra such as the JONSWAP spectrum was developed for the North Sea, where the

fetch length is limited by land (Hasselmann et al., 1973). The JONSWAP spectrum is a fetch-limited variation of the Pierson-Moskowitz spectrum defined by

$$S(f) = \frac{1}{(2\pi)^4} \alpha_s g^2 f^{-5} e^{\left[-\frac{5}{4} \left(\frac{f}{f_p} \right)^{-4} \gamma^\delta \right]}, \qquad (2.25)$$

where γ is the peak enhancement factor with a given value of 3.3 and

$$\delta = \exp \left[-\frac{(f - f_p)^2}{2\sigma^2 f_p^2} \right], \qquad (2.26)$$

$$\alpha_s = 0.076 \bar{x}^{-0.22}, \qquad (2.27)$$

$$\bar{x} = \frac{gx}{U^2}, \quad \text{and} \qquad (2.28)$$

$$\sigma = \begin{cases} 0.7 & \text{for } f \leq f_p \\ 0.9 & \text{for } f > f_p. \end{cases} \qquad (2.29)$$

The value $\bar{x}$ indicates fetch where U is the wind speed taken at 19.5 m above sea level. The JONSWAP spectrum is valid for seas that are narrow-banded (such as the North Sea) and is often used in the offshore industry. Other spectral types, such as the modified Pierson-Moskowitz spectrum (Bretschneider spectrum) (Bretschneider, 1959), have been developed for seas with different parameters, locations, currents, fetch, etc.

For any wave spectrum, the area under the spectral curve is the zeroth moment, m_0, about the axis (Pierson and Moskowitz, 1964), and gives the total energy within the spectral function. The value for m_0 is equivalent to the variance of the wave elevation time series σ_η^2 (Chakrabarti, 1987), or

$$\sigma_\eta^2 = m_0 = \int_0^\infty S(f)_\eta df. \tag{2.30}$$

From the frequency spectrum, the significant wave height H_s and amplitude components a_n can be found from (Papoulis, 1991, Sumer and Fredsøe, 2006) to be

$$H_s = 4\sqrt{m_0} \tag{2.31}$$

and

$$a_n = \sqrt{2S(f)_\eta \Delta f}. \tag{2.32}$$

Under the assumption that superposition applies, the undisturbed free surface elevation of a two-dimensional random sea state in the (x, z)-plane is described by linear wave theory and the wave spectrum (2.22) (Dean and Dalrymple, 1991). For an irregular wave (2.9) becomes

$$\eta_\infty = \sum_{n=1}^N a_n cos(k_n x - \omega_n t + \psi_n), \tag{2.33}$$

where the amplitude of the n-th component a_n is obtained from (2.32) and ψ is randomly sampled from the phase distribution. Equation (2.33) is the 2-D representation when y components are small, which is assumed henceforth. The linear dispersion relation for this frequency component is given by $w_n^2 = gk_n \tanh k_n h$. Similarly by superposition, the undisturbed vertical and horizontal velocity components in irregular waves may be expressed

$$u_\infty = \sum_{n=1}^{N} a_n \omega_n \frac{\cosh k_n \left(z + h \right)}{\cosh k_n h} \cos \left(k_n x - \omega_n t + \psi_n \right) \cos \Theta \qquad (2.34)$$

$$w_\infty = \sum_{n=1}^{N} a_n \omega_n \frac{\sinh k_n \left(z + h \right)}{\cosh k_n h} \sin \left(k_n x - \omega_n t + \psi_n \right), \qquad (2.35)$$

and the irregular water particle acceleration components are

$$\dot{u}_\infty = \frac{\mathrm{D} u_\infty}{\mathrm{D} t} = \sum_{n=1}^{N} a_n g k_n \frac{\cosh k_n \left(h + z \right)}{\sinh k_n h} \sin(k_n x - \omega_n t + \psi_n) \cos \Theta$$

$$(2.36)$$

$$\dot{w}_\infty = \frac{\mathrm{D} w_\infty}{\mathrm{D} t} = \sum_{n=1}^{N} a_n g k_n \frac{\sinh k_n \left(h + z \right)}{\sinh k_n h} \cos(k_n x - \omega_n t + \psi_n). \qquad (2.37)$$

The analytically calculated undisturbed surface elevation in (2.33) can be statistically correlated to the *in situ* displacement data by evaluating the wave spectrum $S(f)_\eta$ of both data sets and comparing the m_0 values and spectral shapes. Equation (2.30) can be used to verify that each wave spectrum correctly corresponds to its respective surface elevation data.

The average frequency that the signal crosses the x-axis in the upward direction, or the zero-crossing frequency, can also be obtained from the wave spectrum,

$$f_z = \sqrt{\frac{m_2}{m_0}}, \qquad (2.38)$$

where m_2 is the second moment, given by

$$m_2 = \int_0^\infty f^2 S(f)_\eta df. \qquad (2.39)$$

The area under the curve for a continuous wave spectrum can be approximated using a discrete numerical integration method, such as Simpson's rule, which uses quadratic interpolation so that the expected error is bound by (Δf^4), where Δf is the frequency step size. Therefore, if Δf is reasonably small, Simpson's rule has an appreciable advantage in accuracy over linear interpolation methods and gives a good approximation of the total area.

By applying the method of superposition, a specific unidirectional sea state and wave spectrum can be constructed when displacement data are available. When location-specific data is not available, an idealised spectrum most suitable to the region of interest, such as Pierson-Moskowitz or JONSWAP, can be applied. Simulation of the correct sea state is essential to the design of structures in offshore environments. It has previously been established that regular waves often over-predict the forces and surface elevations around an offshore structure in comparison to irregular waves (Goda, 1985).

Spectral Smoothing

When determining the wave spectrum using Fourier analysis, the record length for the spectrum is finite, implying that the values in the spectrum are only apparent values rather than the true refined spectral density values from an infinite time sample. Spectra are therefore smoothed in order to remove noise when recording the steady state spectral function. Herein, a Moving Average filter (MA filter) is chosen to filter the data points and smooth the spectrum. An MA filter is a Low-Pass Finite Impulse Response (FIR) filter. The MA filter works by taking M input points from either side of a point in the spectral signal and calculating the

average over the M points, resulting in a single data point. The larger the value of M, the more the signal is filtered and smoothed (Chakrabarti, 1987). The algorithm for the smoothed spectrum $\bar{S}_{sm}$ using a MA filter is

$$
\begin{aligned}
\bar{S}(f)_{sm} &= \frac{S_M + S_{M-1} + ... + S_{M-(N-1)}}{N} \\
&= \frac{1}{N} \sum_{i=0}^{N-1} S_{M-i}
\end{aligned}
\tag{2.40}
$$

where M are the chosen number of data points and correspond to one side of the unfiltered point, N in this case is the total number of points to average over, and i is the current point. In the present work, a minimum of 8 input points (N) were required to obtain a smoothed, filtered spectrum.

2.3.1 Directional Seas

In an ocean environment, waves travel from different directions and with multiple modal frequencies. Without including directionality in the wave spectrum, the wave particle velocities and free-surface profiles may be overestimated (Hughes and Thompson, 1986). However, to take the wave direction into account in the statistical analysis, wave displacement data taken during identical time intervals at multiple points are required. In this work, as is commonly the case in offshore analysis, data from only one point was available. It is difficult to resolve the prevailing wind-wave-swell directions from single-point observations (McAllister et al., 2017, Adcock and Taylor, 2009) and so directionality will not be included in the later application to the site at Teesside. Nevertheless, a method to

incorporate the directionality of the waves that can be used when data from multiple points are available is briefly discussed below.

The angular distribution of the wave energy in directional seas is described by a directional spreading function, which is based on the specified sea state and directionality information provided by displacement data from multiple wave buoys (Venugopal et al., 2005). Estimating the directionality of the wave components within a sea state typically requires a minimum of three simultaneous time series measurements (McAllister et al., 2017). Previously, the spectrum was defined as a function of frequency only $S(f)_\eta$, but to account for wave directionality, the wave spectrum is redefined as $S(f_n, \theta_m)_\eta$, where θ is the wave direction. The subscript n again denotes the n-th frequency component and m relates to a given wave direction contained within the wave elevation time series. The wave spectrum is equivalent to the directional spectrum, such that

$$S(f)_\eta = \int_{-\pi}^{\pi} S(f, \theta)_\eta \, \mathrm{d}\theta. \tag{2.41}$$

From (2.41), the variance of a multi-directional free surface is defined as

$$\sigma_\eta^2 = \int_0^\infty \int_{-\pi}^{\pi} S(f, \theta)_\eta \mathrm{d}\theta \mathrm{d}f. \tag{2.42}$$

As in (2.32), the amplitude components are defined as

$$a_{nm} = \sqrt{2S(f_n, \theta_m)_\eta \, \mathrm{d}f \mathrm{d}\theta}. \tag{2.43}$$

The directional surface elevation is determined from (2.33) with amplitudes (2.43).

In practice, measurement of $S(f, \theta)_\eta$ is difficult, so parametric representations of the directional spectrum are used, whereby

$$S\left(f,\theta\right)_{\eta} = D\left(f,\theta\right)S(f)_{\eta}, \qquad\qquad (2.44)$$

and $D\left(f,\theta\right)$ is a spreading function. Several common spreading functions exist including the "cosine-squared" type, an example of which is

$$D(f,\theta) = D(\theta) = \begin{cases} \frac{2}{\pi}\cos^2\theta & \text{for} \quad \left(-\frac{\pi}{2}+\theta\right) < \theta < \left(\frac{\pi}{2}+\theta\right) \\ 0 & \text{otherwise.} \end{cases} \qquad (2.45)$$

It is hoped that future developments of this work will use a method such as that presented by Adcock and Taylor (2009); this would enable weak nonlinearities within the wave field to contain additional spreading functions to reproduce multidirectional sea states, including crossing seas, more accurately. Without the inclusion of directionality, there is a risk of overestimating the total in-line force in a design wave environment (such as that outlined in Section 2.3), relative to the wave loading from the real sea (Sarpkaya, 1986). Future improvements to the methods discussed in this chapter would take into consideration the wave approach angle but, as previously discussed, this process can be difficult without data from multiple points and is beyond the scope of the present analysis.

2.4   Summary

In this chapter, the mathematical formulation has been presented for equations describing linear waves. Commencing with a brief background of linear wave theory, an overview of irregular wave fields and ocean statistical analysis has been given along with descriptions of the wave

parameters and statistical values that can be inferred from the stationary ocean process. A statistical analysis of ocean waves provides valuable information concerning the water particle kinematics, energy and wave amplitudes present in an irregular wave field. Wave parameters determined here will be compared to the numerical results in Chapters 4 and 5 to investigate the validity of the numerical model.

Chapter 3

Wave Loading on a Vertical Cylinder

Chapter Summary

This chapter focuses on determining the water particle kinematics in the near-vicinity of a fixed monopile turbine support structure in waves. The rationale is that predictions of the water particle kinematics from an analytical approximation of the wave field in the very-near wake of a monopile turbine can be used for a 2-D vessel motion analysis based on local input wave conditions. Methods for computing the in-line wave forces are presented for small- and large-diameter cylinders located in regular and irregular wave fields. An analytical method is outlined for determining the water particle kinematics around a monopile turbine within the region where a crew transfer vessel (CTV) would lie, for any incident unidirectional sea state.

3.1 Introduction

Subsequent to the time-dependent and statistical representation of the undisturbed wave field and the determination of the water particle kinematics in Chapter 2, it is desirable to determine the effect that the monopile has on the passing wave field. The appropriate method for describing the fluid-structure interaction is dependent on the monopile diameter-to-wavelength ratio. For a small-diameter monopile, it is assumed that the presence of the monopile has a negligible effect on the passing flow, although a viscous wake will form, and the Morison Equation (Morison et al., 1950) provides a suitable approximation for the in-line wave force. For large-diameter monopiles where the effect of the monopile on the incident wave field must be taken into account, the linear diffraction theory presented by MacCamy and Fuchs (1954) provides a satisfactory approximation to the diffracted surface elevation and the diffracted wave force. The in-line wave force loading will be discussed first for waves in a monochromatic wave field, and then for waves in an irregular undirectional wave field. Both force-loading calculation methods will be described in Section 3.2.

An expression for the diffracted wave spectrum from an arbitrary input sea state is presented in Section 3.3, with the derivation of an autocorrelation function using the Wiener-Khinchin theoreom. The transfer function derived is not presently validated by data and therefore the formulation herein is solely theoretical. However, the formulation could be of interest for determining the water particle kinematics within the region of the turbine monopile from any given wave buoy displacement data. Further work is recommended to validate experimentally the trans-

fer function.

An important outcome of this chapter is the development of an analytical method to determine the linear diffracted wave particle kinematics and wave force loading for any unidirectional irregular sea state under operating conditions. Analytical solutions for the water particle kinematics and wave forces within this region would provide CTV operators with fast approximations of the expected wave loading on the vessel. Improved knowledge of the water particle kinematics within this region could also greatly enhance the vessel operators' ability to manoeuvre the vessel to avoid unwanted wave motion and remain steady to allow safe crew transfer.

3.2 Overview of Wave Forces on a Vertical Cylinder

The turbine monopile support column is idealised as a vertical smooth, surface-piercing, fixed circular cylinder. Close to the cylinder walls, viscous surface effects disturb the local flow and potential theory for describing undisturbed wave motion (see Section 2.2) no longer applies. The local hydrodynamic regime depends on the incident wave parameters, water depth and length scale of the cylinder. No method exists that is universally applicable for predicting the wave loading on a surface-piercing cylinder under all circumstances; the length scale of the cylinder, wave period, viscosity and other factors must be taken into account to determine the effect (if any) that the presence of the cylinder has on the passing water flow (Dean and Dalrymple, 1991). The total forces are dependent on the fluid flow regime, described in terms of the parame-

ters identified above, and relative size of the cylinder diameter D to the wavelength λ.

For small-diameter cylinders where the diameter-to-wavelength ratio $D/\lambda < 0.2$, it may be assumed that the presence of the cylinder has a negligible effect on the pressure field of the passing waves and viscous forces dominate. As the cylinder diameter-to-wavelength ratio increases, the presence of the cylinder modifies the local hydrodynamic pressure gradient and the inertia force, which is the force due to momentum, increases, related to wave diffraction. In the drag-inertia regime, where both drag and inertia forces are important, both viscous and diffraction force components contribute to wave loading, and the flow can experience additional effects due to wave nonlinearity in the presence of high-frequency diffracted waves (Swan and Sheikh, 2014).

The Reynolds number (Re) and the Keulegan-Carpenter number (KC) are commonly used to describe the ratio of inertia-to-viscous forces and the ratio of drag-to-inertia forces respectively, for a fluid flow past an obstacle (Faltinsen, 1990, Sarpkaya and Isaacson, 1981). Re and KC are given by

$$Re = \frac{U_\infty D}{\nu}, \tag{3.1}$$

$$KC = \frac{T U_\infty}{D}, \tag{3.2}$$

where T is the wave period, ν is the coefficient of fluid kinematic viscosity and U_∞ is the incident velocity magnitude.

Zdravkovich (1997) has classified unidirectional flow past a cylinder with respect to Re, and gave the flow descriptions listed in figure 3.1.

With increasing Re, the fluid flow changes from a laminar flow with no separation at the cylinder surface to a fully turbulent flow, where the flow motions are rotational and eddy shedding occurs. As the pressure gradient decreases, the vortices separate from the cylinder and travel downstream, creating a wake or a vortex pattern (Sumer and Fredsøe, 2006).

At Teesside Offshore Wind Farm, a typical monopile is of diameter $D \approx 5$ m, and the Reynolds number and Keulegan-Carpenter number ranges, based upon the cylinder diameter and under operational conditions, are within the ranges $1.2 \times 10^6 < Re < 3.6 \times 10^6$ and $0.35 < KC < 1.1$. In this case, KC remains small across the entire range of wave periods, implying that the inertia force is large. Whilst it might be expected that vortices form in this Reynolds number range (see figure 3.1), it is known that vortex shedding does not occur when $KC < 3$ (Sarpkaya and Isaacson, 1981). At high Re and low KC, a third parameter, $\beta = Re/KC$, is a better indicator than Re alone of the viscous forces present in the flow (Chaplin, 2000, Johanning et al., 2001, Sarpkaya, 2006) and is given by

$$\beta = \frac{D^2}{\nu T}. \tag{3.3}$$

The total in-line wave force on a vertical surface-piercing fixed cylinder in long-crested waves can be attributed to the unsteady pressure field within the incident wave field (see (2.21)) over the submerged cylinder length (Dean and Dalrymple, 1991). In an ideal potential flow where it is assumed that the cylinder has no effect on the flow field, the total in-line force per unit height can be calculated as the sum of the drag force ($F_{p,D}$)

a)	No separation. Creeping flow	Re < 5
b)	A fixed pair of symmetric vortices	5 < Re < 40
c)	Laminar vortex street	40 < Re < 200
d)	Transition to turbulence in the wake	200 < Re < 300
e)	Wake completely turbulent. A:Laminar boundary layer separation	$300 < Re < 3 \times 10^5$ Subcritical
f)	A:Laminar boundary layer separation B:Turbulent boundary layer separation;but boundary layer laminar	$3 \times 10^5 < Re < 3.5 \times 10^5$ Critical (Lower transition)
g)	B: Turbulent boundary layer separation;the boundary layer partly laminar partly turbulent	$3.5 \times 10^5 < Re < 1.5 \times 10^6$ Supercritical
h)	C: Boundary layer completely turbulent at one side	$1.5 \times 10^6 < Re < 4 \times 10^6$ Upper transition
i)	C: Boundary layer completely turbulent at two sides	$4 \times 10^6 < Re$ Transcritical
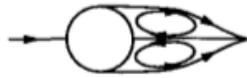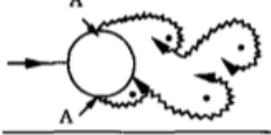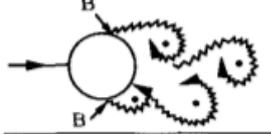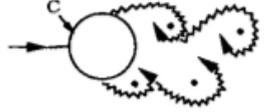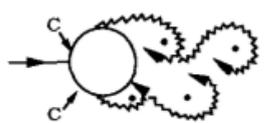
Figure 3.1: Effect of Reynold's Number on Unidirectional Flow Past a Cylinder - Adapted from Zdravkovich (1997)

component and the lift force $(F_{p,L})$ component, found through integration of the surface pressure distribution:

$$F_{p,D} = \int\limits_0^{2\pi} p(R, \theta) R\cos\theta \mathrm{d}\theta, \tag{3.4}$$

and

$$F_{p,L} = \int\limits_0^{2\pi} p(R, \theta) R\sin\theta \mathrm{d}\theta. \tag{3.5}$$

In (3.4) and (3.5), R is the cylinder radius and θ is the angle taken anticlockwise positive about the x-axis with origin at the centre of the cylinder, illustrated in figure 3.2.
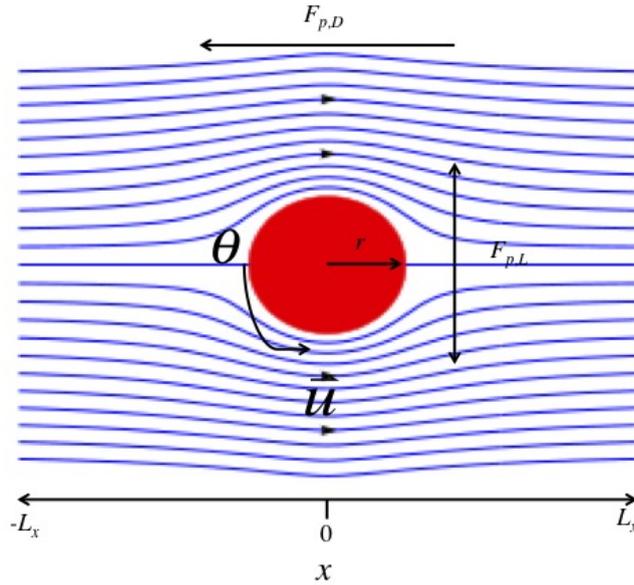
Figure 3.2: Diagram demonstrating the direction of the hydrostatic drag force $(F_{p,D})$ and lift force $(F_{p,L})$ incident on a cylinder in an ideal potential flow, in which $\vec{u}$ denotes direction of flow and θ is the angle on the cylinder.

In an idealised potential flow, the lift force component is equal to zero. However, in a wave field, once the incident wave crest passes and

40

the wave trough reaches the turbine, the flow field is reversed and the wake comes back towards the turbine, resulting in the force loading reversing direction. The directional changes and flow separations breach the prior assumptions of irrotational flow and an inviscid fluid assumed by potential theory (Dean and Dalrymple, 1991), and the pressure integrations in (3.4) and (3.5) are not equal to zero. This deviation from the expected result in symmetrical flow is called *D'Alembert's Paradox*, which occurs due to the unreasonable assumption of potential irrotational flow (Dean and Dalrymple, 1991).

Two more approximate methods are used in practice to calculate the wave-induced force on a monopile, depending on the cylinder diameter-to-wavelength ratio: one for small-diameter cylinders and the other for large-diameter cylinders. In the following sections, the force calculations are based on assumptions that the wave field is comprised of linear waves in either a regular wave field with a single modal wave frequency or in an irregular unidirectional wave field with a range of wave frequencies.

3.2.1 Wave Forces on a Small Diameter Cylinder - Morison equation method

For small-diameter cylinders, where it is assumed that the fluid flow close to the cylinder walls is not altered in the incident wave direction, the Morison equation is commonly used to estimate the total in-line force (Morison et al., 1950). The Morison equation comprises the linear sum of drag and inertia force components, and is evaluated using the undisturbed water particle velocity and acceleration components calculated in the absence of the cylinder. By integrating the representation over the submerged length of a vertical surface-piercing cylinder (that extends

from the bed to above the free surface), the total in-line horizontal force exerted on the cylinder is given by

$$F_M = \int\limits_{z=-h}^{z=\eta} \left[\frac{1}{2}\rho C_d D u |u| + \rho C_m \frac{\pi D^2}{4}\dot{u} \right] dz \qquad (3.6)$$

where the in-line horizontal velocity component u and the in-line horizontal acceleration component $\dot{u}$ can be determined from (2.13) and (2.36), respectively, for regular wave loading, or from (2.34) and (2.35), respectively, for irregular wave loading. The second term on the right hand side of (3.6) is the inertia force, a combination of the force produced by the pressure in an undisturbed wave field (Froude-Krylov force) and the hydrodynamic added mass force (Dean and Dalrymple, 1991). The added mass force results from the force of the fluid acting on the submerged part of the structure. Viscous effects in the boundary layer on the cylinder wall induce flow separation leading to the formation of a vortex street wake at $KC > 3$ (Faltinsen, 1990).

The drag (C_d) and inertia (C_m) coefficients are usually determined experimentally. Results from many experimental tests have been compiled (see e.g. (Roshko, 1961), (Bearman et al., 1985)) and accepted values of C_d at a range of Re values for a smooth cylinder are presented in figure 3.3, where it is assumed that the drag coefficient remains constant over the length of the cylinder.

Around $Re > 1 \times 10^5$, it can be seen in figure 3.3 that there is a drop in the C_d value before it increases again, corresponding to the so-called drag crisis. In oscillatory flow, when $KC < 5$, the flow regime is considered to be inertia-dominant and it has been shown, by Wang (1968), that for high Re values and low KC values (i.e. high β, where $\beta = \dfrac{Re}{KC}$, values),
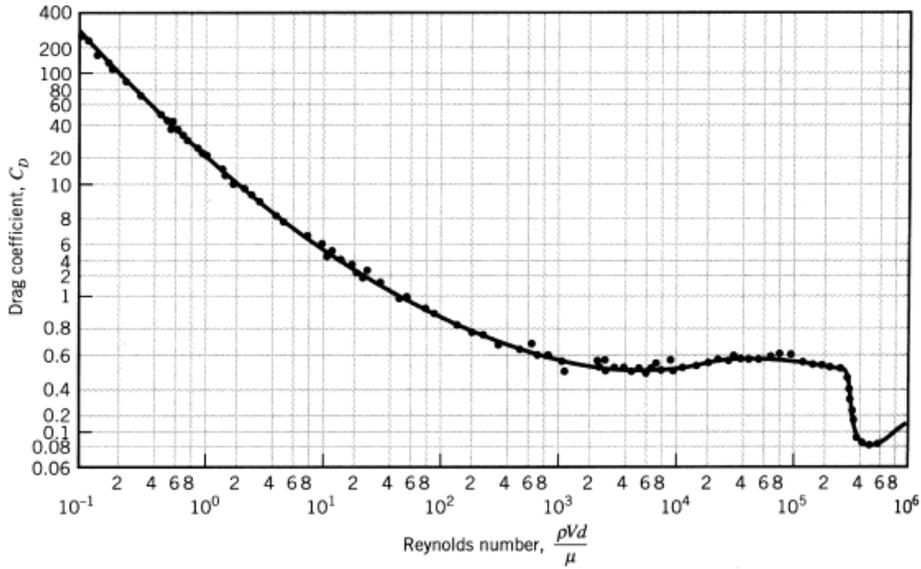
Figure 3.3: Experimental drag coefficient values as a function of Reynold's number for a smooth infinitely long cylinder in unidirectional flow. Image from Schlichting (1960).

the drag and inertia coefficients can be calculated from

$$C_d = \frac{3\pi^3}{2KC}\left[(\pi\beta)^{-1/2} + (\pi\beta)^{-1} - \frac{1}{4}(\pi\beta)^{-3/2}\right] \tag{3.7}$$

and

$$C_m = 2 + 4(\pi\beta)^{-1/2} + (\pi\beta)^{-3/2}. \tag{3.8}$$

Figure 3.4 shows the behaviour of the drag coefficient with Keulegan-Carpenter number for different β values; although it should be noted that the β-values are below those expected for a monopile in waves at the Teesside site.

Ishida and Iwagaki (1978) applied an alternative method introduced by Borgman (1965) to calculate the force spectrum per unit length due to irregular waves in the frequency domain (Sumer and Fredsøe, 2006). The

43
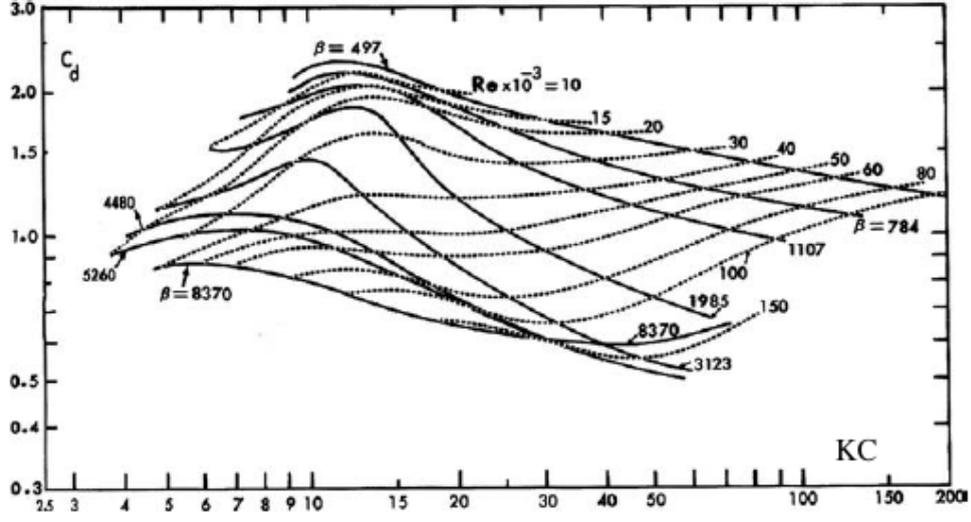
Figure 3.4: Values of C_d versus KC for a range of β values. Adapted from Sarpkaya (1976)

Borgman method for the first approximation of the wave force spectrum at a specified height on the cylinder is given by

$$S(f)_{F_B} = \frac{8 f_d^2 \omega_u^2}{\pi} S(f)_u + f_m^2 S(f)_{\dot{u}}, \qquad (3.9)$$

where the drag and inertia force magnitude values f_d and f_m are related to the Morison coefficients C_d and C_m by

$$f_d = \frac{1}{2}\rho C_d D \quad \text{and} \quad f_m = \rho C_m \frac{\pi D^2}{4}, \qquad (3.10)$$

and $S_u(f)$ and $S_{\dot{u}}(f)$ are the power spectral densities of the in-line velocity and acceleration components, respectively, and

$$\omega_u^2 = 2 \int_0^\infty S_u(f). \qquad (3.11)$$

Predictions from this method can be compared in the frequency domain to the total in-line force spectrum computed as the Fourier transform of

44

the horizontal force time series for irregular waves, calculated using the Morison equation.

3.2.2 Wave forces on a large diameter cylinder - Diffraction Method

Linear diffraction theory applies to inertia-dominated wave flow past a large-diameter cylinder when the ratio of the diameter-to-wavelength $\geq$ 0.2. In this range, diffracted waves are produced by a combination of waves reflected from the cylinder and the undisturbed incident wave field. The initial undisturbed incident wave field potential from (2.6) can be written in complex notation as

$$\phi = \text{Re}\left[-\frac{ag}{\omega} \frac{\cosh k\,(h+z)}{\cosh kh} \text{e}^{i(kx-\omega t)} \right]. \tag{3.12}$$

Using polar coordinates (r, θ) in the horizontal plane, the incident wave potential that satisfies the polar form of Laplace's equation and the kinematic and dynamic free surface boundary conditions (MacCamy and Fuchs, 1954) is given by the standard form

$$\phi_I = -\frac{ga}{\omega} \frac{\cosh k\,(h+z)}{\cosh kh} \left[\sum_{m=0}^{\infty} \epsilon_m (i)^m J_m(kr) \cos m\theta \right] e^{-i\omega t}, \tag{3.13}$$

where $i = \sqrt{-1}$, J_m is the Bessel function of the first kind of order m and ϵ_m equals 1 when $m=0$ and 2 for $m > 0$. As the incident wave impacts upon the cylinder, a reflected wave is radiated outwards and interacts with the incident wave. Combining the undisturbed incident potential ϕ_I and a scattered potential ϕ_R, MacCamy and Fuchs (1954) obtained the following analytical solution for the diffracted velocity potential

$$\phi_D = \phi_I + \phi_R =$$

$$\text{Re}\left\{\frac{ga}{\omega}\frac{\cosh k(h+z)}{\cosh kh}e^{-i\omega t}\left\{\sum_{m=0}^{\infty}\epsilon(i)^m\cdot\right.\right.$$

$$\left.\left.\left[J_m(kr) - \frac{J_m'(kR)}{J_m'(kR) - iY_m'(kR)}\left(J_m(kr) + iY_m(kr)\right)\right]\right\}cosm\theta\right\}.$$
(3.14)

where Y_m is the Bessel function of the second kind of order m and R represents the cylinder radius.

On the cylinder wall, the radial distance from the centre of the column is $r = R$. By definition, $z = r\cos\theta$, where θ refers to the location on the cylinder as measured anti-clockwise from the centre line in the direction of flow, as in (3.4) and (3.5). The diffracted surface elevation η_D is found from the linearised Bernoulli equation (2.5),

$$\eta_D = -\frac{1}{g}\frac{\partial \phi_D}{\partial t},$$
(3.15)

and applying the diffracted potential in (3.14) gives the linear diffracted surface elevation as

$$\eta_D = a\sum_{m=0}^{M}\varepsilon_m\left(i\right)^{-m}$$

$$\cdot\left(J_m(kr) - H_m^{(1)}(kr)\frac{J_m'(kR)}{H_m^{(1)'}(kR)}\right)\cos m\theta. \quad (3.16)$$

where $H_m^{(1)}$ is the Hankel function of the first order, defined as

$$H_m^{(1)}(kr) = J_m(kr) + iY_m(kr).$$
(3.17)

Standard diffraction analysis assumes regular monochromatic waves and can overestimate wave heights in the vicinity of an obstacle in a given sea state (Goda, 1985). The diffracted wave height in an irregular wave field is derived from the superposition of the diffracted wave solution obtained for each individual wave component, where frequencies of the radially outward moving diffracted waves correspond to frequencies of the incident waves (Swan and Sheikh, 2014). Linear superposition allows the irregular diffracted solution to be expressed as

$$
\eta_{\mathrm{D}} = Re\Bigg\{ \sum_{n=1}^{N} a_n e^{-i\omega t + \psi_n} \cdot \Bigg[\sum_{m=0}^{M} \epsilon_m (i)^m
$$
$$
\cdot \left(J_m(k_n r) - H_m^{(1)}(k_n r) \frac{J_m'(k_n R)}{H_m^{(1)'}(k_n R)} \right) \cos m\theta \Bigg] \Bigg\}. \quad (3.18)
$$

It should be stressed that (3.18) is only valid for linear diffracted waves, and so does not hold when nonlinear diffraction becomes significant.

Following the steps outlined in Section 2.3, where the dependency on frequency f is implied, the diffracted surface elevation spectrum $S_{\eta,D} = \frac{1}{F_s N} |\mathrm{FFT}(\eta_D)|^2$, is evaluated, and from $S_{\eta,D}$, the irregular diffracted water particle kinematics, u_D and w_D, can be determined (where (2.32) is implemented to calculate the individual diffracted amplitudes from the diffracted wave spectrum).

The total wave force on a large-diameter cylinder can also be determined from diffraction theory. As in (3.4), the in-line force can be determined through integration of the surface pressure. The pressure field can then be obtained from the unsteady Bernoulli equation (2.4), and the resulting in-line diffracted force per unit length given by MacCamy

47

and Fuchs (1954) is

$$F_D = \frac{2\rho g H}{k} \frac{\cosh k(h+z)}{\cosh kh} G(kR) \cos\left(\omega t - \chi\right), \qquad (3.19)$$

where

$$G(kR) = \frac{1}{\sqrt{J_1'(kR)^2 + Y_1'(kR)^2}} \quad \text{and} \quad \tan\chi = \frac{J_1'(kR)}{Y_1'(kR)}.$$

where the total diffraction force can be found through integration of (3.19) vertically along the submerged length of the cylinder.

Similarly, the irregular in-line diffracted force can be expressed as the sum of each individual diffracted wave force component, or

$$F_D = 2\rho g \sum_{n=1}^{N} \frac{a_n}{k_n} \frac{\cosh k_n\left(h+z\right)}{\cosh k_n h} \cdot G_n(k_n R) \cos\left(w_n t - \alpha_n + \psi_n\right). \quad (3.20)$$

The diffracted force spectrum can be found by the same method as introduced in Section 2.3, where the diffracted force spectrum can be determined by FFT of the diffracted force,

$$S(f)_{F_D} = \frac{1}{F_s N} |\text{FFT}(F_D)|^2, \qquad (3.21)$$

where again F_s is the sampling frequency and N are the number of frequency bins.

It must be noted that the diffraction method only resolves the first-order terms and neglects higher-order terms, the values of which can be non-negligible. Improvements to the methods above could be made by attempting to determine higher-order diffraction terms using a method such as that presented by Chau and Eatock Taylor (1992).

3.3 Transfer Function Derivation

A method is suggested here to determine an expression for the diffracted surface elevation from any input sea state containing waves within the linear regime. Recalling that the significant wave height H_s remains the primary factor on CTV access, the method proposed will allow the diffracted significant wave height $H_{s,D}$ to be calculated from the diffracted surface elevation spectrum $S_{\eta,D}$. Additional parameters such as the diffracted water particle, velocities, accelerations and wave pressures can then also be determined from $S_{\eta,D}$.

The power transfer function $H_T(f)$, which relates the autocorrelation of the input and its spectral density as a Fourier transform pair correlates the input spectrum $S(f)_\eta$ with the output diffracted spectrum $S(f)_{\eta,D}$, and can be found using the Wiener-Khinchin (WK) theorem (Fuller, 1996), which is given for a general case by

$$|H_T(f)|^2 = \frac{S(f)_y}{S(f)_x} \tag{3.22}$$

where $S(f)_y$ represents the diffracted spectral function, $S(f)_x$ represents the inlet spectral function and $|H_T(f)|^2$ is known as the transfer function. With this method, for any input spectral function, the diffracted surface elevation spectrum can be found from (3.22), and the water particle kinematics and diffracted significant wave height can be subsequently found.

It is important to note that the diffracted spectrum and water particle kinematics computed using the transfer function cannot be verified because experimental data concerning the surface displacement close to a monopile turbine are not available. However, if values from the diffracted

spectrum calculated with (3.22) can be verified in the future, this would provide another fast method for approximating the diffracted water particle kinematics based on the sea state. Advances in machine learning could also aid in expanding the available sea state data.

3.4 Summary

In this chapter, the loading on a fixed structure, represented throughout as a smooth cylinder, due to waves has been considered. Wave loading is quantified using the Morison equation for viscous flow and the linear diffraction formulation by MacCamy and Fuchs (1954) for inertia-dominant flow. Following the process proposed in this chapter, an analytical method has been presented for determining the diffracted wave field and water particle kinematics within the vicinity of a bottom-fixed surface-piercing monopile in long-crested waves for any given unidirectional sea state or surface displacement time-series. Predictions obtained through this technique will be further compared to the predictions of a numerical model (see Chapter 4) to investigate the suitability of the analytical method outlined here.

Chapter 4

Numerical Formulation in OpenFOAM

Chapter Summary

This chapter discusses those numerical methods utilising computational fluid dynamics (CFD) for modeling the wave motion in a numerical wave tank (NWT) containing a surface-piercing vertical cylinder. CFD attempts to solve the governing equations numerically, subject to appropriate boundary conditions, without any input from analytic methods. It is usually based on finite difference (FD), finite element (FE) or finite volume (FV) discretisations of the spatial and temporal equations governing fluid flow. The specific CFD package used in the present research is the open-source C++ library of fluid solvers, OpenFOAM. This chapter will focus on the CFD method relevant to OpenFOAM, although the methods described here also apply to other open-source and commercial solvers. The CFD methods and solvers discussed throughout this section relate to OpenFOAM version 2.4.0, introduced in May 2015.

4.1 Introduction

The analytical solutions presented in Chapters 2 and 3 neglect many factors that influence fluid flow, such as the influence of viscosity on the flow in the vicinity of the cylinder and the influence of shallow water depth on wave propagation. Due to the complexity of fluid flow, exact solutions for the nonlinear governing equations are usually not available for engineering purposes. Consequently, numerical simulations are used to provide approximate solutions. Recent advances in computing power have made it possible to simulate wave flow and fluid-structure interactions with increasing accuracy. CFD is an analysis method of fluid flow and associated phenomena, based on mass and momentum conservation laws. CFD codes are developed through the following process (Versteeg and Malalasekera, 2007):

1. Define the geometry and computational domain, and then generate a representative discretised grid or mesh.

2. Determine the physical fluid properties of interest and the governing equations that model the physics of the system.

3. Specify the appropriate boundary conditions for the system.

4. Adapt the physical governing equations to the entire computational mesh and discretise the continuous partial differential equations into an algebraic system of equations. Implement the boundary conditions.

5. Apply a numerical scheme to solve the discretised algebraic equations.

6. Post-process the numerical results using visualisation, or tracking field values throughout the domain.

At the time of writing, commercial CFD packages are more user-friendly than OpenFOAM, but incur considerable expense with the user having little control over the solution method. Open-source CFD packages are becoming more widespread and their validity has already been acknowledged in the industry (Jasak, 2009). OpenFOAM is a widely used open-source CFD package with a growing community of active users who contribute to the code and provide user support through online forums. Solvers, pre-processing utilities, and applications in OpenFOAM are written in C++ such that users have the ability to view and change the original source code. This freedom allows users to apply the format used in OpenFOAM scripts to write new solvers specific to the relevant area of interest. Results from OpenFOAM have been comprehensively verified (e.g. (Higuera et al., 2013, Lysenko et al., 2013, Davidson et al., 2015)). Taking the foregoing into account, OpenFOAM was chosen as the CFD package for this project to allow the greatest amount of user freedom while avoiding the costs and restrictions that surround use of commercial software.

OpenFOAM permits the use of a very large number of mesh elements within the computational domain and can be easily parallelised, which can significantly reduce the computational time needed for CFD simulations. As open-source software, OpenFOAM is less user-friendly than commercial CFD software and requires a significant amount of time to become proficient. However, the online support community is large and active. All CFD simulations throughout this project were conducted using OpenFOAM and this chapter will discuss the background and overview

of CFD implementation in OpenFOAM.

An overview of the mass conservation and Navier-Stokes momentum equations for fluid motion is presented in Section 4.2. Section 4.3 discusses the finite volume method for discretising the geometry and partial differential equations for fluid flow. Finite volume and finite element methods use an integral formulation of the governing equations, unlike the finite difference method. The finite difference method uses a Taylor series expansion to describe the governing equations in terms of difference terms. The finite element method uses local integration of the governing equations multiplied by a weight residual term (Ferziger and Peric, 2002). The finite volume method uses local integration over each computational cell in turn. For simple geometries, all three methods produce the same or very similar outputs. OpenFOAM uses the finite volume method for greater flexibility in modelling geometric shapes. Turbulence models were not included in the present analysis as the area of interest lay beyond the cylinder wall boundary layer.

The applicable boundary conditions are examined in Section 4.4 and the numerical solvers are outlined in Section 4.5. An overview of the OpenFOAM set-up is given in Section 4.6, and Section 4.7 discusses the use of High Performance Computing (HPC) for CFD applications. Finally, a summary of the numerical formulation is outlined in Section 4.8.

4.2 Numerical Governing Equations

In the undisturbed flow region far away from the cylinder, the velocity potential defined in (2.6) satisfies the Laplace equation's assumption of

an inviscid fluid executing irrotational flow. Close to the cylinder, these assumptions become increasingly invalid due to the influence of viscosity.

The near-cylinder fluid motion is described by the unsteady, incompressible continuity and Navier-Stokes momentum equations. Employing conservation of mass and assuming constant density, the continuity equation can be written as

$$\nabla \cdot \mathbf{u} = 0, \tag{4.1}$$

where the gradient vector $\nabla = \mathbf{i}\frac{\partial}{\partial x} + \mathbf{j}\frac{\partial}{\partial y} + \mathbf{k}\frac{\partial}{\partial z}$ and $\mathbf{u}$ is the flow velocity vector $\mathbf{u} = \mathbf{i}u + \mathbf{j}v + \mathbf{k}w$. From Newton's second law, the rate of increase in momentum is equal to the sum of incident forces, such as gravitational acceleration. The incompressible Navier-Stokes equation of momentum conservation is

$$\underbrace{\frac{\partial}{\partial t}(\mathbf{u})}_{\text{temporal derivative}} + \underbrace{\nabla \cdot (\mathbf{uu^T})}_{\text{convective term}} - \underbrace{\nabla(\nu\nabla\mathbf{u})}_{\text{diffusive term}} = \underbrace{-\frac{1}{\rho}\nabla p}_{\text{source term}} - \underbrace{g \cdot x}_{\text{body force}}, \tag{4.2}$$

in which ν is the kinematic viscosity and p represents the total pressure. The total pressure is a combination of the dynamic and hydrostatic pressure contributions.

The Navier-Stokes equations are typically solved by discretisation in space and time and then by constructing a system of linear algebraic equations that can be solved using computational methods (Ferziger and Peric, 2002). The discretisation and solution process is discussed in more detail in Section 4.3.

For multiphase environments with two immiscible fluids, such as free

surface flows, the flow of both the fluids must be accounted for. The time-averaged Reynolds Averaged Navier-Stokes (RANS) formation for multiphase flow accounts for the flow of both the air and the water. RANS is normally used to describe turbulent flow with high Re values. The compressible version of the RANS equation that is applied in Open-FOAM is given by Rusche (2002)

$$\frac{\partial \rho \mathbf{u}}{\partial t} + \nabla \cdot \left[\rho \mathbf{u} \mathbf{u}^{\mathrm{T}} \right] = -\nabla p^* - g \cdot x \nabla \rho$$
$$+ \nabla \cdot \left[\mu \nabla \mathbf{u} + \rho \tau \right] + \sigma_T \kappa_\alpha \nabla \alpha, \quad (4.3)$$

where μ is the coefficient of dynamic viscosity, ρ is the fluid density, the velocity field is given in Cartesian coordinates by $\mathbf{u} = (u, v, w)$, p^* is pressure in excess of hydrostatic, σ_T is the surface tension coefficient (0.07 kg/s^2 at the air-water interface for 20° water), κ_α is the surface curvature (see e.g. Ubbink and Issa (1999)), α is a scalar field fluid volume fraction tracking the location of the fluid at the interface, and τ is the Reynolds stress tensor given by

$$\tau = \frac{2}{\rho} \mu_t \mathbf{S} - \frac{2}{3} k \mathbf{I}, \quad (4.4)$$

in which μ_t is the dynamic eddy viscosity, $\mathbf{S}$ is the strain rate tensor ($^1/_2(\nabla \mathbf{u} + (\nabla \mathbf{u})^T)$), and k is the turbulent kinetic energy per unit mass (Jacobsen et al., 2011). For laminar flow, the τ term is assumed to be zero. Equation (4.3) can be further simplified by assuming that the surface tension term makes negligible contribution to the fluid flow. Therefore, for laminar, incompressible flow, the convective form of (4.3) is

$$\frac{\partial \mathbf{u}}{\partial t} + \nabla \cdot \left[\mathbf{u}\mathbf{u}^T \right] - \nabla \cdot \left[\nu \nabla \mathbf{u} \right] = -\frac{1}{\rho} \nabla p^* - g \cdot x. \qquad (4.5)$$

The dependence of velocity on pressure inherent in the RANS equations requires special computational treatment, further discussed in Section 4.5.

4.2.1 Free Surface Treatment - Volume of Fluid Approach

The volume of fluid (VOF) method is used to determine the location of the interface by calculating the volume fraction (water-to-air) present in each cell at the interface (Hirt and Nichols, 1981). The VOF process is a storage-saving method based on the Marker and Cell (MAC) technique, where values at several points in each cell are computed and the volume fraction function α defined. Averaging α over each point then gives one value per cell and this is calculated with the transient advection equation

$$\frac{\partial \alpha}{\partial t} + \nabla \cdot \left[\mathbf{u}\alpha \right] + \nabla \cdot \left[\mathbf{u_r}\alpha(1-\alpha) \right] = 0, \qquad (4.6)$$

where

$$\alpha = \begin{cases} 0, & \text{air} \\ 1, & \text{water} \\ 0 \leq \alpha \leq 1, & \text{interface}. \end{cases}$$

The artificial compression term $[\mathbf{u_r}\alpha(1-\alpha)]$ is necessary to restrict smearing of the interface. The MAC method allows only a value of 0 or 1 within the cell, whilst the allowance of a fraction for α in VOF enables a more

accurate determination of the numerical interface location. From (4.6), it is straightforward to determine the spatial variation of any fluid property based on the fraction of fluid in each cell using the equation

$$Q = \alpha Q_{water} + (1 - \alpha)Q_{air}, \tag{4.7}$$

where Q represents a specific property, such as viscosity ν, density ρ, velocity $\mathbf{u}$ or pressure p. All gradient and Laplacian terms in (4.3) and (4.6) are then discretised (see Section 4.3) and applied to the cells in the computational fluid domain. A visualisation of the initial volume fraction scalar field values for a sample computational domain following application of VOF is given in figure 4.1.
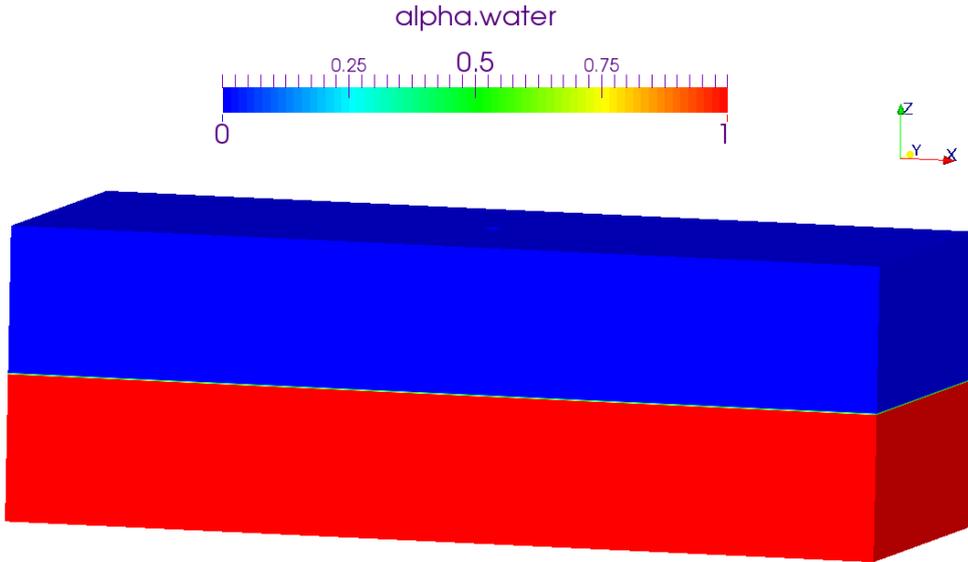
Figure 4.1: The volume fraction function α values within the computational domain, evaluated using the VOF method. Blue areas indicate the air, red indicates water and the thin green line is the interface location.

The width of the interface, the thin green line in figure 4.1, is dependent

on the grid resolution at the free surface.

4.3 Finite Volume Method for Equation Discretisation

The partial differential equations (PDEs) in Section 4.2 are typically solved by first integrating the continuous Navier-Stokes equations over both the spatio-temporal and solution domain (Versteeg and Malalasekera, 2007). The integrated spatio-temporal and solution domain terms are next discretised into a finite number of computational elements and time steps, respectively. The finite volume method (FVM) is applied to discretise the continuous partial differential equations into arbritrary polyhedral non-overlapping cells, or control volumes (Weller et al., 1998). The domain is first divided into discrete nodal points. Cell boundaries (or faces) of the discrete control volumes are located at the midpoint of neighbouring nodes, such that each node lies entirely within a control volume (or mesh element) (Versteeg and Malalasekera, 2007), illustrated in figure 4.2. Each control volume can then be defined as a 3D element bounded on all sides by planar faces (see figure 4.3).

In figure 4.3, point P is the centroid of the "owner" cell, $\mathbf{S}$ is the face area vector pointing directly outwards from face f, and N denotes the centroid of the "neighbouring" cell, which shares one face with the owner cell. The control volume is designated by CV.

The discretised Navier-Stokes and VOF equations can then be applied to the centroid point P within each cell (Versteeg and Malalasekera, 2007).

FVM requires that the governing equations be satisfied over the entire control volume and at point P. The total volume of the control volume
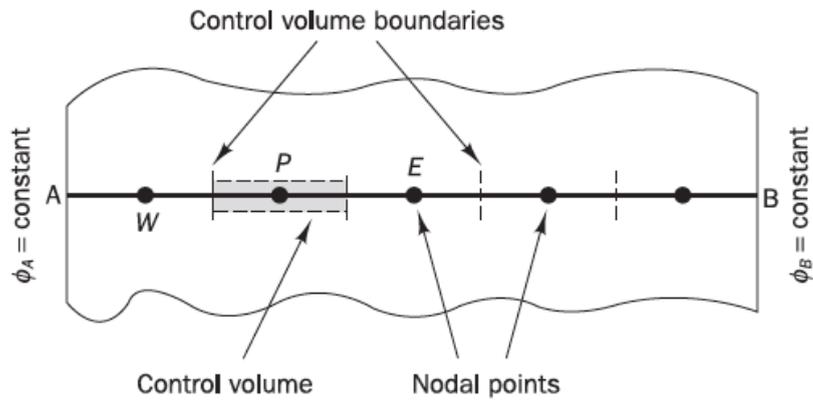
Figure 4.2: Illustration of node and control volume location during grid generation with the FV method - Image from Versteeg and Malalasekera (2007).
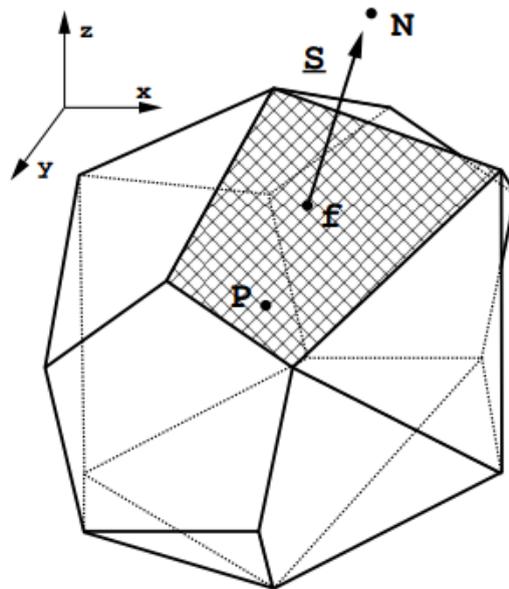
Figure 4.3: Illustration of typical 3D control volume. Image reproduced from Jasak (1996)

about the centroid is defined in terms of the location of P by

$$\int_{CV} (\mathbf{x} - \mathbf{x_p}) \, dCV = 0, \tag{4.8}$$

where the vectors $\mathbf{x}$ and $\mathbf{x_p}$ are locations within the cell and at the centroid, respectively. Equation (4.8) is equal to zero because P is the centroid.

The forms of the Navier-Stokes equations given by (4.2), (4.3) and (4.5) are all specific versions of a fluid transport equation. To discuss discretisation of transport equations more generally, an incompressible transport equation of property ζ is first given by

$$\underbrace{\frac{\partial \zeta}{\partial t}}_{\text{temporal derivative}} + \underbrace{\nabla \cdot (\mathbf{u}\zeta)}_{\text{convective term}} - \underbrace{\nabla \cdot (\Gamma_\zeta \nabla \zeta)}_{\text{diffusive term}} = \underbrace{\frac{1}{\rho} S_\zeta \zeta}_{\text{source term}} , \tag{4.9}$$

where $\mathbf{u}$ is the velocity vector, Γ_ζ describes the rate of diffusion of the field value ζ and the source term $S_\zeta \zeta$ depends on the physical properties of the fluid.

To discretise the transport equations with FVM, (4.9) is first written in integral form:

$$\int_t^{t+\Delta t} \left[\frac{\partial}{\partial t} \int_{CV} \zeta dCV + \int_{CV} \nabla \cdot (\mathbf{u}\zeta) \, dCV - \int_{CV} \nabla \cdot (\Gamma_\zeta \nabla \zeta dCV) \right] dt$$
$$= -\frac{1}{\rho} \int_t^{t+\Delta t} \left(\int_{CV} S_\zeta \zeta dCV \right) dt, \tag{4.10}$$

where ζ in this case represents a field value such as the horizontal velocity component u, t is time, Δt is the time increment, and CV is the control

volume. At the centroid P, ζ can be given in spatial or temporal terms by

$$\zeta(\mathbf{x}, t) = \zeta_{\mathrm{P}} + (\mathbf{x} - \mathbf{x_p}) \cdot (\nabla \zeta)_{\mathrm{P}} \tag{4.11}$$

and

$$\zeta(\mathbf{x}, t + \Delta t) = \zeta^t + \Delta t \left(\frac{\partial \zeta}{\partial t} \right)^t, \tag{4.12}$$

where $\zeta_{\mathrm{P}} = \zeta(\mathbf{x_p})$ and $\zeta^t = \zeta(t)$. A second-order discretisation method is required to minimise errors due to the Laplacian in the diffusive term. Gauss' Theorem and identities presented in Section 4.3.1 below, are applied to discretise each of the terms in (4.10) separately.

4.3.1 Gauss' Theorem for Discretisation

The spatial terms in (4.10) are described using a standard Gaussian finite volume integration. Gauss' theorem, which can be applied to any CV shape, is given by

$$\int_{CV} \nabla \cdot \mathbf{a} dCV = \int_S \mathbf{n} \cdot \mathbf{a} dS, \tag{4.13}$$

where $\mathbf{a}$ is an arbitrary vector and S represents the control volume surface. In general, the discretised second-order accurate form of Gauss' Theorem over all i surfaces is

$$\int_{CV} \nabla \cdot \zeta = \oint_{dCV} d\mathbf{S} \cdot \zeta = \sum_i S_i \cdot \zeta_i. \tag{4.14}$$

Equation (4.14) can be used to describe the convective and diffusive terms as they apply over all surface faces S_i. Figure 4.4 shows a simplified 2-

D element that represents the face bounding the surface of the control volume (denoted as f in figure 4.3).
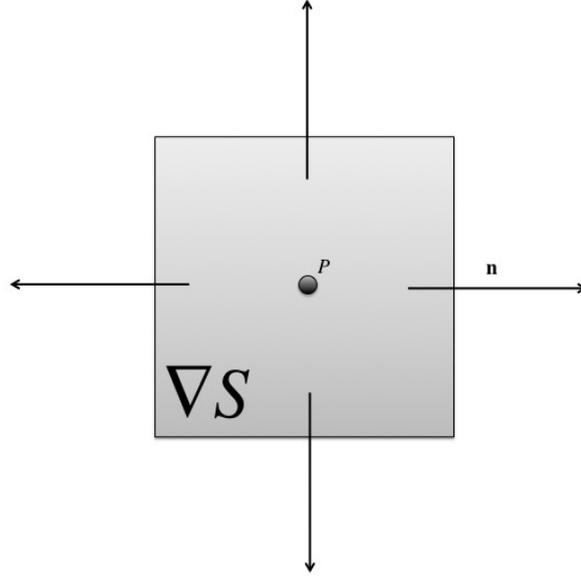
Figure 4.4: Illustration of simple quadrilateral 2D control volume, where midpoint P, outward normal vector $\mathbf{n}$, and surface area ∇S are labelled

To rewrite the terms in the transport equation (4.10), use will be made of three identities arising from Gauss' Theorem,

$$\int_{CV} \nabla \cdot \mathbf{a} \, dCV = \oint_{\partial CV} d\mathbf{S} \cdot \mathbf{a}, \qquad (4.15)$$

$$\int_{CV} \nabla \zeta \, dCV = \oint_{\partial CV} \zeta d\mathbf{S}, \qquad (4.16)$$

and

$$\int_{CV} \nabla \mathbf{a} \, dCV = \oint_{\partial CV} \mathbf{a} \, d\mathbf{S}, \qquad (4.17)$$

where ∂CV is the closed surface bounding the control volume CV and $d\mathbf{S}$ represents a surface element with associated outward-pointing normal on ∂CV. From the variation of ζ given in (4.11), the total spatial variation

over the entire control volume is

$$\int_{CV} \zeta(\mathbf{x}) \approx \int_{CV} [\zeta_P + (\mathbf{x} - \mathbf{x_P} \cdot \nabla \zeta_P] \, dV$$
$$= \zeta_P \int_{CV} dV + \left[\int_{CV} (\mathbf{x} - \mathbf{x_p}) dV \right] \cdot (\nabla \zeta)_P \qquad (4.18)$$
$$= \zeta_P \ CV.$$

The second integral on the right-hand-side is again equal to zero as P is the control volume centroid.

The identities in (4.15), (4.16), (4.17) can be used to calculate the total variation of ζ across the control volume as the sum of the integrals across each face. The face area vector $\mathbf{S}$ points outward if face f is "owned" by P and inward if it is "owned" by N. Hence, $\mathbf{S}$ can be described as the difference between the owner cell value and the neighbouring cell value, as in

$$\sum_f \mathbf{S} \cdot \mathbf{a} = \sum_{owner} \mathbf{S}_f \cdot \mathbf{a}_f - \sum_{neighbour} \mathbf{S}_f \cdot \mathbf{a}_f. \qquad (4.19)$$

Throughout this work, $\mathbf{S}$ refers to the total direction, inclusive of both P and N. Gauss' Theorem will be applied separately to each integral term in (4.10).

Convective Term

The convective term for a scalar ζ in the transport equation, $\nabla \cdot (\mathbf{u}\zeta)$, can be expressed over all faces using (4.19)

$$\int_{CV} \nabla \cdot (\mathbf{u}\xi)dV = \sum_f \mathbf{S} \cdot (\mathbf{u}\xi)_f$$

$$= \sum_f \mathbf{S} \cdot (\mathbf{u}_f)\,\xi_f \qquad (4.20)$$

$$= \sum_f F\xi_f$$

where $F = \mathbf{S} \cdot (\mathbf{u}\xi)_f$ represents the volume flux through the face. The variable $\mathbf{u}\xi$ is described in the middle of the face and $\mathbf{S}$ is the outward-pointing face area vector. The value on the cell face is dependent on both the owner cell value ξ_P and the neighbour cell value ξ_N.

The face value ξ_f in (4.20) can be interpolated from the centroid values of cells sharing the face. Interpolation is undertaken using a differencing scheme. Regardless of the differencing scheme used, the constraint on ξ_f is that its value must remain bounded within its original distribution. A number of differencing schemes are available in OpenFOAM and those schemes used in this study are outlined below.

Assuming a linear variation of ξ across the face, the following expression can be used to describe ξ_f in terms of the centroid values ξ_P and ξ_N,

$$\xi_f = f_x\xi_P + (1 - f_x)\xi_N, \qquad (4.21)$$

where f_x is the ratio of the distances $\overline{\text{fN}}$ and $\overline{\text{PN}}$,

$$f_x = \frac{\overline{\text{fN}}}{\overline{\text{PN}}}. \qquad (4.22)$$

This type of second-order differencing is called **Central Differencing**. Central differencing is usually more accurate but can cause non-physical oscillations and violate the criteria for boundedness at or near boundaries.

To avoid these oscillations, **Upwind Differencing** can be used (Versteeg and Malalasekera, 2007). OpenFOAM utilises a simple first-order accurate upwind method where ξ_f is dependent on the flow direction and cell orientation, such that

$$\xi_f = \begin{cases} \xi_P & \text{for} \;\; F \geq 0 \\ \xi_N & \text{for} \;\; F \leq 0, \end{cases} \tag{4.23}$$

in which F denotes flow direction (≥ 0 denotes flow from cell P and ≤ 0 is flow from cell N). Although the upwind differencing scheme insures boundedness, it violates the necessity for second-order accuracy (required by the Laplacian term in the transport equation), potentially causing instabilities in the model. A mixture of central and upwind differencing can be used to overcome these issues.

Diffusive Terms

The diffusion term in the transport equation (4.10) can be written as

$$\int_{CV} \nabla \cdot (\Gamma_\xi \nabla \xi) = \sum_f \mathbf{S} \cdot (\Gamma_\xi \nabla \xi) \tag{4.24}$$

$$= \sum_f (\Gamma_\xi)_f \, \mathbf{S} \cdot (\nabla \xi)_f \,. \tag{4.25}$$

The quality and alignment of the computational mesh elements affect the calculation method and accuracy for $\mathbf{S} \cdot (\nabla \xi)_f$. For orthogonal meshes where the outward pointing normal vector is exactly perpendicular to the vector connecting the cell centres, the following expression for the gradient of ξ at the face is valid

$$S \cdot (\nabla \xi)_f = |\mathbf{S}| \frac{\xi_\mathrm{N} - \xi_\mathrm{P}}{|\mathbf{d}|}, \tag{4.26}$$

where $\mathbf{d}$ represents the vector connecting the cell centres. For non-orthogonal meshes where $\mathbf{S}$ and $\mathbf{d}$ are not perpendicular to each other, a non-orthogonality correction term is needed (see e.g. Ferziger and Peric (2002)). It is more common for cells to be non-orthogonal than orthogonal and therefore a more general expression for $\mathbf{S} \cdot (\nabla \xi)_f$ splits the products into an orthogonal component $\mathbf{\Delta}$ and the non-orthogonal correction component $\boldsymbol{\kappa}$,

$$\mathbf{S} \cdot (\nabla \xi)_f = \underbrace{\mathbf{\Delta} \cdot (\nabla \xi)_f}_{\text{orthogonal term}} + \underbrace{\boldsymbol{\kappa} \cdot (\nabla \xi)_f}_{\text{non-orthogonal correction}}, \tag{4.27}$$

where the vectors $\mathbf{\Delta}$ and $\boldsymbol{\kappa}$ must satisfy the condition $\mathbf{S} = \mathbf{\Delta} + \boldsymbol{\kappa}$, and $\mathbf{\Delta}$ is selected to be parallel to vector $\mathbf{d}$.

In OpenFOAM, the mesh quality can be checked with the *checkMesh* utility. The *checkMesh* utility gives information on mesh features such as non-orthogonality and the mesh aspect ratio (AR), which for a 3D control volume is calculated from

$$\mathrm{AR} = \frac{1.0}{6.0} \times \frac{|ax| + |ay| + |az|}{CV^{2/3}}, \tag{4.28}$$

where ax, ay and az are the areas of the bounding faces in the x, y and z directions and CV is the total cell volume. It is desirable that AR remain as close to unity as possible (Ferziger and Peric, 2002).

Once the non-orthogonal corrector has been incorporated into the discretisation, the final form of the discretised diffusion is defined. For the orthogonal component where $\mathbf{d}$ and $\mathbf{\Delta}$ are parallel,

$$\boldsymbol{\Delta} \cdot (\nabla \xi)_f = |\boldsymbol{\Delta}| \frac{\xi_{\mathrm{N}} - \xi_{\mathrm{P}}}{|\mathbf{d}|}, \tag{4.29}$$

and combining the non-orthogonal term, (4.27) can be written as

$$\mathbf{S} \cdot (\nabla \xi)_f = |\boldsymbol{\Delta}| \frac{\xi_{\mathrm{N}} - \xi_{\mathrm{P}}}{|\mathbf{d}|} + \boldsymbol{\kappa} \cdot (\nabla \xi)_f. \tag{4.30}$$

Source Terms

The source terms can be any function of ξ not described by the convection, diffusion or temporal terms. The discretisation method is dependent on the interaction between source terms and the other terms in the equation. Typically, the source terms can be discretised directly as a combination of linear terms, such as

$$S_\xi(\xi) = Su + Sp\xi, \tag{4.31}$$

where both Su and Sp can depend on ξ.

Temporal Discretisation

Incorporating the discretised terms from the previous sections, and assuming that the control volume is not altered in time, the semi-discretised integral form of the transport equation (4.10) can be rewritten

$$\int_t^{t+\delta t} \left[\left(\frac{\partial \xi}{\partial t} \right)_{\mathrm{P}} CV + \sum_f F \xi_{\mathrm{f}} - \sum_f (\Gamma_\xi)_{\mathrm{f}} \mathbf{S} \cdot (\nabla \xi)_f \right] dt$$
$$= \int_t^{t+\delta t} (Su + SpCV \xi_{\mathrm{P}}) \, dt. \tag{4.32}$$

The time derivative and integral terms are computed using simple differ-

encing from

$$\frac{\partial \xi}{\partial t} = \frac{\xi_P^n - \xi_P^0}{\delta t} \tag{4.33}$$

and

$$\int_t^{t+\delta t} \xi(t) dt = \frac{1}{2}(\xi^0 + \xi^n)\delta t, \tag{4.34}$$

where

$$\xi^n = \xi(t + \delta t) \tag{4.35}$$

and

$$\xi^0 = \xi(t). \tag{4.36}$$

The Crank-Nicolson discretisation method in (4.33) and (4.34) is second-order accurate in time. The fully discretised transport equation then becomes

$$\frac{\xi_P^n - \xi_P^0}{\delta t}CV + \frac{1}{2}\sum_f F\xi_f^n - \frac{1}{2}\sum_f(\Gamma_\xi)_f \mathbf{S} \cdot (\nabla\xi)_f^n$$
$$+ \frac{1}{2}\sum_f F\xi_f^0 - \frac{1}{2}\sum_f(\Gamma_\xi)_f \mathbf{S} \cdot (\nabla\xi)_f^0 \tag{4.37}$$
$$= SuCV_P + \frac{1}{2}SpCV_P\xi_P^n + \frac{1}{2}SpCV_P\xi_P^0.$$

The Crank-Nicolson method requires the face values ξ_f, the gradient $(\nabla\xi)_f$, and the centroid value for each present and previous time step. Face values can be calculated using a differencing scheme such as central differencing, upwind differencing or a combination of both. To determine the centroid value ξ_P, the Crank-Nicolson scheme utilises the algebraic

69

formulation of the momentum conservation equation

$$a_{\mathrm{P}}\xi_{\mathrm{P}} + \sum_{N} a_{\mathrm{N}}\xi_{\mathrm{N}}^{n} = R_{\mathrm{P}}, \tag{4.38}$$

where R_{P} are the source terms. Due to the dependence of ξ_{P}^{n} on the values in neighbouring cells, (4.38) creates an algebraic system of equations,

$$[A][\xi] = [R], \tag{4.39}$$

where A is a matrix containing coefficients a_{P} on the diagonal, coefficients a_{N} in the off-diagonal positions and ξ is the vector for all control volumes. The solution for this system of equations gives the next time-step value for ξ.

Although the Crank-Nicolson method is unconditionally stable, there is no guarantee of boundedness (Ferziger and Peric, 2002, Jasak, 1996). To be sure that the temporal discretisation term is bounded, a first-order accurate Euler method is used instead. Neglecting the face values of ξ and $\nabla\xi$, the old and new values of the convection, diffusion and source terms can be included to give the simplified form of (4.37),

$$\left(\frac{\xi_{\mathrm{P}}^{n} - \xi_{\mathrm{P}}^{0}}{\delta t}\right)CV + \sum_{f} F\xi_{\mathrm{f}} - \sum_{f}(\Gamma_{\xi}) + \mathbf{S} \cdot (\nabla\xi)_{\mathrm{f}} = SuCV + SpCV\xi_{\mathrm{P}}. \tag{4.40}$$

The next time-step value of ξ is given by Euler explicit discretisation to be

$$\xi_{\mathrm{P}}^n = \xi_{\mathrm{P}}^0 + \frac{\delta t}{CV} \left[\sum_{\mathrm{f}} F\xi_f \sum_{\mathrm{f}} (\Gamma_\xi) \cdot \mathbf{S}(\nabla \xi)_{\mathrm{f}} + SuCV + SpCV\xi_{\mathrm{P}} \right] . \quad (4.41)$$

The stability of Euler explicit differentiation relies on the Courant criterion to be met (Courant et al., 1967). The Courant criterion is given by

$$Co = \frac{\Delta t \mid \mathbf{u} \mid}{\Delta x} \leq 1, \quad (4.42)$$

where Δx is the cell length and Δt is the time step. The Courant number should remain below unity so that the fluid particles travel from one cell to the next in a maximum of one time step. This criterion ensures that the time step is not so large that the information inside any cell is skipped. In figure 4.5a, Co is greater than 1 and the fluid flows through more than one mesh element in a single time step, losing information from cells that are skipped. When information is lost, instabilities can cause the solution to diverge or lose accuracy. Figure 4.5b illustrates the situation when the Courant criterion is met and Co remains below 1. Information from each cell is recorded and a numerically stable solution with greater accuracy is achieved. Conversely, it is also possible that Co can be too small, in which case the solution takes too long to converge and over-sampling within one cell can also result in inaccuracies.

To satisfy the Courant criterion and maintain stability, a maximum value for Co is set at 0.5 and an adjustable time step applied, i.e. the time step size decreases when the velocity or cell size decreases and the time step size increases with increasing velocity or larger cell size. For
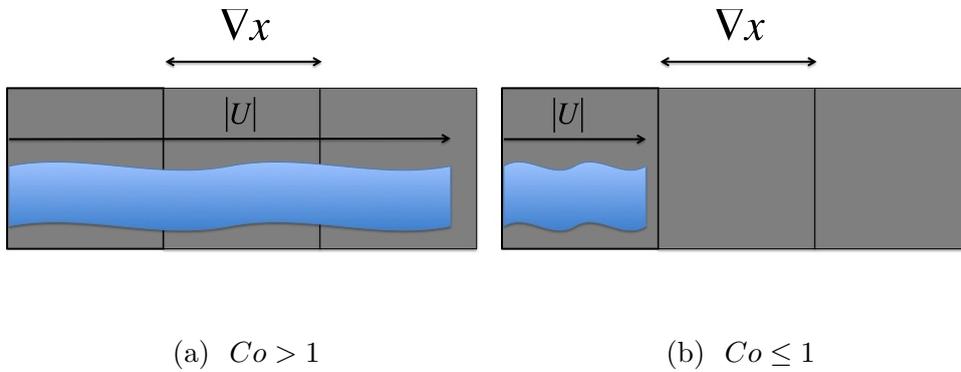
Figure 4.5: Illustration of distance flow travels per time step, dependent on the Courant number.

two-dimensional or three-dimension flow, the Co value must take into account the velocities and cell width in each relevant direction. When simulating multiphase flow with the VOF method, the Courant criterion must also be satisfied for α, which replaces $| \mathbf{u} |$ in (4.42).

4.4 Boundary Conditions

From (4.38), the flow is modelled by the algebraic system of equations,

$$a_{\mathrm{P}}\xi_{\mathrm{P}} + \sum_{\mathrm{N}} a_{\mathrm{N}}\xi_{\mathrm{N}} = R_{\mathrm{P}}.$$

To solve this system of equations for each mesh element, it is necessary to specify the values on the boundaries and, for transient flow, the initial values throughout the domain for all flow field parameters. Specification of the initial conditions can be straightforward by setting each field value according to the desired initial conditions, which are defined by the problem, e.g. fluid flow starts from rest (Ferziger and Peric, 2002). The governing equations must also satisfy the boundary conditions, which are either physical or numerical. Physical boundary conditions are walls, such as the cylinder wall, inlet/outlet conditions, the sea floor and sym-

metry planes. Numerical boundary conditions are used to prescribe either the value on the boundary (Dirichlet), the gradient on the boundary (von Neumann), or a combination of the two (mixed boundary condition). (Versteeg and Malalasekera, 2007).

Prior to solving the equations, the numerical boundary conditions are incorporated into the discretised governing equations. The boundary conditions can therefore be described separately for the convection and diffusion terms in the transport equation. Boundary condition implementation is discussed below.

4.4.1   Numerical Boundary Conditions

Fixed-Value (Dirichlet) Boundary Condition

For a fixed-value boundary condition, the value on the boundary face is denoted by ξ_b. The non-orthogonal corrector in the diffusion term in (4.30) can be neglected because the vector between the cell centre and the boundary face $\mathbf{d}_n$ is normal on the boundary, and is given by

$$\mathbf{d}_n = \frac{\mathbf{S}}{|\mathbf{S}|}\frac{\mathbf{d} \cdot \mathbf{S}}{|S|}. \tag{4.43}$$

From the discretised form of the diffusion term with solely the orthogonal component, the face gradient $\mathbf{S} \cdot (\nabla \xi)_b$ is found using the known value on the cell face at the boundary and the cell centre value (Jasak, 1996), or

$$\mathbf{S} \cdot (\nabla \xi)_{\mathrm{b}} = |\mathbf{S}|\frac{\xi_{\mathrm{b}} - \xi_{\mathrm{P}}}{|\mathbf{d}_n|}. \tag{4.44}$$

The above formulation is valid because the outward pointing normal vector $\mathbf{S}$ and the vector $\mathbf{d}_n$ pointing from the cell centre to the face are parallel.

Fixed-Gradient (von Neumann) Boundary Condition

For a fixed-gradient boundary condition, the boundary value is defined by the dot product of the gradient of ξ and the vector $\mathbf{S}$ as

$$\left(\frac{\mathbf{S}}{|\mathbf{S}|} \cdot \nabla \xi \right)_{\mathrm{b}} = q_{\mathrm{b}}, \tag{4.45}$$

where q_{b} represents the selected gradient value on the boundary. For the convection term, the dot product in (4.45) can be used to calculate the face value of ξ, which is a combination of the centroid value and the assigned gradient value. Recalling again that $\mathbf{S}$ and $\mathbf{d}$ are parallel, in the convection term in the fixed gradient boundary condition gives

$$\xi_{\mathrm{b}} = \xi_{\mathrm{P}} + \mathbf{d}_n \cdot (\nabla \xi)_{\mathrm{b}} \tag{4.46}$$

$$= \xi_{\mathrm{P}} + |\mathbf{d}_n| q_{\mathrm{b}}. \tag{4.47}$$

Applying the dot product again, the gradient value in the diffusion term in the transport equation can be written simply as $|\mathbf{S}| q_{\mathrm{b}}$, and the final discretisation is

$$(\Gamma_\xi) |\mathbf{S}| q_{\mathrm{b}}. \tag{4.48}$$

4.4.2 Physical Boundary Conditions

In this study, physical boundary conditions are required for the two computational domains of interest: an open numerical wave tank and a numerical wave tank with a monopile. For an open wave field, physical boundary conditions are required at the inlet, outlet, the bottom of the

computational domain and the domain walls. For each physical boundary condition, an associated numerical boundary condition must be constructed and applied for each of the variables to be computed. Correctly applied boundary conditions are vital to simulate fluid flow successfully using CFD. The boundary conditions are not only a geometric description, but also apply to the mesh, discretisation method, computational processing and solver (Versteeg and Malalasekera, 2007).

At the inlet, the physical boundary condition could be a specification of the velocity field value and the pressure field can be assigned a gradient of zero. At the outlet, it is most important to ensure that the overall mass balance for the entire computational domain is satisfied (Ferziger and Peric, 2002). One way of achieving this is to specify that the distribution of the velocity on the outlet boundary is dependent on the inner velocity conditions. However, this specification can lead to instabilities if, due to reflection or non-absorption of the fluid, inflow from the outlet boundary occurs. This problem can be overcome through the use of numerical absorption zones, covered in greater depth in Chapter 5. To avoid this, the pressure distribution (instead of the velocity field) is defined as a fixed-value boundary condition and a zero-gradient boundary condition applied for the velocity.

To represent an open sea, the computational domain walls should influence the flow as little as possible. Symmetric boundary conditions on the walls specify that the flow either side has mirror-symmetry about the centre-plane, approximating open sea conditions. The symmetric boundary condition is applied by setting the component of the gradient normal to the boundary to zero and the parallel components to the boundary are projected onto the boundary face creating the mirror condition.

Other common boundary types for incompressible flow are no-slip and slip conditions. The no-slip boundary condition on a wall means that the velocity close to the walls is equal to the wall velocity, which for a fixed object is equal to zero. The pressure gradient is also assumed to be zero. A slip boundary condition allows fluid flow parallel to the wall and the normal fluid flow is equal to zero. A slip boundary condition implies that the viscous near-wall forces are negligible, or that the mesh element size near the wall is wider than the boundary layer, i.e. when the boundary layer is not important to the calculations.

4.5 Numerical solver for pressure-velocity coupling

Inherent in the Navier-Stokes equations is the dependency of the velocity field on the pressure field and *vice versa*. The OpenFOAM solvers utilise a segregated method for solving for the velocity and pressure fields in sequence by a predictor-corrector iterative approach. Pressure-velocity coupling algorithms are valid for both linear and non-linear systems. For example, the algebraic system of equations in (4.38) that resulted from discretisation of the transport equation can be either linear or non-linear, depending on the partial differential equations from which they are derived.

The iterative methods applied to solve the algebraic system of equations involves providing an initial solution, linearizing the equations about the predicted solution, correcting the solution and repeating until a tolerance level is reached. OpenFOAM uses the PIMPLE algorithm, which blends the Pressure Implicit with Splitting Operator (PISO) approach

introduced by Issa (1985) with the SIMPLE algorithm (Semi-implicit Method for Pressure Linked Equations) (Patanker, 1980) to correct the pressure at each step. The pressure-corrector step also enforces mass conservation for each time step (Ferziger and Peric, 2002).

The pressure equation is derived from the momentum equation, given in the form of (4.38). Rewriting the system of equations, where the term R_P, which includes all transient and source terms excluding the pressure, is now given in terms of the matrix operator $\mathbf{H}(\mathbf{U})$,

$$a_\mathrm{P}\mathbf{u}_\mathrm{P} = \mathbf{H}(\mathbf{U}) - \nabla p, \tag{4.49}$$

where $\mathbf{u}_\mathrm{P}$ is the velocity at centroid point P, and $\mathbf{H}(\mathbf{U})$ is a combination of a transport part and a transient source part,

$$\mathbf{H}(\mathbf{U}) = -\sum a_\mathrm{N}\mathbf{u}_\mathrm{N} + \frac{\mathbf{u}^0}{\Delta t}. \tag{4.50}$$

The value for $\mathbf{u}^0$ in (4.50) is either the velocity result from the previous time step or else the initial guess for the velocity value at the first time step. From the discretised form of the continuity equation in (4.20),

$$\nabla \cdot \mathbf{u} = \sum_\mathrm{f} \mathbf{S} \cdot \mathbf{u}_\mathrm{f} = 0, \tag{4.51}$$

and (4.49) can be applied to denote the centroid velocity value $\mathbf{u}_\mathrm{P}$ in terms of the matrix operator by

$$\mathbf{u}_\mathrm{P} = \frac{1}{a_\mathrm{P}}\mathbf{H}(\mathbf{U}) - \frac{1}{a_\mathrm{P}}\nabla p. \tag{4.52}$$

The face velocities expressed through interpolation of (4.52) across the face are given by

$$\mathbf{u}_f = \left(\frac{1}{a_\mathrm{P}}\mathbf{H}(\mathbf{U})\right)_f - \left(\frac{1}{a_\mathrm{P}}\right)_f (\nabla p)_f. \tag{4.53}$$

Substituting (4.53) into the discretised form of the continuity equation in (4.51) gives the final form of the pressure equation,

$$\nabla \cdot \left(\frac{1}{a_\mathrm{P}}\nabla p\right) = \nabla \cdot \left(\frac{1}{a_\mathrm{P}}\mathbf{H}(\mathbf{U})\right) \tag{4.54}$$

$$= \sum_f \mathbf{S} \cdot \left(\frac{1}{a_\mathrm{P}}\mathbf{H}(\mathbf{U})\right)_f. \tag{4.55}$$

Discretisation of the Laplacian term on the left-hand-side of (4.54) follows the same process outlined for the diffusive terms; the final form of the discretised Navier-Stokes conservation equations for incompressible flow is given by

$$a_\mathrm{P}\mathbf{U}_\mathrm{P} = \mathbf{H}(\mathbf{U}) - \sum_f \mathbf{S}(p)_\mathrm{f}, \tag{4.56}$$

$$\sum_f \mathbf{S} \cdot \left[\left(\frac{1}{a_\mathrm{P}}\right)_f (\nabla p)_f\right] = \sum_f \mathbf{S} \cdot \left(\frac{\mathbf{H}(\mathbf{U})}{a_\mathrm{P}}\right)_f, \tag{4.57}$$

where the flux across the face is

$$F = \mathbf{S} \cdot \mathbf{U}_f = \mathbf{S}\left[\left(\frac{\mathbf{H}(\mathbf{U})}{a_P}\right)_f - \left(\frac{1}{a_P}\right)_f (\nabla p)_f\right]. \tag{4.58}$$

The flux going through the face is guaranteed to be conserved by (4.54). A visual diagram of the PIMPLE algorithm is given in figure 4.6. Note that it reduces to the SIMPLE algorithm without the corrector steps and to PISO for steady-state problems.
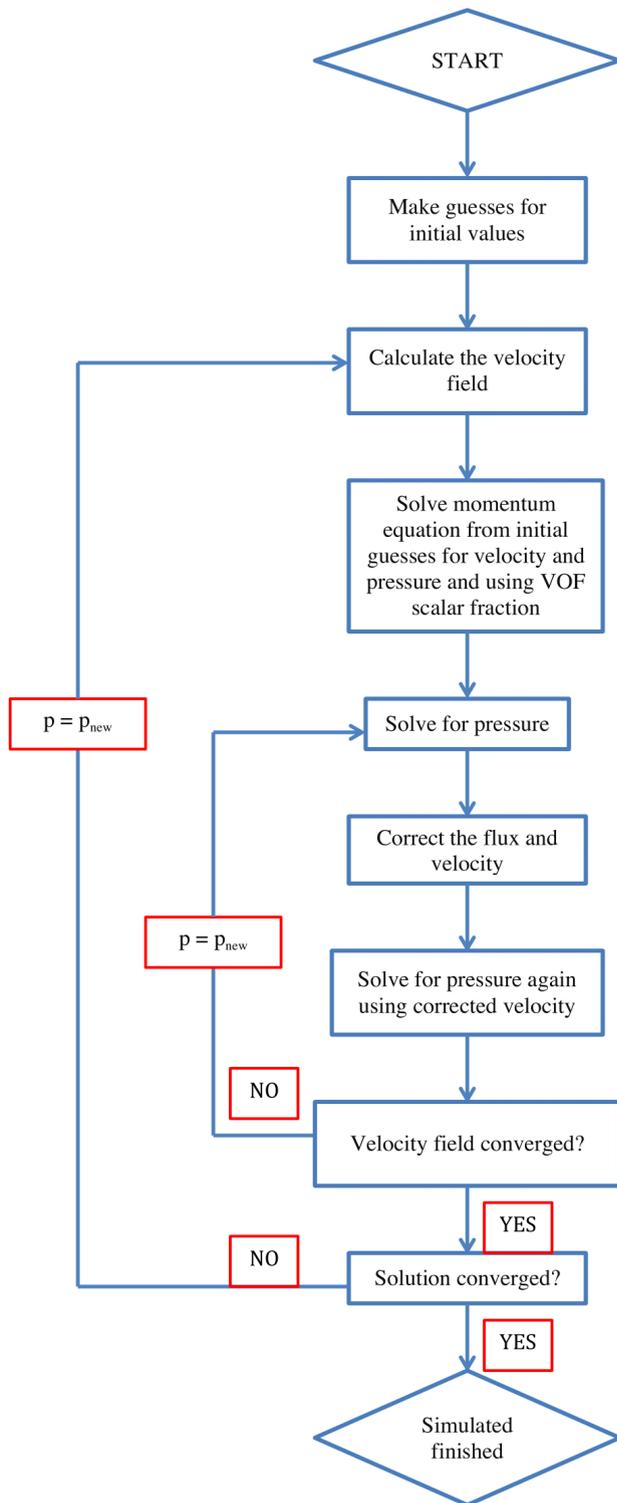
Figure 4.6: Procedure followed by the PIMPLE solver in OpenFOAM.

4.5.1 Other Numerical Solving Algorithms

For the other governing equations, such as VOF in (4.6), the value for α must remain bounded regardless of which numerical scheme is chosen or the mesh structure. To ensure boundedness, an algorithm has been developed in OpenFOAM for solvers that use the VOF method. The solver, the Multidimensional Universal Limiter for Explicit Solution (MULES) method, was created by Henry Weller, one of the main Open-FOAM developers and contributors; the MULES method itself is not explicitly documented. MULES is an iterative semi-implicit predictor-corrector scheme similar in process to PIMPLE that works by computing a corrected flux value between a high and low order scheme solution with a weighting factor. The weighting factor can be determined based on the criterion that the value of the net flux within each cell must neither be greater than the local maximum nor less than the local minimum. In the MULES section of the *interFoam* algorithm, the flux value of α is corrected a specified number of times each time step to ensure the maximum and minimum values remain bounded between 0 and 1. Thus, $\alpha_1 + \alpha_2 = 1$, where α_1 is the volume fraction of water and α_2 is the volume fraction of air. Once this initial value has been attained, it can be used to determine the initial values of other parameters, such as the velocity, before beginning the PIMPLE loop.

4.6 OpenFOAM Case Set-Up

The process for running simulations in OpenFOAM follows the same general procedure regardless of solver chosen. The solver for incompressible, isothermal multi-phase flow that uses the PIMPLE algorithm is called

interFoam. The *interFoam* solver utilises the VOF approach discussed in Section 4.2 to locate the interface between two immiscible fluids and to compute the initial velocity values, dependent on the fluid volume phase fraction, before entering the PIMPLE loop. Figure 4.7 shows the algorithm followed by the *interFoam* solver.

The main directory set-up for each OpenFOAM simulation is laid out in figure 4.8. Contained within the **0** folder in the main directory are the initial and boundary conditions for the velocity, pressure in excess of hydrostatic (called *p_rgh* in OpenFOAM to differentiate from total pressure), and the fluid volume fraction α. Within each field file, the type of boundary condition is specified for that field on each boundary patch or wall and an initial value given where needed, i.e. a fixed-value Dirichlet boundary condition requires an initial value to be defined.

The **constant** folder contains all of the mesh information inside the **polyMesh** subdirectory. Physical properties such as the value of gravitational acceleration ($g = 9.81 \, \text{m/s}^2$), transport properties, such as viscosity and density values for the air and fluid domains, and other environmental properties which act as external source terms are also assigned within the **constant** directory. Turbulent or laminar flow is specified in the *RASProperties* file. Turbulence models are not used in the present thesis and so the flow is set to laminar in the *RASProperties* file for all simulations discussed herein.

Within the **system** folder, the discretisation schemes for each term in the governing equation are specified in the *fvSchemes* file. The solver schemes used for each term (in this case, u, *p_rgh* and α) and PISO parameters (the number of correctors, non-orthogonal correctors and tolerance levels) are set in the *fvSolution* file. The solvers specified here

81
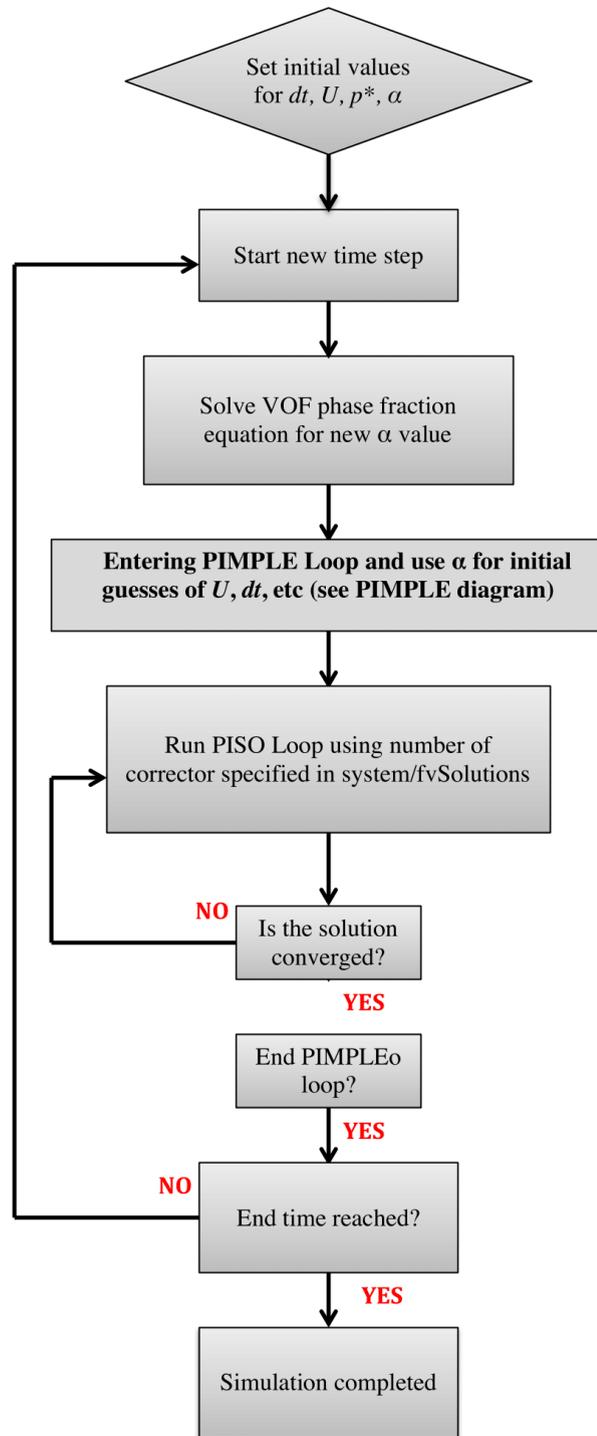
Figure 4.7: The procedure followed by the *interFoam* solver in Open-FOAM.
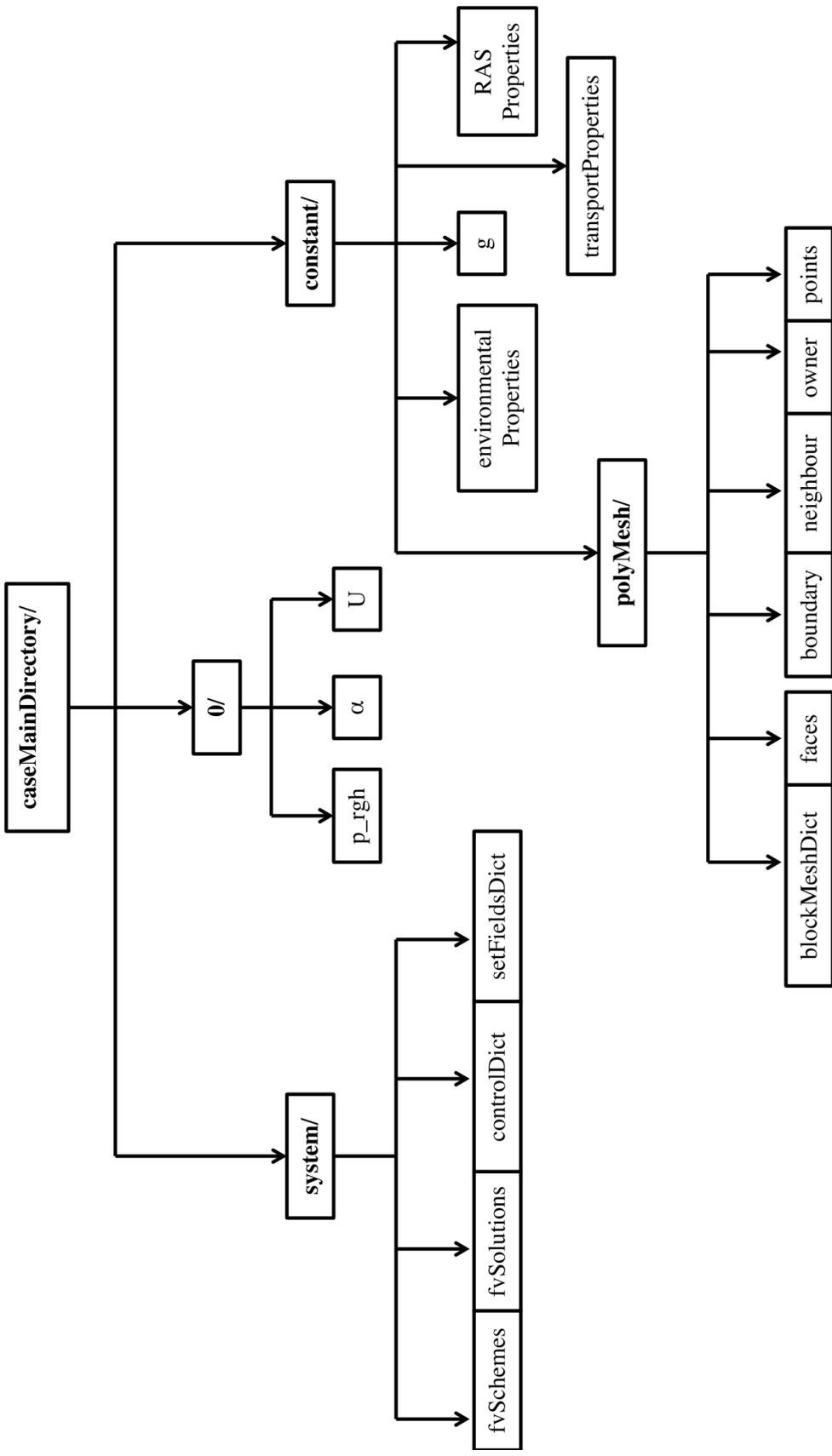
Figure 4.8: Case-set up diagram for *interFoam* simulation. Names in bold indicate folders that contain the information specified in the diagram.

depend on whether the matrices created by the system of equations for the field values are symmetric or asymmetric. The *setFieldsDict* file is used by *interFoam* to set the initial fluid parameters within the computational domain, i.e. the user can specify that the initial α value is equal to 1 for the fluid part of the domain and is equal to 0 for the part of the domain representing the air. The solver name, start and end times, initial time step size and maximum Courant number are set in the *controlDict* file. An automatic time step size adjustment ensures that the Courant criterion is met throughout. The file also contains functions designated to post-process the results as the simulation progresses.

Table 4.1 shows an example of how the discretisation schemes are specified for each term in the governing equation. Not all of the discretisation schemes applied here have been discussed in depth but it can be assumed that the majority of the schemes rely on the second-order Gauss method. For example, the *limitedLinearV 1* scheme used to discretise the continuity equation limits the discretisation used towards an upwind differencing scheme in regions where the gradient changes quickly. The coefficient value of 1 specifies the strongest limiting value and a coefficient value of 0 causes the solution to revert to a Gauss linear scheme. The "V" value in *limitedLinearV* specifies that the scheme is applied to a vector value, such as velocity.

The Gauss *Monotonic Upwind Scheme for Conservation Laws* (MUSCL) scheme is a discretisation algorithm that can be used for scalar fields that are strictly bounded, such as α (van Leer, 1979). For each cell in the domain, the slope-limited value and the reconstructed left and right states of the scalar value are determined, and the values used to compute the fluxes across the cell faces. The specification of "corrected" in the

Laplacian and *snGradSchemes* includes explicit non-orthogonal correction. The *Gauss interfaceCompression* scheme is used to sharpen the interface using VOF in multiphase flows. Note that the set-up illustrated here is valid for the *interFoam* solver only and each solver requires different files to specify fully the problem. For example, a solver for a single phase fluid would not require the α field to be specified.

Table 4.1: Discretisation schemes used in a typical multiphase simulation using VOF

Term name:	Description of term	Discretisation Scheme Used
ddtSchemes	temporal terms	Euler;
gradSchemes	gradient terms	default Gauss linear;
divSchemes	divergence terms	div(rhoPhi,U) Gauss limitedLinearV 1; div(phi,alpha) Gauss MUSCL; div(phirb,alpha) Gauss interfaceCompression;
laplacianSchemes	Laplacian terms	default Gauss linear corrected;
interpolationSchemes	face interpolation	default linear;
snGradSchemes	component of gradient normal to cell face	default corrected;

The user is also responsible for setting consistent units for all values to ensure accurate results. The geometric units are specified inside the **polyMesh** directory in the *blockMeshDict* file. The meshing utility included in OpenFOAM, *blockMesh*, will be further discussed in Chapter 5. Other units are established in the *transportProperties* file, such as units for viscosity and density, and in the *g* and *environmentalProperties* files. It is essential that the user ensures that the units defined for the geometry in the *blockMeshDict* file correspond correctly to the units in the remainder of the physical property files.

Finally, several options for post-processing can be defined in the **sys-**

tem folder such as numerical probes, field sampling specifications, or forces, depending on what data are needed. Files in this folder can be called to run during the simulation as function objects in the *controlDict* file, or else as post-processing steps after the simulation has finished.

As OpenFOAM is an open-source software, the user has many options for manipulating results, solvers, discretisation schemes, boundary conditions, etc. For the novice user, the OpenFOAM release includes tutorials for each of the solvers available; the content of the tutorial directories can be copied and pasted to a new directory and the parameters adjusted to customise the simulation conditions. Moreover, all of the source code is available to view and edit, allowing for the addition of any new schemes, boundary conditions, turbulence models, patch types, etc. Although writing customised code to be used with OpenFOAM must be done carefully so as not to break any links to existing libraries or current codes, the availability of the source code provides templates for the user to adjust existing code.

4.7   High Performance Computing

CFD simulations can require considerable computational resources. Running simulations in parallel across several processors can greatly reduce the computational time, but requires multiple available processors on a personal computer or access to a supercomputer. Access to a high performance computer was made available through the Irish Centre for High-End Computing (ICHEC), enabling simulations to be run across multiple processors (up to 24). Simulations were run on a supercomputer as well as on one or two processors on a personal laptop.

It is straightforward to run OpenFOAM simulations in parallel across multiple distributed processors. An additional tool for running Open-FOAM in parallel was produced through the distribution of a Python wrapper for OpenFOAM called *pyFoam*, which was developed by Bernhard Gschaider [1] and made available to the public as an open-source code. The *pyFoam* command for decomposing the computational domain and running simulations in parallel automatically follows the process outlined below and it will be assumed that the steps given in this section can all be executed using the *pyFoamDecompose.py* code.

4.7.1 Domain Decomposition

The first step in decomposition is to specify the number of subdomains, which can be done in an additional dictionary called *decomposeParDict* located within the *system* folder. There are four decomposition methods available in OpenFOAM: simple, hierarchical, scotch and manual (Weller et al., 1998). The *simple* method is self-explanatory: the computational domain is split into the number of pieces specified by the number of subdomains in the designated direction, i.e. in the *decomposeParDict* file, the user can state that the domain should be split into two directions in the x direction and 1 in the z direction, etc. The *hierarchical* method is the same as simple decomposition except that the user must also specify the order in which the split is done. *Scotch* decomposition is automatically applied when the *pyFoamDecompose.py* code is run. In scotch decomposition, no geometric input specification is required from the user and the decomposition is done automatically by dividing the domain in the best location to minimise the processor boundaries. If

---

[1]https://openfoamwiki.net/index.php/Contrib/PyFoam

87

a specific decomposition scheme is not required, scotch is the simplest method to apply. The final decomposition method available is *manual*, where the user must specify directly what proportion of each cell will go to a particular processor. For all simulations run throughout this work, the scotch method was used to decompose the domain as it offered the greatest ease in application for the required geometry.

4.8   Summary

Algorithms and discretisation methods used in the OpenFOAM CFD software have been presented this chapter. The methods considered can be extended to CFD simulations in general, although the discussion here is focused on the OpenFOAM implementation.

Following the overview of the Navier-Stokes equations and VOF equations that allow for treatment of the interface for multiphase fluids, the Finite Volume method for discretisation was outlined. This describes the continuous equations of fluid flow as a discretised system of algebraic equations to be solved through iterative methods.

The pressure-velocity coupling in the Navier-Stokes equation required the PIMPLE algorithm to be solved first for the pressure, and then pressure and velocity correctors were applied to improve on the initial computed values. An example of a case set-up using the multiphase solver *interFoam* was given with typical discretisation methods emphasized.

Parallelisation for use of OpenFOAM on a high-performance computer was also briefly discussed. The procedure and algorithms described in this chapter provide the basis for the flow simulations discussed in later chapters.

Chapter 5

Validation of Numerical Model

Chapter Summary

In this chapter, benchmark simulations are presented to validate the OpenFOAM model for problems to which analytical solutions exist. The first validation test considers the interaction of a steady current with a smooth, surface-piercing, bottom-fixed cylinder representing the wind turbine monopile support structure. The second and third sets of tests consider linear waves in an open numerical wave tank (NWT) and linear waves past a surface-piercing cylinder. Analytical solutions for force coefficients in a steady current and wave particle kinematics, wave pressure, and in-line wave forces in linear regular waves are compared to the numerical predictions. Meshing with the OpenFOAM utility *blockmesh* and the open-source meshing software *Gmsh* is also briefly examined. Lastly, effective wave absorption is explored through the use of relaxation zones where the focus is specifically in reduction of relaxation zone length, thereby decreasing computational overhead.

5.1 Introduction

The evaluation of wave forces on a cylinder is an integral part of offshore engineering, a typical application being the design of marine structures to withstand wave damage (Sarpkaya, 2010). The present study considers disturbances to the passing wave field caused by the presence of the monopile support column, as well as the loads on the column. An alteration of the undisturbed flow field has a subsequent effect on any floating object in contact with the structure, such as a CTV abutted against a monopile support column. The application of the methods for resolving the forces incident on the structure to problems, where known experimental or analytical solutions exist, provides a reliable method for verifying and validating the numerical model.

The analytical solutions were found through application of the equations for wave motion and the wave force loading methods presented in Chapters 2 and 3. The numerical methods outlined in Chapter 4 were applied to simulate the wave numerically. Prior to solving the numerical problem using CFD, a geometrical mesh was constructed, following the meshing procedure described in Section 5.2. In Section 5.3, results are presented from simulation of idealised steady currents past a cylinder with differing Re values, where $Re = U_\infty D/\nu$ and U_∞ is the undisturbed flow, D is the cylinder diameter, and ν is the coefficient of fluid kinematic viscosity. Reynold's number values of $Re = 40$, 300, 3900, and 1×10^5 were utilised. At very low Re values, the flow field should remain symmetric with no visible vortex shedding (Sumer and Fredsøe, 2006) and the flow can be considered as a steady state. The flow remains steady and laminar for $Re = 40$, and a pair of symmetric rotating vortices may

form on the cylinder and remain attached (Zdravkovich, 1997) (although Norberg (1994) did not observe vortices forming for $Re < 47.4$). At these very low Re values, the fluid flow should behave almost as an ideal flow, where the cylinder has little or no effect on the flow field.

As Re increases to 300, the vortices that form begin to detach periodically from the cylinder as the pressure gradient within the wake decreases. This vortex shedding creates a wake pattern called a *Von Kármán Vortex Street* (Sarpkaya and Isaacson, 1981). At $Re = 3900$, an unsteady vortex pattern forms in the wake and the shed vortices travel down the wake and are transported away from the cylinder. Experimental values for the drag coefficient at these Re values have been well documented (Sarpkaya and Isaacson, 1981, Zdravkovich, 1997). At $Re = 1 \times 10^5$, vortices form and should detach, but the wake narrows due to a decrease in viscous behaviour (Sumer and Fredsøe, 2006). This decrease in the effect of viscosity is notable in the "drag crisis" portion of the chart illustrated in figure 3.3.

In Chapter 3, the total wave force on the cylinder over its submerged length l in an idealised flow was determined through integration of the surface pressure (see eqns. (3.4) and (3.5)). From the values of the drag and lift force, F_d and F_l respectively, the drag and lift coefficients, C_d and C_l, can be calculated directly from the force values by

$$C_d = \frac{2F_d}{\rho |u_\infty^2| D} \qquad (5.1)$$

and

$$C_l = \frac{2F_l}{\rho |u_\infty^2| D}, \qquad (5.2)$$

where ρ is the fluid density, u_∞ is the oncoming velocity of the undisturbed flow and D is the cylinder diameter.

Previously, C_d was calculated using (3.7); this method is useful for high values of Re where experimental values do not exist. However, empirical values of the force coefficients at low Re number values have been well documented (Sarpkaya and Isaacson, 1981, Sumer and Fredsøe, 2006, Zdravkovich, 1997).

Linear waves in an open NWT are then simulated for several different flow parameters and the results are presented in Section 5.4. Effective wave absorption using relaxation zones is explored, where the focus is on absorbing the wave completely whilst reducing the total length of the computational domain. The wave parameters used for the NWT are again applied to simulate free surface waves interacting with a bottom-fixed surface-piercing smooth cylinder. The waves simulated here (see Section 5.5) should display characteristics depending on the diameter-to-wavelength ratio. Analytical solutions exist for linear diffraction from a large diameter cylinder and the Morison equation provides a good approximation for the forces on a small-diameter cylinder (see Section 3.2). Several wave parameters are tested, first for cases corresponding to experimental studies, in order to explore relaxation zone length, and then for cases with a range of linear wave parameters similar to those found at Teesside Offshore Wind Farm. Conclusions about the success of the OpenFOAM model are presented in Section 5.6.

Numerical simulations are conducted on the super-computer FIONN, operated by the Irish Centre for High End Computing (ICHEC). Each simulation employed several processors of one node of the "thin" component of FIONN, comprising 2 x 12 core 2.4 GHz Intel Ivy Bridge proces-

sors, 64 GiB of RAM and an FDR InfiniBand network adaptor (ICHEC, 2018). Numerical validation cases presented in this chapter were run in parallel on eight processors.

Comparison between the analytical solutions and numerical predictions of forces on a cylinder in regular linear waves is used to validate the numerical model and provides an important foundation for determining the same parameters for a cylinder in irregular waves, which will be explored in Chapter 6.

5.2   Computational Domain and Meshing

In OpenFOAM, the mesh is called a *polyMesh*. Arbitrarily aligned continuous non-overlapping polyhedral cells offer the user considerable freedom in meshing complex geometries (Weller et al., 1998). OpenFOAM has a built-in meshing utility called *blockMesh* that can be used to create simple geometries used by the finite volume method (see Section 4.3). The mesh is constructed where the boundary of the computational domain coincides with the faces of the control volumes on the boundary. Point locations are first defined in the dictionary *blockMeshDict* and the mesh element type selected (hex-shaped elements are used throughout this work). Each block is constructed by connecting the vertices in the correct order (see figure 5.1 for *blockMesh* ordering convention).
Each control volume is defined by a physical boundary type, i.e. patch for a boundary with in- or out-flow, walls for boundaries through which no fluid flows, symmetry for symmetrical flow patterns, or empty for 1D or 2D simulations, and the mesh is constructed using the *blockMesh* utility algorithm included in OpenFOAM.
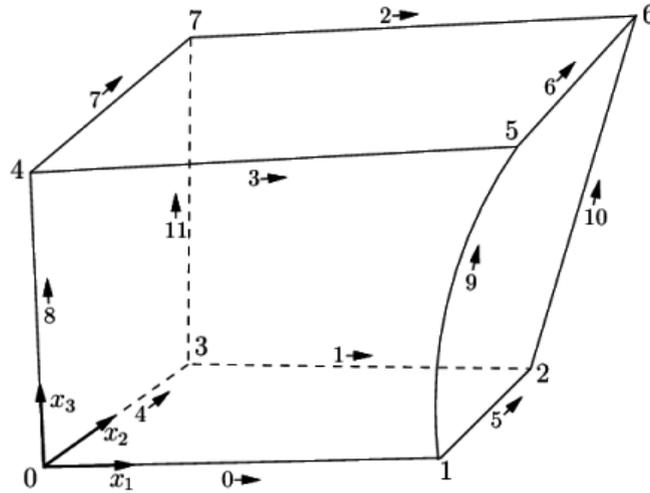
Figure 5.1: Vertex and control volume face numbering convention used in *blockMesh* with the direction of ordering indicated by the arrows. - Adapted from Greenshields (2015)

Whilst *blockMesh* is capable of generating simple geometries, it can become difficult and time consuming to control the quality of the mesh, such as reducing non-orthogonality and maintaining suitable aspect ratios, and creating meshes for more complex geometries quickly increases the effort in using *blockMesh*. For more complex geometries and better control over the mesh quality, it is possible to convert the mesh from another software directly into a format recognised by OpenFOAM.

Initially, *blockMesh* was used to generate the mesh for applications described in this thesis, where variables defined at the start of the *blockMeshDict* file allowed easy mesh generation and where the dimensions and cell size were dependent on parameters such as the wavelength or cylinder diameter. However, to gain better control over the mesh quality, the open-source meshing tool *Gmsh* was used. The results presented here use meshes created with *Gmsh*, which likewise creates meshes of the geometry, on which the finite volume method is applied. *Gmsh* also includes

a user-friendly GUI to ease mesh construction (Geuzaine and Remacle, 2009). A screen shot of the mesh created in *Gmsh* using a quadrilateral transition zone around the cylinder is shown in figure 5.2, where the magnified area demonstrates cell grading applied closer to the cylinder and within the wake.
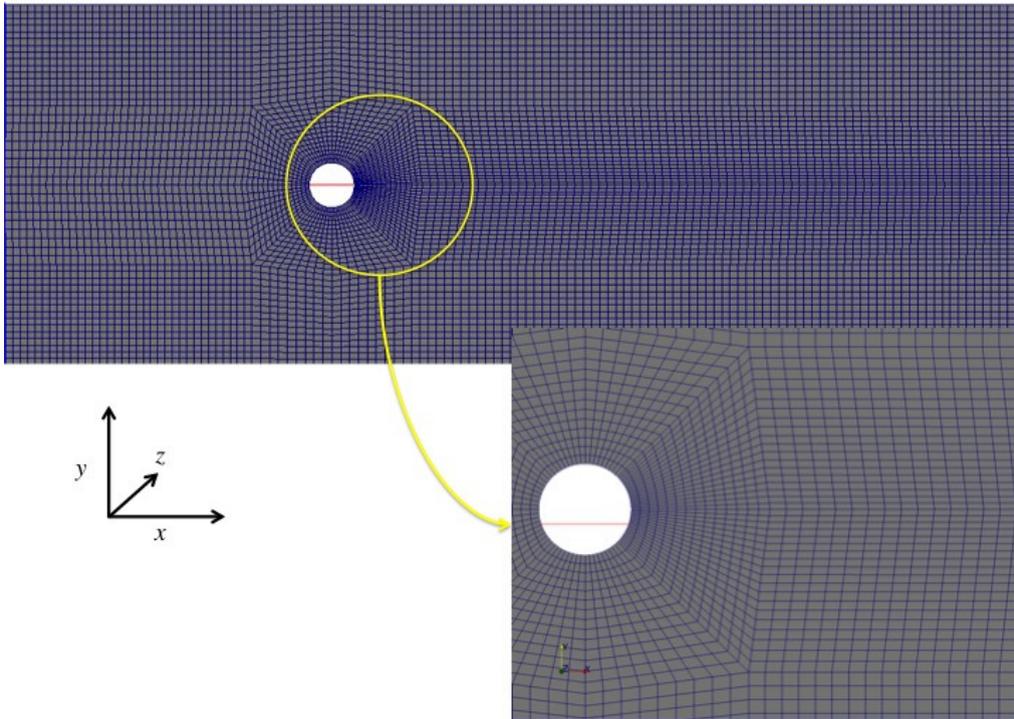
Figure 5.2: Mesh with monopile present, transition zone magnified

OpenFOAM includes a renumbering-mesh utility, *renumberMesh*, which improves the node numbering for meshes created with different software to optimise the mesh for OpenFOAM. The bandwidth is greatly increased when the node numbering is not optimized for the applied solver method. Renumbering the mesh ensures that the node numbering will be in the most efficient order and is employed when *Gmsh* is used.

5.3 Steady current past a cylinder

A steady unidirectional current past a cylinder is first simulated. For a cylinder in a steady current, the in-line force on the cylinder is quantified in order to determine drag and inertia coefficients. Four cases are tested, for $Re = 40$, 250, 3900 and 1×10^5. The computational domain for all simulations is 6 m long and 2 m wide with a depth of 0.3 m and a cylinder diameter $D = 0.2$ m, which gives a blockage ratio of 10%. An additional 0.3 m in the vertical direction represents the atmosphere. Figure 5.3 illustrates the patches on the boundaries in the mesh, the locations at which the boundary conditions are applied. At each value of Re, the drag and lift coefficients are determined.
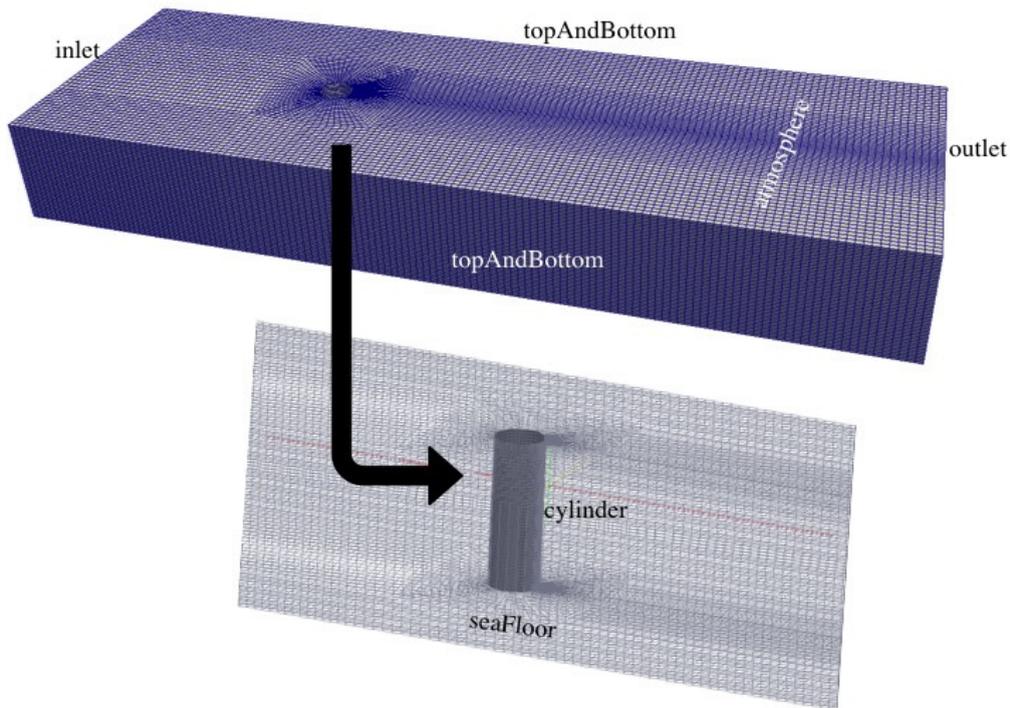
Figure 5.3: Patch names for simulation with a monopile. Top image displays entire computational domain and bottom image shows a close-up of the cylinder.

The mesh element length in the flow direction is $\Delta x = 0.039$ m in the

region away from the cylinder and $\Delta x = 0.014$ m near the cylinder walls. In the vertical direction, $\Delta z = 0.014$ m. Each simulation is run for 50 s with an initial time step $dt = 0.01$ s, and an adjustable time step is used thereafter to satisfy automatically the Courant criterion, where $Co \leq 0.5$. The *interFoam* solver is implemented with the boundary conditions given in Table 5.1.

Table 5.1: Boundary conditions used for constant current past a cylinder

	velocity	**pressure**	**VOF fraction**
inletAir	fixedValue value uniform (0 0 0)	zeroGradient	fixedValue value uniform 0
inletWater	fixedValue value uniform (0.5 0 0)	zeroGradient	fixedValue value uniform 1
outlet	zeroGradient	zeroGradient	zeroGradient
seaFloor	zeroGradient	zeroGradient	zeroGradient
atmosphere	pressureInletOutletVelocity	totalPressure	inletOutlet
frontAndBack	symmetry	symmetry	symmetry
cylinder	zeroGradient	zeroGradient	zeroGradient

The *pressureInletOutletVelocity* velocity boundary condition at the atmosphere is applicable when the pressure on the boundary is known - the pressure difference at the interface is equal to zero. This boundary condition defines a zero-gradient condition for flow moving outwards, where the direction is defined by the flux, and the inflow velocity is acquired from the patch-face normal component of the internal cell value for the velocity.

Similarly for the VOF fraction, named *alpha.water* in OpenFOAM, the boundary condition *inletOutlet* specifies zero-gradient for the flow moving outwards and a specified value for flow moving inwards with respect to the boundary; the inlet flow is equal to zero for all cases throughout this work. The *totalPressure* boundary condition specifies

that the pressure at the boundary is

$$
p =
\begin{cases}
p_0, & \text{for outflow} \\
p_0 - \frac{1}{2}|\mathbf{u}|^2, & \text{for inflow (incompressible).}
\end{cases}
$$

Using the *checkMesh* utility supplied with OpenFOAM, the mesh quality is checked. The maximum aspect ratio for all meshes in this section is 3.94. The images in figure 5.4 are screen shots at $t = 15.5$ s for $Re = 40$ and $Re = 300$.

(a)   (b)
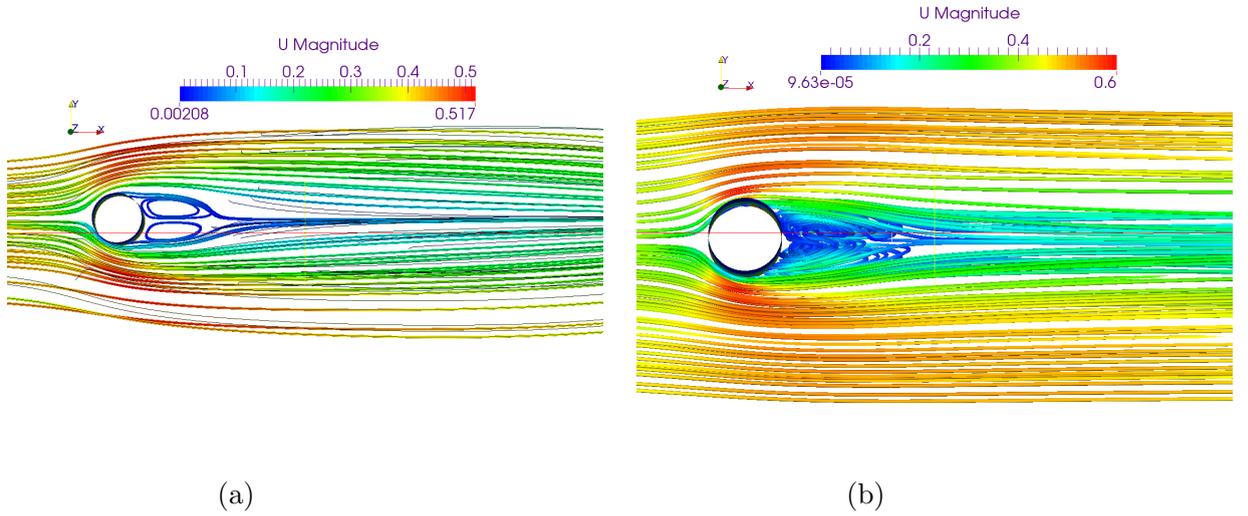
Figure 5.4: Streamlines at $t = 15.5$ s for (a) $Re = 40$ and (b) $Re = 300$.

For $Re = 40$, figure 5.4a, two symmetrical vortices have formed on the cylinder but do not detach from the cylinder wall. At $Re = 300$, flow rotation occurs, evidenced by the two vortices that have formed on the cylinder wall, shown in figure 5.4b. The vortices have not yet begun to detach from the cylinder. Figure 5.5 presents screen shots from $Re = 3900$, where figure 5.5a is taken at $t_1 = 5$ s and figure 5.5b is at $t_2 = 50$ s. By t_2, vortices that could be seen beginning to form at t_1 have detached from the cylinder, creating the unsteady vortex wake pattern that can be seen downstream of the cylinder.

(a)   (b)
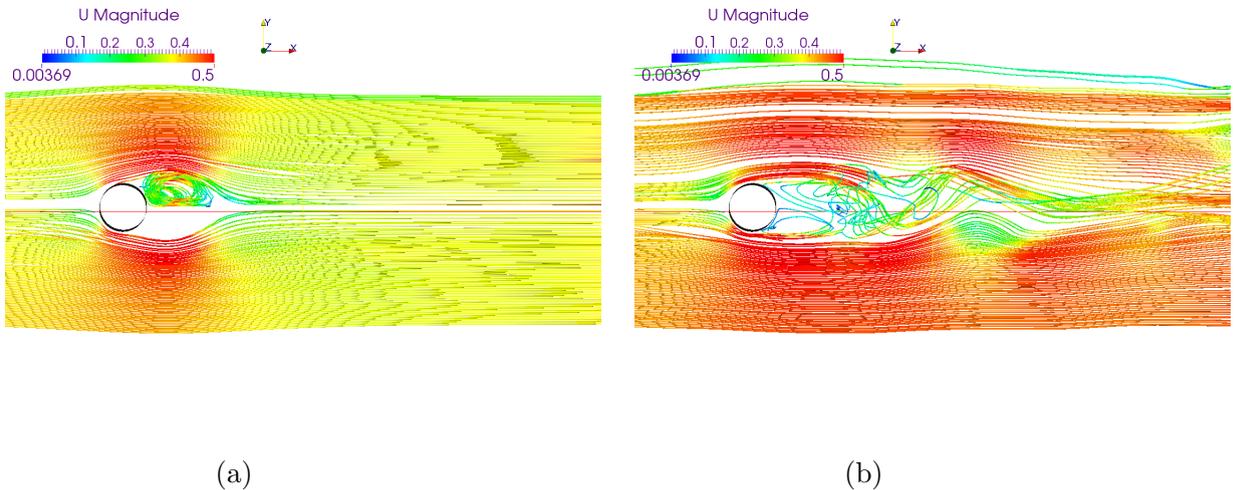
Figure 5.5: Streamlines for $Re = 3900$ at (a) $t = 5$ s and (b) $t = 50$ s.

Table 5.2 lists the values found for C_d where (5.1) is applied to determine the coefficients from the instantaneous drag force. Values for the drag coefficient vary widely, and information is taken from several sources to provide empirical values for the drag coefficient.

Table 5.2: Drag and lift coefficient values for each simulation, specified by the Reynolds number Re

	40	300	3900	1×10^5
Numerical results (this study)	1.9	1.82	1.26	1.00
Braza et al. (1986)	1.6	–	–	–
Wieselsberger (1922)	–	1.3	–	–
Beaudan and Moin (1994)	–	–	1.74	–
Rahman et al. (2007)	–	–	0.997	–
Schlichting (1960)	–	–	–	0.7

As Re increases, the development of the vortices and separation of the vortices from the cylinder, forming a vortex shedding pattern within the wake are apparent in the visualisations. The changing flow regime, which can be expected at these values and described by Zdravkovich

99

(1997) are presented in figures 5.4 and 5.5, The fluid remains within the laminar regime and achieves a steady-state solution, which agrees with accepted results at $Re = 40$ (Apelt, 1958). The wake becomes unsteady and the length of the vortices increase. The flow appears to be periodic with the developing vortices having the greatest influence on the flow structure. This transition to an unsteady wake agrees with experimental and numerical results Rajani et al. (2009).

The unsteady vortex shedding pattern that develops at $Re = 3900$ and visible in figure 5.5 shows a subcritical flow regime, seen in category e) in figure 3.1. The development of a vortex street pattern results from the increasing influence of viscosity within the boundary layer on the cylinder wall as Re increases.

OpenFOAM demonstrates capability in capturing viscous effects within the numerical model of unidirectional flow. The vortex development and separation pattern that are apparent in the numerical model are in good agreement with previous results and the resulting drag coefficient values are within the acceptable range.

5.4   Linear Waves in an open wave tank

The OpenFOAM version used throughout this work, v. 2.4.0, does not include wave propagation. However, Jacobsen et al. (2011) developed an extension to the multiphase solver, *interFoam*, for wave generation as part of their Waves2Foam package. For incompressible flow, the solver *waveFoam* operates similarly to the *interFoam* solver. The *waveFoam* solver generates free surface flows using the RANS formulation (see eqn. (4.5)) coupled with the VOF method discussed in Section 4.2.1. The

assumption of linear waves remains valid throughout and the wave steepness $H/\lambda < 1/7$ for all validation simulations to ensure small-amplitude waves required by linear wave theory.

5.4.1 Wave Absorption

For all wave tank simulations, wave absorption is achieved using the relaxation zone utility included in the Waves2Foam release, which acts as a sponge layer to eliminate wave reflection at the outlet wall. When simulating flow around a cylinder, an inlet relaxation zone can also be used to absorb waves reflecting from the cylinder to avoid interference with the inlet flow.

Prior to solving the RANS momentum equation, the velocities and fluid volume fraction α are multiplied by a weighting function within the relaxation zone. A relaxation zone is defined as inlet if the value is 0 at the start of the domain and 1 at the end and an outlet if the value is equal to 1 at the start of the relaxation zone and 0 at the end. The relaxation function is

$$\alpha_R\left(\chi_R\right) = 1 - \frac{exp\left(\chi^\zeta\right) - 1}{exp(1) - 1},\tag{5.3}$$

where the value of χ represents the location within the relaxation zone and is 0 at the start of the relaxation zone and 1 at the end; the default value for ζ is 3.5 (see e.g. Mayer et al. (1998)). Adjustment of the value for ζ changes the behaviour of the relaxation zone and can permit a shorter computational domain through more rapid absorption of the wave. Inside the relaxation zone, α_R is applied through

$$q = \alpha_R q_{computed} + (1 - \alpha_R) q_{target}, \qquad (5.4)$$

where q is either the velocity $\mathbf{u}$, where $\mathbf{u}_{target} = \mathbf{0}$, or the fluid volume fraction α, where α_{target} is dependent on the location of the still water level.

5.4.2 Mesh Convergence

A mesh convergence analysis was first run for an experimental case; table 5.3 lists the mesh parameters and running times for each mesh. The parameter values used for the mesh convergence tests were chosen to replicate cases investigated experimentally by Chapalain et al. (1992) and numerically by Jacobsen et al. (2011). The computational domain possessed length $L_x = 39$ m and width $L_y = 10$ m, with a wave period of $T = 3.5$ s (corresponding to wave length $\lambda = 6.8$ m) and the wave height was prescribed as $H = 0.084$ m. The number of elements and element size were varied by adjusting the number of cells per wavelength in the horizontal direction (Δx) and wave height in the vertical direction (Δz). No relaxation zones were used and the run time for each simulation was minimized so that reflected waves would not interfere with the incident waves at the gauge of interest. All simulations were undertaken in parallel on a supercomputer across 24 processors with 64 GB of RAM. Figure 5.6 depicts the time series for velocity in the x-direction (U_x) at $(x, y) = (15, 0)$.

It can be seen in figure 5.6 that mesh 3 corresponded well to the analytical solution and mesh 4 did not improve the results significantly, so the parameters for mesh 3 (75 cells per wave length and 8 per wave

Table 5.3: Mesh Details

Mesh Number	Max. cells per λ (Δx)	Max. cells per H (Δz)	Total Elements	Total Runtime
1	30	3	377,304	11m 58s
2	50	5	691,886	20m 59s
3	75	8	1,274,130	57m 33s
4	100	8	2,437,596	145m 30s
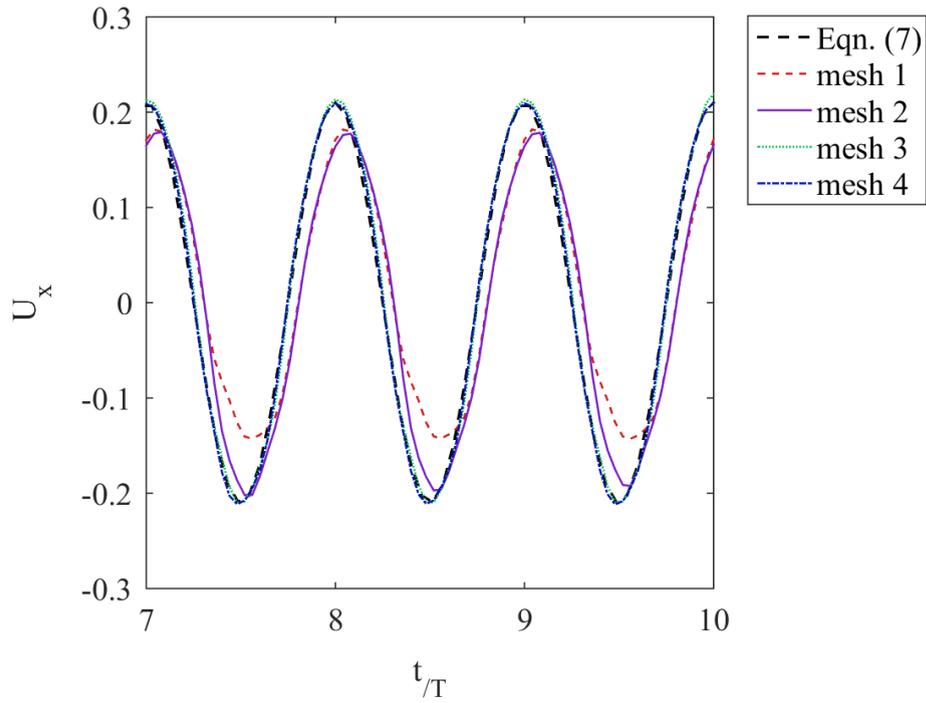
Figure 5.6: Mesh convergence test results: horizontal velocity time series at elevation $z = 0.4$ m under regular waves, at $T = 3.5$ s and $H = 0.084$ m, where details of mesh 1, mesh 2, mesh 3 and mesh 4 are given in Table 5.3.

height) were deemed sufficient. Boundary conditions for each field were applied in the 0 time directory used by OpenFOAM and are detailed in table 5.4.

Table 5.4: Boundary Conditions

Boundary	*alpha.water*	U	p_{rgh}
topAndBottom	symmetry	symmetry	symmetry
inlet	waveAlpha	waveVelocity	zeroGradient
outlet	zeroGradient	fixedValue	zeroGradient
seaFloor	slip	slip	slip
atmosphere	inletOutlet	pressureInletOutletVelocity	totalPressure

5.4.3 Relaxation Zone Length Modification

An investigation was undertaken into the influence that varying the ζ-value in (5.3) has on the wave absorption, in order to reduce the length of the outlet relaxation zone. Numerical wave gauges, a utility included in the Waves2Foam package for determining free surface location, extending from the bottom of the domain to the top were spread out evenly on the $y = 0$ plane and vertically interpolated to calculate the free surface location. Figure 5.7 depicts two possible computational domains; the upper image comprises a relaxation zone of length 2λ and the lower image a relaxation zone of length λ. When waves generated in an open channel are produced, it is assumed that the domain length is sufficiently long, relative to the wavelength, and the number of wave periods simulated is small enough that outgoing waves are fully absorbed and do not reflect, removing the need for an inlet relaxation zone.

In the validation cases considered for the *relaxationZone* utility, Jacobsen et al. (2011), a relaxation zone length of approximately 2λ was used. Chen et al. (2014) found that a relaxation zone length of 1.5λ
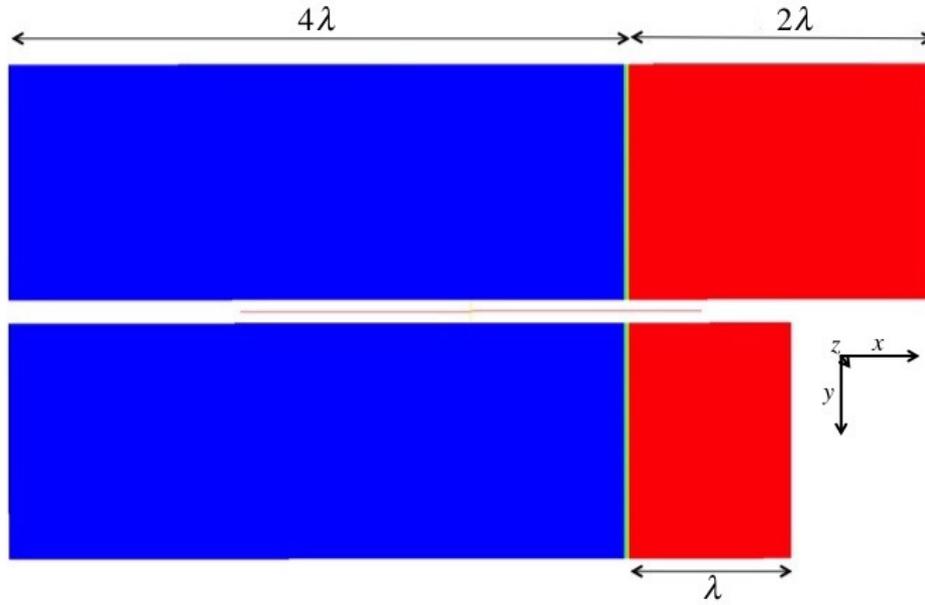
Figure 5.7: Computational domain with differing relaxation zone lengths.

was sufficient. It must be noted that an additional 2λ or 1.5λ increases the computational cost and CPU time considerably. Reduction of the computational domain whilst still achieving full wave absorption is thus explored here. Modification of the value for ζ changes the behaviour of the relaxation zone and can permit a shorter computational domain through more rapid absorption of the wave. Figure 5.8 gives a presentation of the behaviour of the wave within the relaxation zone for different values of ζ in (5.3).

The free surface should remain at a constant level throughout the domain outside the relaxation zones, but it can be seen clearly in figure 5.9 that when no relaxation zone is used, wave reflection occurs, which is evident in the increase in surface elevation. Adjusting the ζ-value and then the length of the outlet relaxation zone showed no effect on the incident waves, thereby implying full wave absorption was achieved.

105
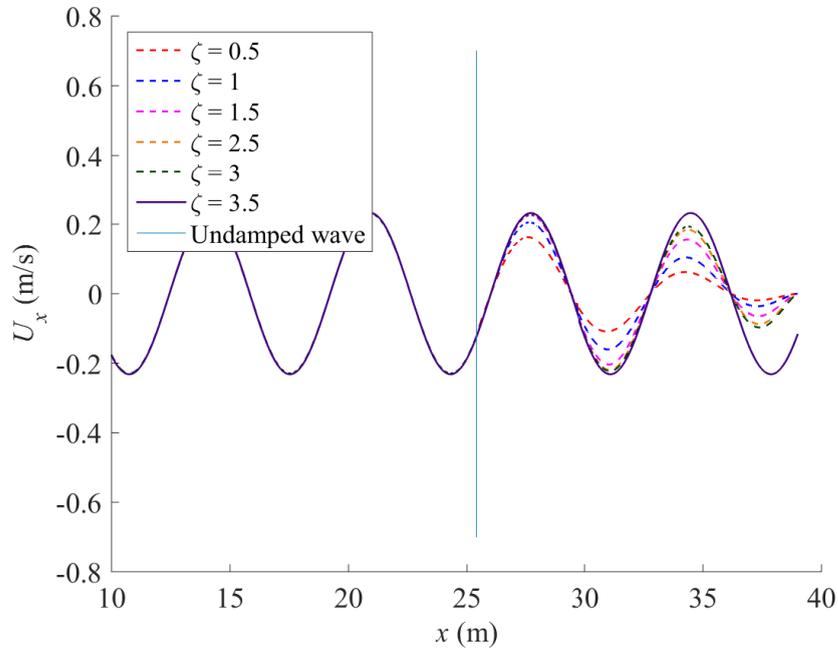
Figure 5.8: Water particle velocity profiles obtained for different ζ-values in (5.3) indicating their effect on the wave absorption within the damping zone
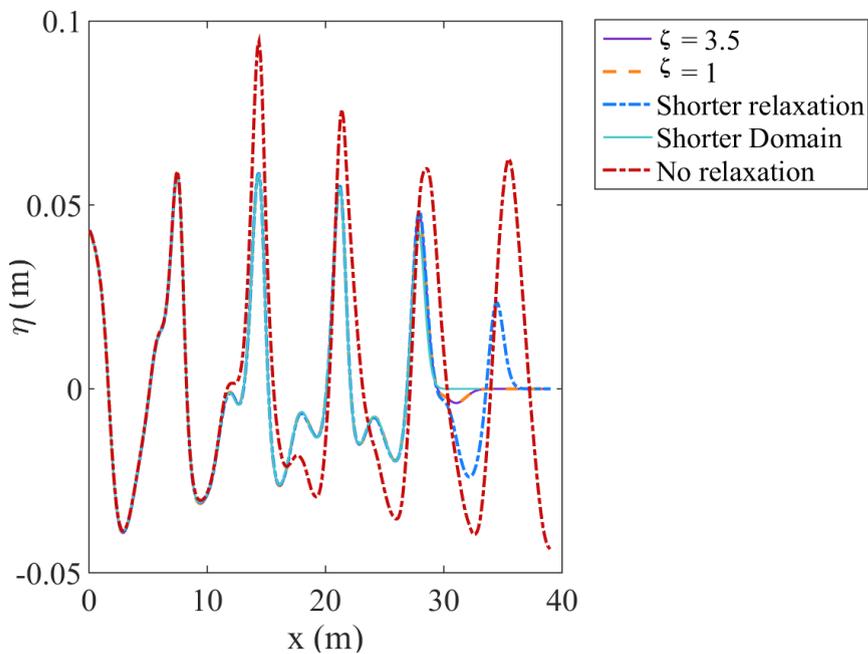
Figure 5.9: Surface elevation profiles along domain length at $t^* = 5$ for different wave absorption conditions and varying values for ζ in equation (5.3).

5.4.4 Linear waves in a numerical wave tank

Linear waves in a NWT are simulated where the wave parameters reflect values comparable to those found at Teesside Offshore Wind Farm. The wave periods tested are $T = 4$, 6, 8 and 10 s, corresponding to wave lengths $\lambda = 25$, 53, 82 and 109 m respectively, for depth $h = 15$ m. The cylinder diameter $D = 5$ m, and the wave height $H = 1.0$ m throughout. Simulations were run for 40 wave periods. The domain length for each simulation was set at 4λ in the wave propagation (x) direction and λ in the transverse (y) direction. The vertical domain z had a depth of 15 m and extended to 10 m above the free surface. For all simulations, 8 cells in the vertical direction were used, giving $\Delta z = 0.125$ m. Table 5.5 lists the wave period, corresponding wave length, mesh element size in the Δx direction and maximum aspect ratio (AR), calculated with (4.28). Figures 5.10-5.13 present results for the simulations of a linear wave train in a NWT with no cylinder present.

Table 5.5: Mesh details for each linear wave in a NWT case

T (s)	λ (m)	Δx (m)	Maximum A.R.
4	25	0.33	3.10
6	53	0.71	4.73
8	82	1.09	7.31
10	109	1.45	9.72

A comparison is made between the numerical and analytical values for the undisturbed wave pressure, horizontal and vertical velocity components, and surface elevation. Numerical wave gauges were used to locate the free surface through interpolation of α in the vertical direction. The velocity components and wave pressure are extracted from the numerical

probe utility included in OpenFOAM. Both the wave gauges and numerical probes are placed 20 m from the inlet of the computational domain, and the analytical properties calculated at the same location.

Comparisons between the numerical prediction of a parameters within a monochromatic linear wave in a NWT versus the analytical solutions, shown in figures 5.10-5.13, show that the numerical prediction accurately simulates the waves for varying wave lengths. Excellent agreement between the analytical solution and numerical prediction is seen in across all four wave periods for the wave pressure and vertical velocity components, i.e. figures 5.10b-5.13b and figures 5.10d-5.13d. A small upwards shift is seen in both the horizontal velocity component, U_x, and the surface elevation, *eta* across each simulation. This is likely due to a small increase in the location of the still water surface, likely related to a lack of mesh refinement for the simulations of the shorter wave periods. Despite the increase seen in some parameters within the simulated wave, the stability of the remainder of the parameters gave satisfactory verification that the correct wave was produced.

5.5 Wave-structure interaction: waves past a surface-piercing cylinder

Simulations were also carried out for linear waves past a monopile. The simulated surface elevation was compared to the diffracted surface elevation from (3.16), as well as the undisturbed free surface elevation, $\eta = a\cos(kx - \omega t)$. For small-diameter cylinders, where, for $D/L < 0.2$, the undisturbed surface elevation should be comparable to the predictions from the analytical diffracted model and the numerical model. As
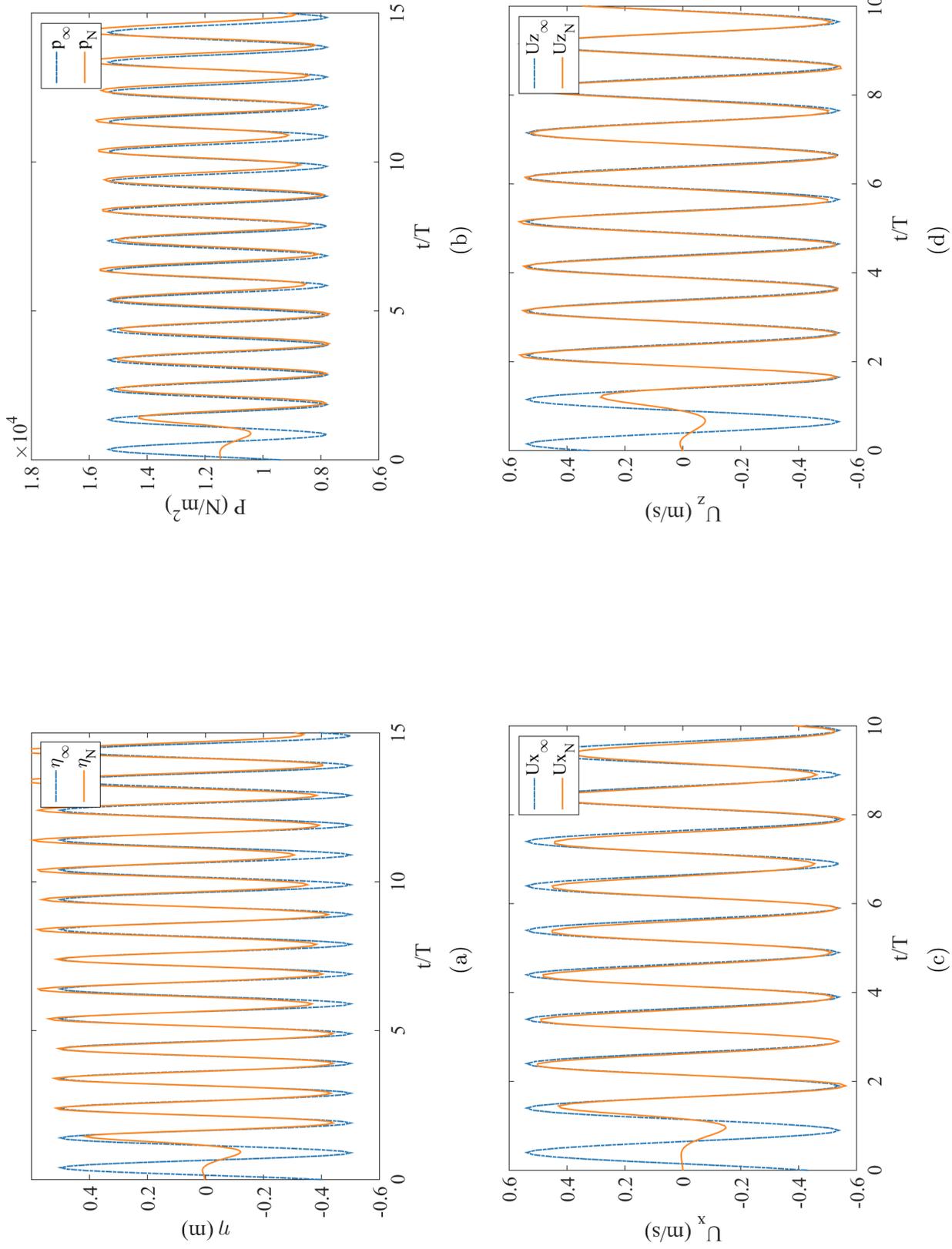
Figure 5.10: Comparison between numerical predictions and analytical solutions of linear wave parameters for waves with period $T = 4\,\mathrm{s}$. Figures illustrate time series predictions for (a) surface elevation, (b) pressure time series, (c) horizontal velocity component, (d) vertical velocity component. For each parameter in these figures, the subscript ∞ denotes the analytical linear wave solution and the subscript N represents the numerical simulation.

Figure 5.11: Comparison between numerical predictions and analytical solutions of linear wave parameters for waves with period $T = 6$ s. Figures illustrate time series predictions for (a) surface elevation, (b) pressure time series, (c) horizontal velocity component, (d) vertical velocity component. For each parameter in these figures, the subscript ∞ denotes the analytical linear wave solution and the subscript N represents the numerical simulation.

Figure 5.12: Comparison between numerical predictions and analytical solutions of linear wave parameters for waves with period $T = 8$ s. Figures illustrate time series predictions for (a) surface elevation, (b) pressure time series, (c) horizontal velocity component, (d) vertical velocity component. For each parameter in these figures, the subscript ∞ denotes the analytical linear wave solution and the subscript N represents the numerical simulation.

Figure 5.13: Comparison between numerical predictions and analytical solutions of linear wave parameters for waves with period $T = 10$ s. Figures illustrate time series predictions for (a) surface elevation, (b) pressure time series, (c) horizontal velocity component, (d) vertical velocity component. For each parameter in these figures, the subscript ∞ denotes the analytical linear wave solution and the subscript N represents the numerical simulation.

the wavelength decreases, diffraction effects increase. Table 5.6 lists the mesh details for the simulations involving the monopile, inclusive of the diameter-to-wavelength ratio. The value for Δx given here refers to the minimum cell length in the region around the cylinder.

Table 5.6: Mesh details for each linear waves past a cylinder

T (s)	$\frac{D}{L}$ (m)	Min Δx (m)	Max. A.R.
4	0.2	0.175	10.1
6	0.1	0.377	8.73
8	0.06	0.404	9.54
10	0.04	0.565	9.54

The total forces incident on the monopile are calculated from the Morison Equation (3.6), integration of the numerical surface pressure and from the diffraction formulation given in (3.19). A slip boundary condition is applied on the cylinder and all other boundary conditions remain as listed in Table 5.1.

Numerical wave gauges are again applied near the inlet and at 16 locations around the cylinder at a distance of $\pi/8$ from each other and $0.1D$ away from the cylinder wall. Wave gauges are used to capture both the inlet surface elevation and the diffracted surface elevation in several locations. The free surface elevation and wave forces are quantified and a time series for the four different wave periods given in figures 5.14-5.17. The surface elevation is measured on the cylinder at $\theta = 0$, where θ is measured positive anti-clockwise from the $y = 0$ axis; i.e. measurements are taken at the rear-stagnation point of the cylinder. The Re and KC values for the analytical solution (subscript ∞) and the numerical solution (subscript S) are listed in Table 5.7. For waves of longer wave-

113

length, the forces calculated using the Morison equation should equate to the diffraction force calculation.

Table 5.7: Re and KC values for linear waves past a monopile

T (s)	KC_∞	KC_S	Re_∞	Re_S
4	0.48	0.44	3.00×10^6	2.75×10^6
6	0.57	0.50	2.37×10^6	2.08×10^6
8	0.65	0.54	2.02×10^6	1.67×10^6
10	0.72	0.62	1.03×10^6	1.54×10^6

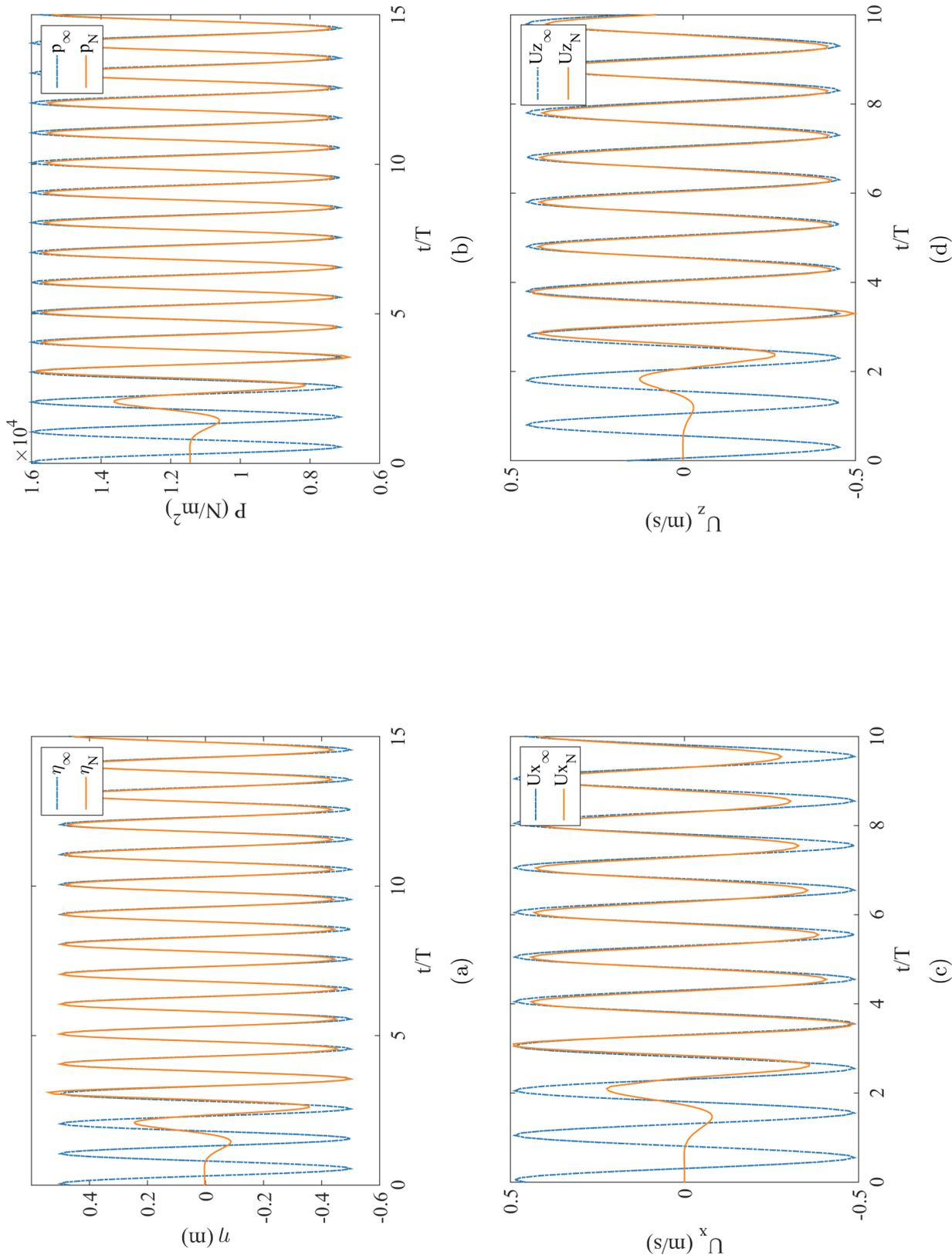(a)   (b)

Figure 5.14: Comparison between numerical solutions and analytical predictions of linear wave parameters for waves of period $T = 4$ s. Figure (a) shows the time series for the analytical solution with no cylinder present η_∞, numerical solution using slip cylinder wall condition η_S and the diffracted surface elevation η_D. Figure (b) is the time series for wave forces calculated with the Morison equation, F_M, numerically predicted wave forces using a slip wall condition, F_M, and the analytically calculated wave force due to diffraction, F_D.

The results from the numerical model agree well, though a reduction in the velocity is seen across all simulations. For waves where $D/\lambda \ll 0.2$ and diffraction effects are not expected, the wavelength-to-depth ratio λ/h reduces. Waves are considered to propagate in shallow water if the ratio $\lambda/h < 0.05$, but it is conceivable that bottom friction effects cause a decrease in wave velocity for $T = 8$ and 10 s, evidenced by the decreasing KC and Re values. Whilst it is commonly accepted that diffraction

(a)   (b)
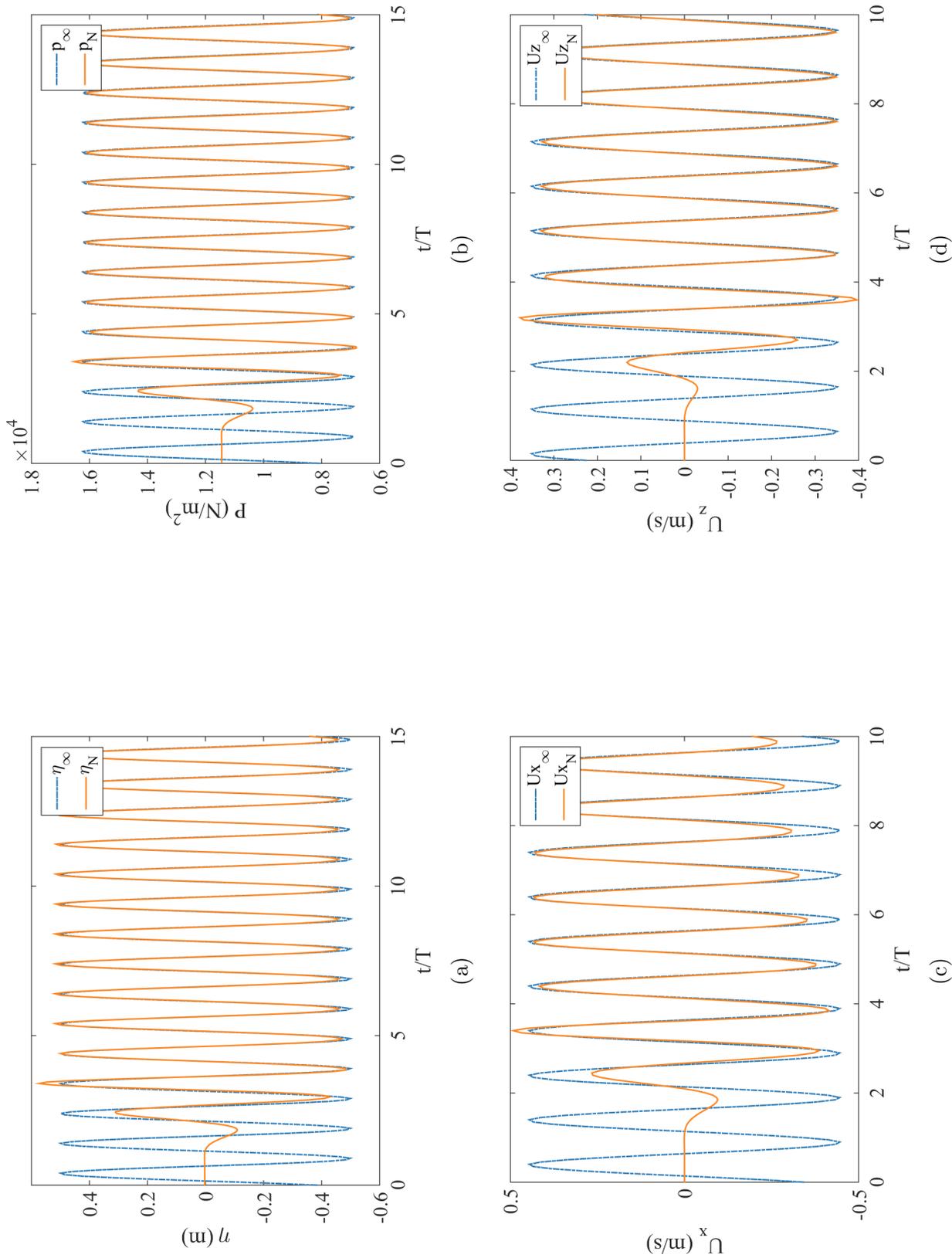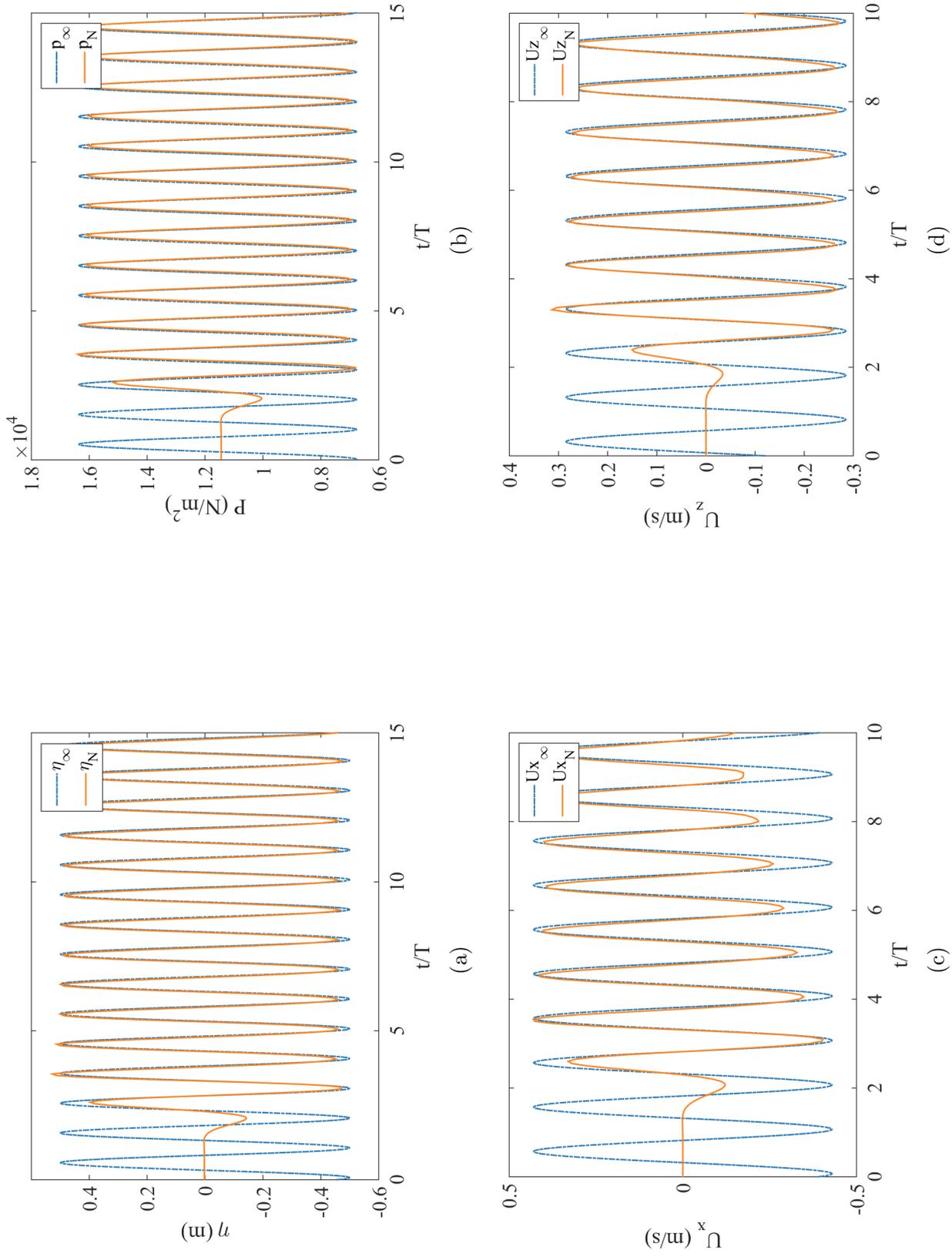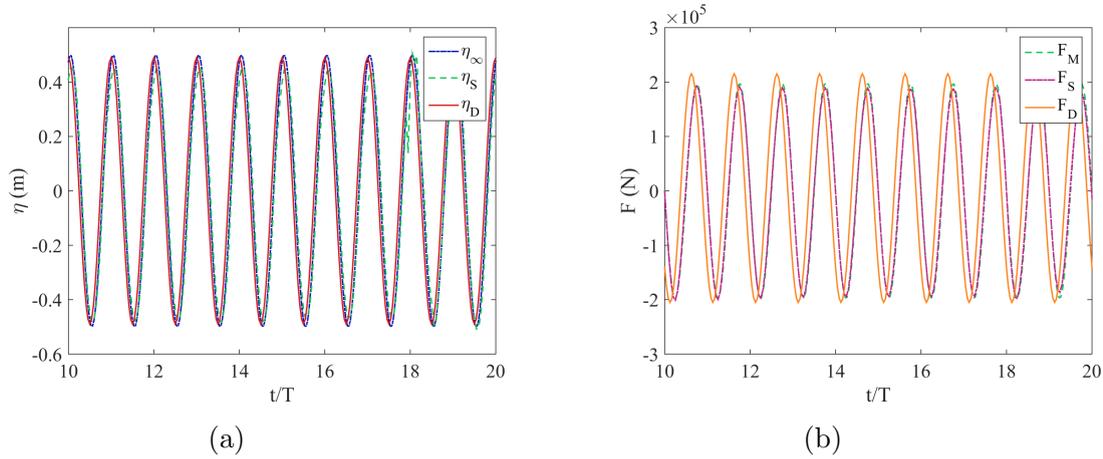
Figure 5.15: Comparison between numerical solutions and analytical predictions of linear wave parameters for waves of period $T = 6$ s. Figure (a) shows the time series for (a) the analytical solution with no cylinder present η_∞, numerical solution using slip cylinder wall condition η_S and the diffracted surface elevation η_D. Figure (b) is the time series for wave forces calculated with the Morison equation, F_M, numerically predicted wave forces using a slip wall condition, F_M, and the analytically calculated wave force due to diffraction, F_D.

(a)   (b)
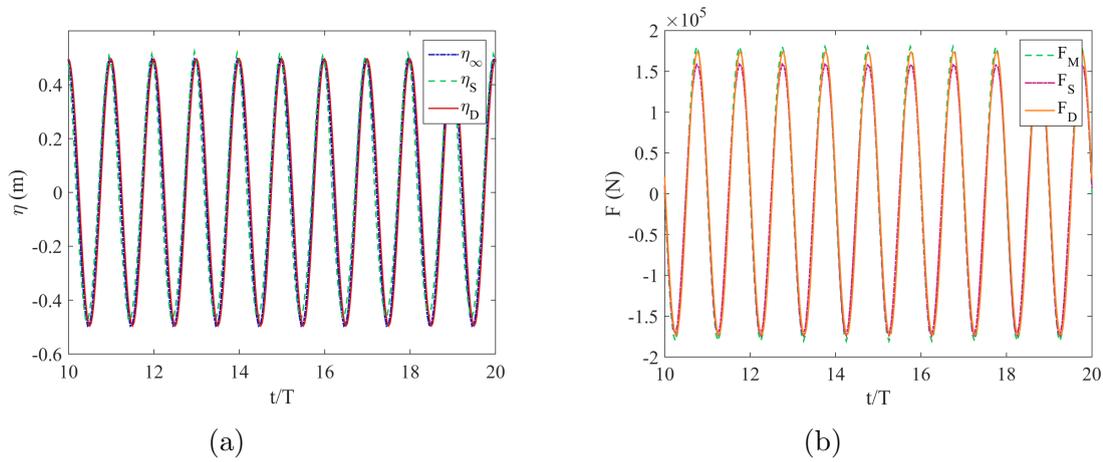
Figure 5.16: Comparison between numerical solutions and analytical predictions of linear wave parameters for waves of period $T = 8$ s. Figure (a) shows the time series for (a) the analytical solution with no cylinder present η_∞, numerical solution using slip cylinder wall condition η_S and the diffracted surface elevation η_D. Figure (b) is the time series for wave forces calculated with the Morison equation, F_M, numerically predicted wave forces using a slip wall condition, F_M, and the analytically calculated wave force due to diffraction, F_D.
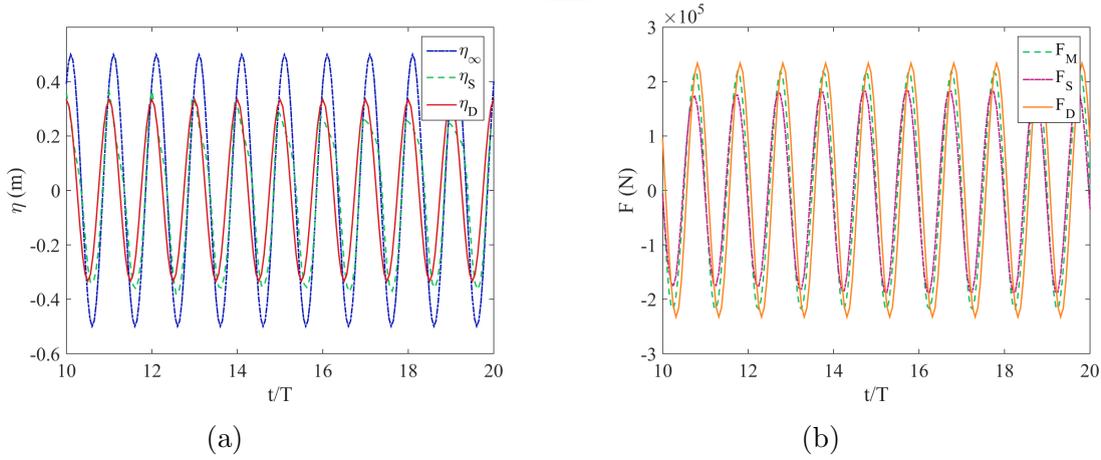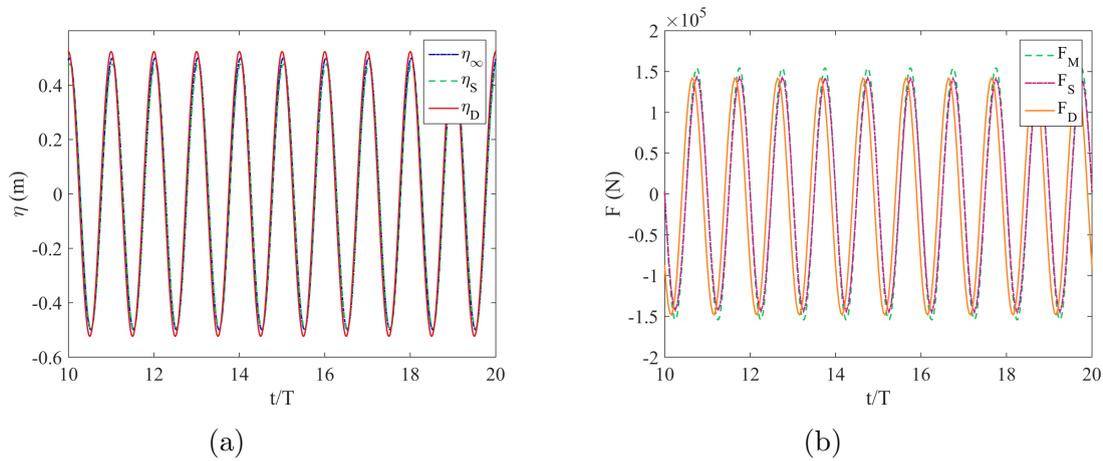
Figure 5.17: Comparison between numerical solutions and analytical predictions of linear wave parameters for waves of period $T = 10$ s. Figure (a) shows the time series for (a) the analytical solution with no cylinder present η_∞, numerical solution using slip cylinder wall condition η_S and the diffracted surface elevation η_D. Figure (b) is the time series for wave forces calculated with the Morison equation, F_M, numerically predicted wave forces using a slip wall condition, F_M, and the analytically calculated wave force due to diffraction, F_D.

effects occur when $D/\lambda \geq 0.2$, such effects have also been noted to occur for ratios as low as 0.1 (Chakrabarti, 1987), and so it can be expected that some diffraction effects occur at $T = 6$ s.

5.6   Discussion and Conclusions

OpenFOAM appears to provide accurate predictions for linear wave simulation both for waves in an open numerical wave tank and for waves past a cylinder. Although relaxation zones are still necessary to absorb outgoing and reflected waves, it is found that reducing the ζ value in the relaxation function (5.3) allowed a reduction in the computational domain length and no wave reflection was observed when a relaxation zone of length λ with $\zeta = 1$ was used.

Wave components in the horizontal and vertical directions, pressure

116

due to waves, and undisturbed surface elevations were compared for four different wave parameters, $T = 4$, 6, 8, and 10 s. While the values match well, a slight reduction was seen in the horizontal velocity component. This could be due to the numerical scheme, although no additional tests were run because the discrepancy is small.

The interaction between waves with the same parameters and a surface-piercing fixed monopile were then simulated. The monopile diameter corresponded to turbine support structure diameters found at Teesside Offshore Wind Farm, and the diameter-to-wavelength ratio effect on the wave-structure-interaction was explored. The numerical predictions of the diffracted wave height corresponded well to analytical values found from linear diffraction theory.

It is also seen that as the wavelength increases, the effects due to diffraction decrease and the diffracted wave height becomes equivalent to the undisturbed wave height for the longer wave periods. This result can be expected from diffraction theory and the influence of the cylinder is particularly clear in comparing figures 5.10 and 5.14.

The wavelength-to-diameter ratio is 0.2, well within the regime where diffraction substantially influences the flow. The reduction in wave heigh due to the presence of the cylinder is apparent in the values from both the analytical diffracted calculation and the numerical prediction. Mesh refinement required when including the cylinder in the simulation also appeared to have a stabilising effect on the numerical surface elevation, pressure and velocity time series, especially for simulations of waves with period $T = 4$ s, where the mesh density used in the simulation without the cylinder was likely too coarse and showed a small increase in the location of the surface elevation over time.

Numerical predictions of the wave values with and without a cylinder present demonstrate the increasing influence of the cylinder as the diameter-to-wavelength ratio increases. With the linear wave properties verified, the model is next extended to include irregular waves. Simulations of specific sea states are presented in the following chapter.

Chapter 6

Results: Model Validation in OpenFOAM and Discussion

Summary

The linear wave model presented in Chapter 5 is now extended to simulate an irregular wave field, governed by the equations presented in Section 2.3. Numerical and analytical formulations are employed to determine the water particle kinematics, wave force and significant wave height (H_s) from ocean wave data provided by practitioners. The irregular sea state is modelled numerically in OpenFOAM with an upstream boundary condition derived from wave energy spectra obtained by analysis of existing field measurements of free surface wave displacement from Teesside Offshore Wind Farm located in the Southern North Sea off the east coast of the United Kingdom. Measured wave conditions are represented numerically and analytically, and the fluid-structure interaction with a surface-piercing turbine monopile is computed.

6.1 Introduction

The principal limiting condition for CTV operation at an offshore wind farm is that the significant wave height H_s remains below a certain limit. For most CTVs, the limiting criterion is $H_s \leq 1.5$ m (Halvorsen-Weare et al., 2013, Dalgic et al., 2015b). However, the use of significant wave height as the main access criterion introduces additional uncertainty because H_s is dependent on specific *in situ* wave and wind conditions and also on the conditions in close proximity to the monopile. In addition, H_s provides no information about the wave kinematics at the site, including whether the sea state has a unimodal or bimodal spectral distribution.

Data from a single wave buoy located at Teesside Offshore Wind Farm in the southern North Sea, shown in figure 6.1 for location and array set-up, was provided for this project. From the wave buoy data, the surface displacement is tracked for a 24-hour period in each season throughout period 2015-2016. Data were provided for September 2015, December 2015, March 2016 and June 2016, giving a wide range from which to determine seasonal changes in the sea state. The wave buoy seen in figure 6.2 tracks the displacement of the free surface in cm at a sampling frequency $F_s = 1.28$ Hz. The water depth at Teesside Offshore Wind Farm, where the turbine monopiles of interest are located, is 15 m on average.

In this chapter, a statistical analysis of practitioner data was used to simulate numerically and analytically the unidirectional sea state in an open wave field and the wave interaction with a surface-piercing turbine monopile support column. Analytical and numerical methods outlined in Chapters 2, 3, and 4 are applied to calculate the local water particle kine-
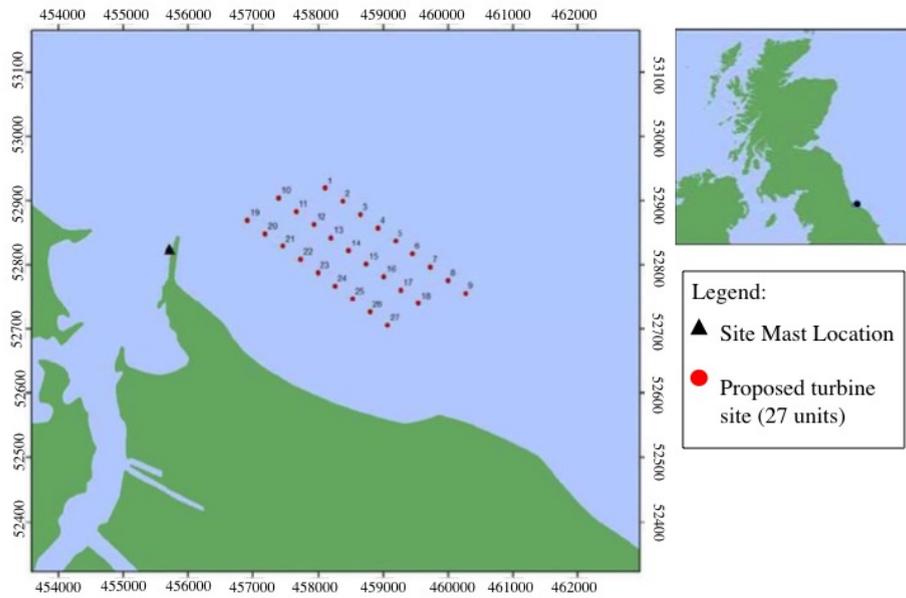
Figure 6.1: Location of Teesside Offshore Wind Farm. Image provided by EDF Energy Renewables.

0.7 m DWR-MkIII with optional painted hull

Figure 6.2: Datawell Waverider Wave Buoy (DWR‿ MkIII). Image from EDF Energy Renewables.

matics and wave loading on an individual turbine monopile at Teesside Offshore Wind Farm.

Section 6.2 summarises the numerical set-up and Section 6.3 introduces the numerical driving boundary condition. The boundary condition is a modification of the wave types included in the Waves2Foam release, which are linear waves (Stokes 1st order), nonlinear (Stokes 2nd and 5th orders, cnoidal waves) and irregular waves from either a JONSWAP or Pierson-Moskowitz spectrum. The boundary condition developed for this project, *customSpectrum*, allows input of verified spectral information derived from the field data directly into OpenFOAM simulations. Section 6.4 presents the results from calibration of the input boundary condition. The boundary condition was calibrated by simulating the sea state in an numerical wave tank and using statistical checks to verify that the correct sea state is produced. In Section 6.5, the interaction between the actual sea state found at Teesside Offshore Wind Farm and the monopile support column was computed, where the total in-line wave force and local hydrodynamic field were determined. Conclusions regarding the ability of the models in producing the local sea state are given in Section 6.6.

6.2   Numerical Set-Up

The horizontal dimensions of the computational domain were set according to the maximum modal wavelength λ_p, representing the longest wavelength in the spectral distribution. The computational domain is of length $4\lambda_p$ in the wave propagation direction x and length λ_p in the transverse direction y. The vertical dimension z occupied 15 m of still water depth, with a further 10 m of air above the water free surface to

avoid surface diffusion. In cases involving bimodal spectra, two T_p values were evident, and the larger value was used to set the computational domain length, whilst the smaller value was used to ensure that all waves were sufficiently sampled.

A cut-off frequency was employed to remove the longest wavelengths in the low-energy part of the spectrum and hence alleviate the computational domain length, thus enhancing computational performance. The peak period was limited throughout to $T = 13$ s, such that the maximum wavelength was $\lambda \sim 150$ m. The shortest waves considered when bimodal spectra occur corresponded to a minimum period of $T = 1.5$ s, with an associated minimum wavelength $\lambda \sim 4$ m. In Section 5.4.4, it was found that 75 cells per wavelength in the horizontal direction were sufficient. A minimum of 7 cells in the vertical direction were used, chosen based on the validation results of linear monochromatic waves in presented in Chapter 5. In the present study, such a fine mesh density could not be achieved for the highest frequency waves (with the shortest wavelengths), and so a minimum of 6 cells in the horizontal direction was set for the shortest wavelengths (≈ 4 m) to control the computational overhead.

For all simulations, a relaxation zone of length λ_p was located at the outlet where an undisturbed sea state was assumed. When the interaction with the turbine monopile was considered, an inlet relaxation zone of length λ_p was also applied.

6.3 Input of Wave Buoy Data to Open-FOAM

In order to utilise data from the offshore wind farm, fixed-value boundary condition values for velocity were retrieved from the wave spectrum S_η, obtained from measured wave field data. The boundary condition was developed based on the source code provided in the Waves2Foam release for calculation of the sea state from a JONSWAP spectrum.

FFT analysis of the free surface displacement data measured from a wave buoy was used to produce the wave spectrum for each seasonal data set, and (2.32) was applied within the source code to calculate the wave amplitudes from the spectral data. A random phase value $0 \le \psi \le 2\pi$ was applied within the time-dependent periodic term in (2.33). In-line and vertical velocity components at all locations within the fluid domain on the inlet boundary were then calculated within the source code using (2.34) and (2.35).

The *waveFoam* solver also uses the PISO algorithm described in Section 4.5 to solve the momentum equation from the initial boundary velocity values and then evaluates the pressure before correcting the flux. The *waveFoam* solver finds solutions for the incompressible RANS equation, given by (4.5) and reproduced here for clarity,

$$\frac{\partial \mathbf{u}}{\partial t} + \nabla \cdot \left[\mathbf{u}\mathbf{u}^{\mathbf{T}} \right] - \nabla \cdot \left[\nu \nabla \mathbf{u} \right] = -\frac{1}{\rho} \nabla p^* - g \cdot \mathbf{x}, \qquad (6.1)$$

where $\mathbf{u}$ is the velocity vector, p^* is the pressure, ρ is the fluid density, ν is the coefficient of kinematic viscosity, g is gravitational acceleration acting vertically downwards, and $\mathbf{x}$ is the location vector. The source

code can be edited directly using templates provided within the Open-FOAM and Waves2Foam releases. The source code is written in C++ and both header (.H) and main (.C) files require editing. The mathematical expression from equation (2.32) is implemented within the customSpectrum.C file, which reads directly from the file containing the frequency and spectral values.

Once the amplitudes have been determined, the fixed-value boundary condition calculates the value of the in-line and vertical velocity components u and w from (2.34) and (2.35) respectively, for all cells on the boundary; the PISO algorithm is then applied to calculate and correct the pressure values.

Prior to simulation, the numerical wave amplitudes calculated at the boundary using *customSpectrum* were compared to the corresponding analytical results. This comparison ensured that the sea state produced contained the correct wave amplitudes; figure 6.3 illustrates the comparisons. In figure 6.3, dissimilarities between the values can be seen where the spectral frequency cut-off values were employed to limit the wavelengths and mesh size. Once the initial values calculated by OpenFOAM were compared against the analytical amplitude values, the *customSpectrum* boundary condition was applied at the inlet for each of the four seasonal data sets, where the boundary values for each set corresponded to the seasonal spectral data. Simulations were run first for the local sea state in an open numerical wave tank with no monopile present.
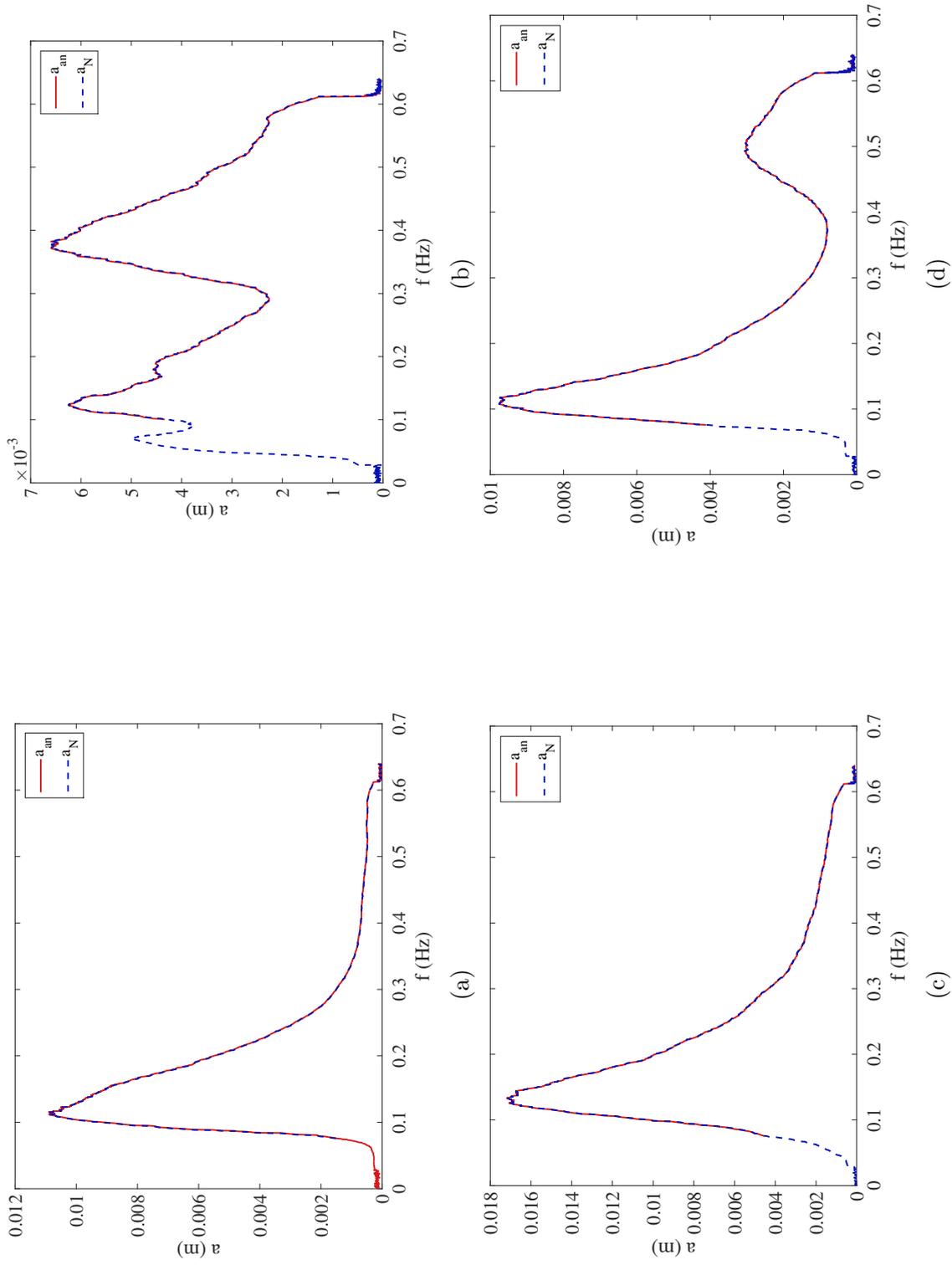
Figure 6.3: Predicted amplitude as a function of wave frequency calculated in OpenFOAM a_N compared to the analytical formulation a_{AN} for (a) September 2015, (b) December 2015, (c) March 2015 and (d) June 2016.

6.4 Wave spectral results for Teesside input sea state

Four simulations were completed for the open sea over spring, summer, autumn and winter conditions. The simulations were run in parallel using 24 processors on a supercomputer operated by ICHEC. Spectral analyses of the input wave data produces a unimodal spectral distribution for two of the datasets and a bimodal spectral distribution for the other two, although the second peak in the June 2016 dataset made only a small contribution to the total energy. For the bimodal sea states in December and June, a much greater mesh density was needed to capture the shortest wavelengths adequately, significantly increasing the computational time. Table 6.1 shows wave parameters, mesh details and the total CPU time for a simulation of duration $t^* = 30$, where $t^* = t/T_p$.

Table 6.1: Total CPU hours for each simulation of the undisturbed sea state

Season	Min/Max λ (m)	No. Elements	CPU Time
September 2015	12.7/164	786,050	4 h 10 min
December 2015	4.3/290	1,330,550	14 h 50 min
March 2016	7.7/178.6	882,050	5 hr 48 min
June 2016	4.3 /164	1,580,040	17 hr 10 min

The spectral information was verified through a statistical analysis of the wave buoy data noting that the variance of the surface elevation σ_η^2 is equivalent to the total energy within the spectral density curve m_0 for the *in situ*, analytically calculated and simulated results. The significant wave height H_s was also determined for each method from (2.31) and the

modal period T_p identified for each set of data. The statistical values are included in Tables 6.2-6.5.

A slip-boundary condition was applied at the sea bed, a fixed-value wave absorption boundary condition at the outlet; an inlet-oulet boundary condition was applied at the atmospheric upper boundary of the domain, analogous to the verification cases presented in Chapter 5. Symmetry boundary conditions were applied on the walls of the domain to represent open sea conditions.

Using a FFT, the horizontal and vertical water particle velocity components were also calculated and comparisons made between the analytically determined sea state and the numerically simulated sea state. The subscript *raw* refers to the spectrum of the *in situ* data and the subscript *an* refers to the spectrum calculated using the analytical formulation of the surface elevation from (2.33). The subscript N denotes the numerical results. The spectral result and time-series data for each season are first presented graphically in Figures 6.4-6.7, and the statistical values for σ_η^2, m_0, H_s and T_p are given in Tables 6.2-6.5.

Table 6.2: Autumn Statistical Values - September 2015

	Raw data	Analytical sea state	OpenFOAM	Percentage error
$\sigma_\eta^2 = m_{0,\eta}$	0.018 m^2	0.018 m^2	0.020 m^2	10.8 %
$H_s = \sqrt{m_0}$	0.53 m	0.53 m	0.56 m	5.1 %
T_p	8.69 s	8.69 s	8.08 s	7.1 %

The model provides a satisfactory approximation of both peaks in a bimodal spectrum, although the accuracy is greatly reduced for multi-directional or crossing seas. Both significant wave height values, analytical and numerical, are within 5% of each other for three out of the four
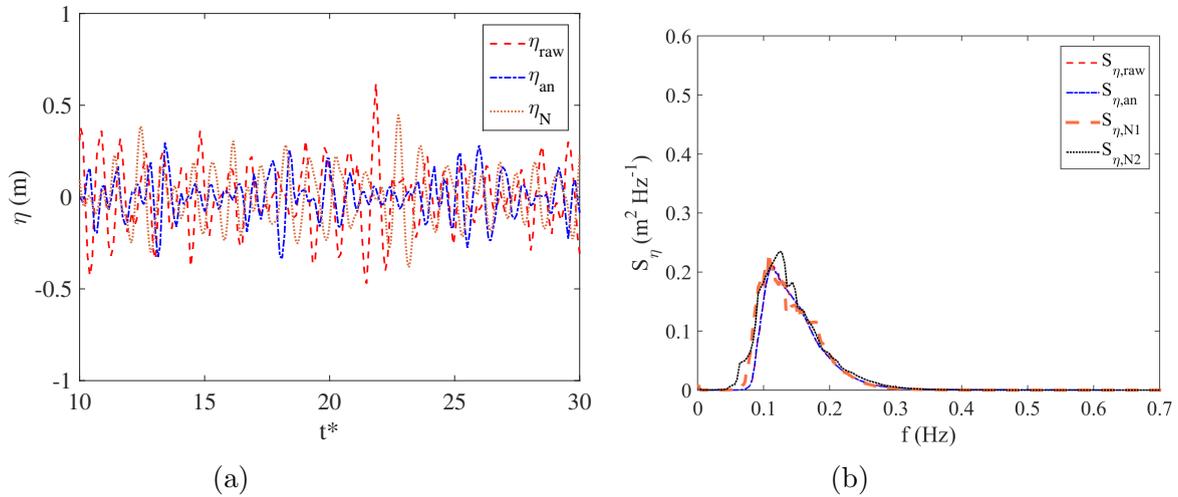
Figure 6.4: Autumn time series for (a) free surface elevation and (b) associated wave spectrum. Subscripts raw, an, N represent values obtained from the *in situ* data set, analytical representation and numerically simulation respectively. Figure (b) includes an additional numerical simulation, represented by the subcaption N2, to demonstrate mesh convergence.
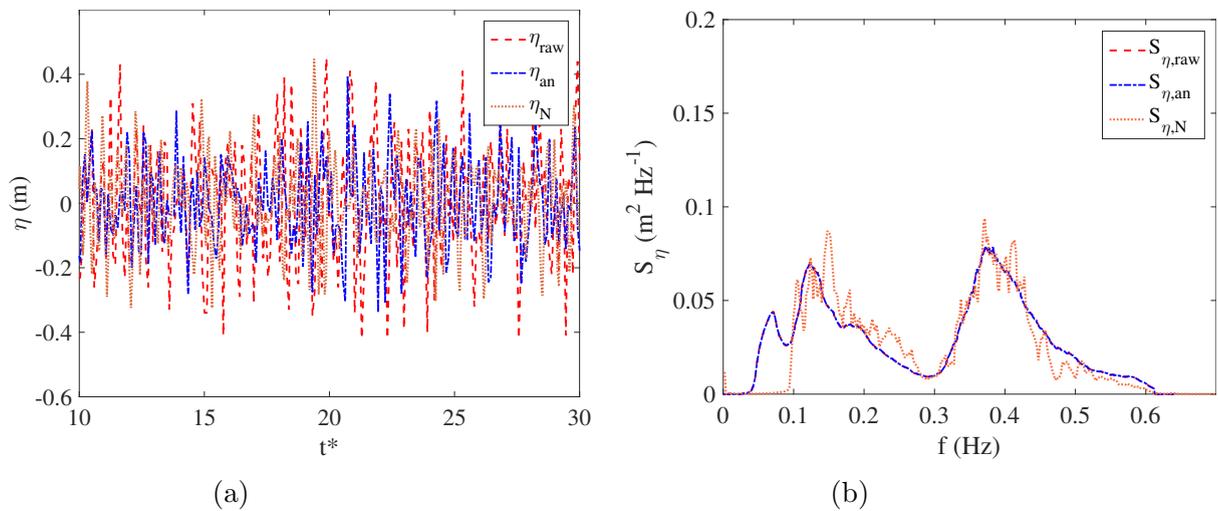
Figure 6.5: Winter time series for (a) free surface elevation and (b) associated wave spectrum. Subscripts raw, an, N represent values obtained from the *in situ* data set, analytical representation and numerically simulation respectively.

Table 6.3: Winter Statistical Values - December 2015

	Raw data	Analytical sea state	OpenFOAM	Percentage Error
$\sigma_\eta^2 = m_{0,\eta}$	0.018 m^2	0.018 m^2	0.017 m^2	5.6 %
$H_s = 4\sqrt{m_0}$	0.54 m	0.54 m	0.52 m	3.7 %
T_{p1}	8.11 s	8.11 s	7.25 s	10.6 %
T_{p2}	2.61 s	2.61 s	2.69 s	3.0 %

(a) (b)
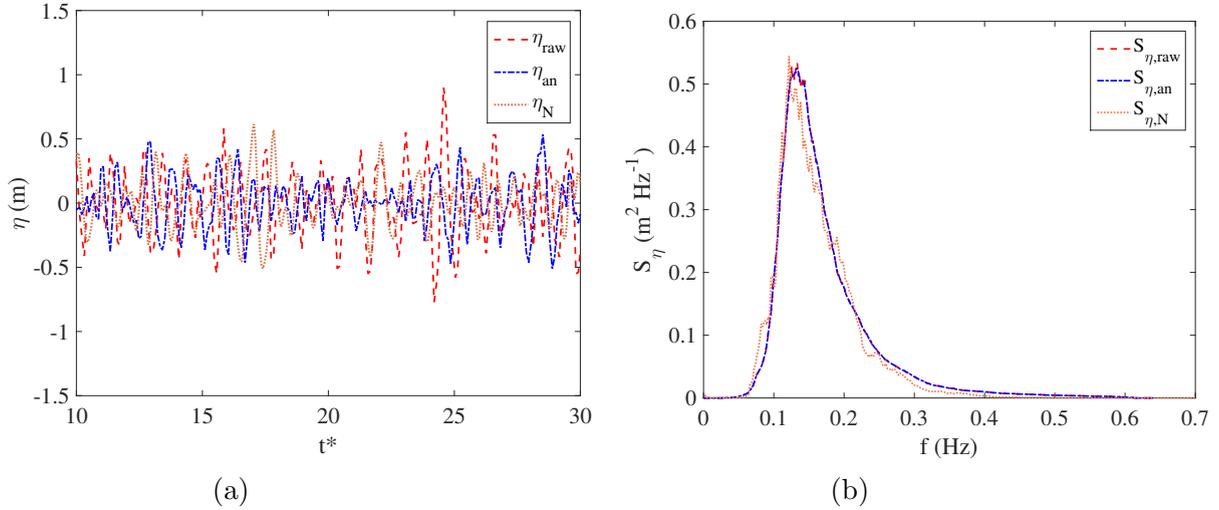
Figure 6.6: Spring time series for (a) free surface elevation and (b) associated wave spectrum. Subscripts raw, an, N represent values obtained from the *in situ* data set, analytical representation and numerically simulation respectively.

Table 6.4: Spring Statistical Values - March 2016

	Raw data	Analytical sea state	OpenFOAM	Percentage Error
$\sigma_\eta^2 = m0, \eta$	0.050 m^2	0.050 m^2	0.047 m^2	6.0 %
$H_s = 4\sqrt{m_0}$	0.89 m	0.89 m	0.87 m	2.2 %
T_p	7.50 s	7.50 s	6.80 s	9.3 %

Table 6.5: Summer Statistical Values - June 2016

|	Raw data	Analytical sea state	OpenFOAM	Percentage Error
$\sigma_\eta^2 = m_{0,\eta}$	0.015 m^2	0.015 m^2	0.012 m^2	20.0 %
$H_s = 4\sqrt{m_0}$	0.49 m	0.49 m	0.44 m	10.2 %
T_p	9.30 s	9.30 s	8.35 s	10.2 %

(a)   (b)
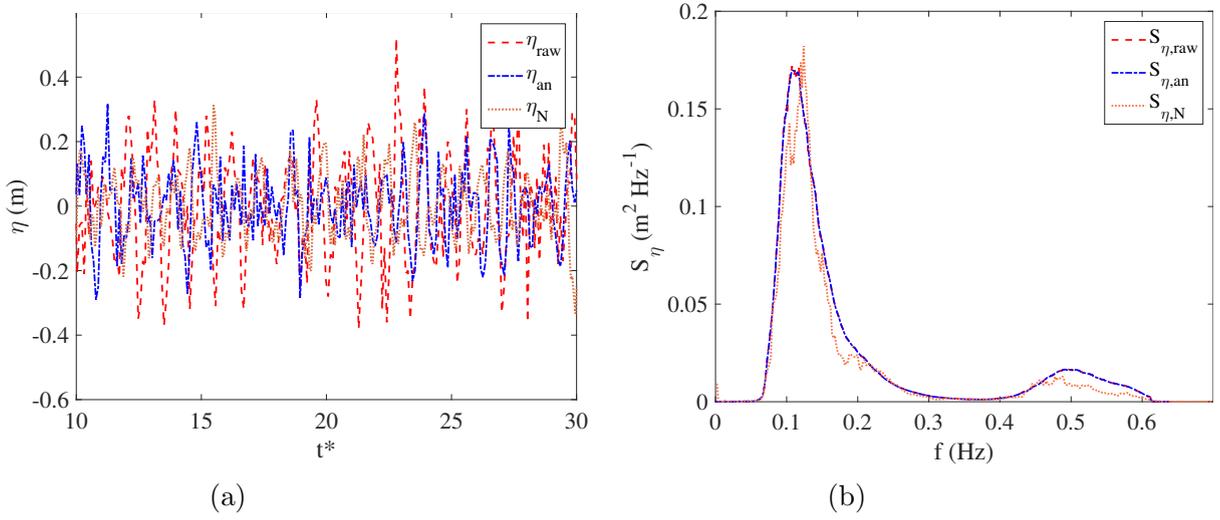
Figure 6.7: Summer time series for (a) free surface elevation and (b) associated wave spectrum. Subscripts raw, an, N represent values obtained from the *in situ* data set, analytical representation and numerically simulation respectively.

data sets, but not the June 2016 dataset. A small second peak around 0.5 Hz is visible in the June 2016 data set; although the numerical model does capture the peak location, the spectral peak has a wider spread than that seen in the analytical and raw wave buoy spectra. This also occurs for the December 2015 data set, where both peaks are captured but the peaks have a wider spread in the numerical model.

The left-hand images in Figures 6.4-6.7 show the time series of the free surface elevation as calculated analytically (η_{an}) and numerically (η_N), and compared to the original displacement data (η_{raw}). Although phase information was not conserved for the surface elevation time series, the results in the frequency domain exhibit good agreement between the raw, analytical and numerical results. Larger differences were found between σ_η^2 and m_0 (up to 20% difference for June 2016).

Table 6.1 indicates there is a very significant difference in the total CPU time required to process the December 2015 and June 2016 datasets

in comparison to September 2015 and March 2016. This is because of the bimodal spectra generated from the former two data sets, where shorter frequency waves contribute significantly to the total energy. Although the same minimum wavelength (maximum wave frequency) was used for both June 2016 and December 2015 data, an increase in energy at the lowest frequencies in the winter spectrum meant that longer wavelengths were included.

The simulated undisturbed irregular inlet sea state presented in this section provides a satisfactory estimate of the actual wave conditions found at Teesside Offshore Wind Farm. The numerically simulated sea state corresponds well to the *in situ* data, and therefore can be used to determine the significant wave height and modal wave periods at the wind farm. Subsequently, the inlet sea state was henceforth used as the input condition for determining the diffracted wave kinematics for a turbine monopile undergoing loading from the specific sea state found at Teesside. Section 6.5 presents the results obtained for this fluid-structure interaction and the wave particle kinematics in the vicinity of the monopile.

6.5 Teesside Data: Interaction with a monopile

Free surface flow past a turbine monopile is now simulated for the four seasonal sea states at Teesside Offshore Wind Farm. Table 6.1 lists the minimum and maximum wave periods and corresponding wavelengths used. As in Chapter 5, the turbine monopile support structure is modelled as a surface-piercing bottom-fixed smooth cylinder in long-crested small-amplitude waves. The open-source meshing tool *Gmsh* was used to construct the mesh using the structure shown in Figure 5.2. The

same mesh parameters as used in the previous simulations of the irregular sea state in an open sea were applied, where a minimum of 75 cells per modal wavelength were used and the shortest wavelengths in the bimodal spectra only used 7 cells per wavelength. Within the transition zone around the cylinder, the cell length was reduced by half, to capture rapidly changing gradients within this region. The boundary conditions applied were again the same as previous simulations and results for both slip and no-slip boundary conditions on the cylinder walls were examined. Each simulation was run for $t^* = 40$.

Numerical wave gauges for capturing the surface elevation are again applied near the inlet of the domain, and also at 16 locations around the cylinder at a distance of $0.1D$ away from the cylinder wall. Numerical probes for recording other parameters (velocity, pressure, etc) were placed at the same locations. Figure 6.8 illustrates the wave gauge and numerical probe locations. Values for the diffracted waves were taken from wave gauge 11 (labeled wg11 in the figure), located at the rear stagnation point of the cylinder.

6.5.1   Irregular Diffracted Wave Results

Figure 6.9 presents a visualization of the wave free surface at time $t^* = 35$ for the sea state during March 2016, obtained using the numerical model with a surface-piercing, circular cylinder representing a turbine support column. The values of surface Reynolds number and Keulegan-Carpenter number are 1.22 x 10^6 and 0.35, respectively. A diffraction pattern is visible upstream of the cylinder, whereas a laminar wake has developed downstream. Viscous effects cause a velocity reduction in the wake of the cylinder. There is evidence of vorticity streaming into the wake but
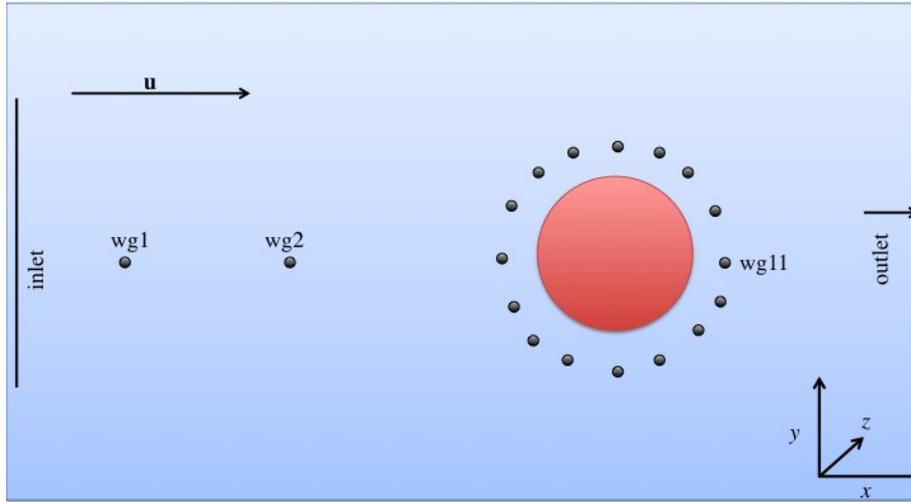
Figure 6.8: Location of numerical wave gauges. Results are presented for data obtained from wg11, located at the rear stagnation point of the cylinder.

no vortex shedding, which is to be expected at such a low Keulegan-Carpenter number. Similar diffraction-wake patterns were obtained using the numerical model for input wave data from each season.

Figure 6.10 presents wave spectra obtained by taking the Fourier transform of the free surface elevation time series at the rear stagnation point of the cylinder, where the boat landing would ideally be located, for each of the four seasons. Each subplot shows: the undisturbed wave spectrum S_η; the diffracted wave spectrum obtained using linear diffraction theory $S_{\eta,\mathrm{D}}$; the numerical wave spectrum using a slip-boundary condition on the cylinder $S_{\eta,\mathrm{S}}$; the corresponding wave spectrum using a no-slip condition $S_{\eta,\mathrm{N}}$. The undisturbed wave spectral estimates were previously validated against raw *in situ* sea state data in Section 6.4. Overall, the undisturbed, linear diffracted and numerical diffracted pro-
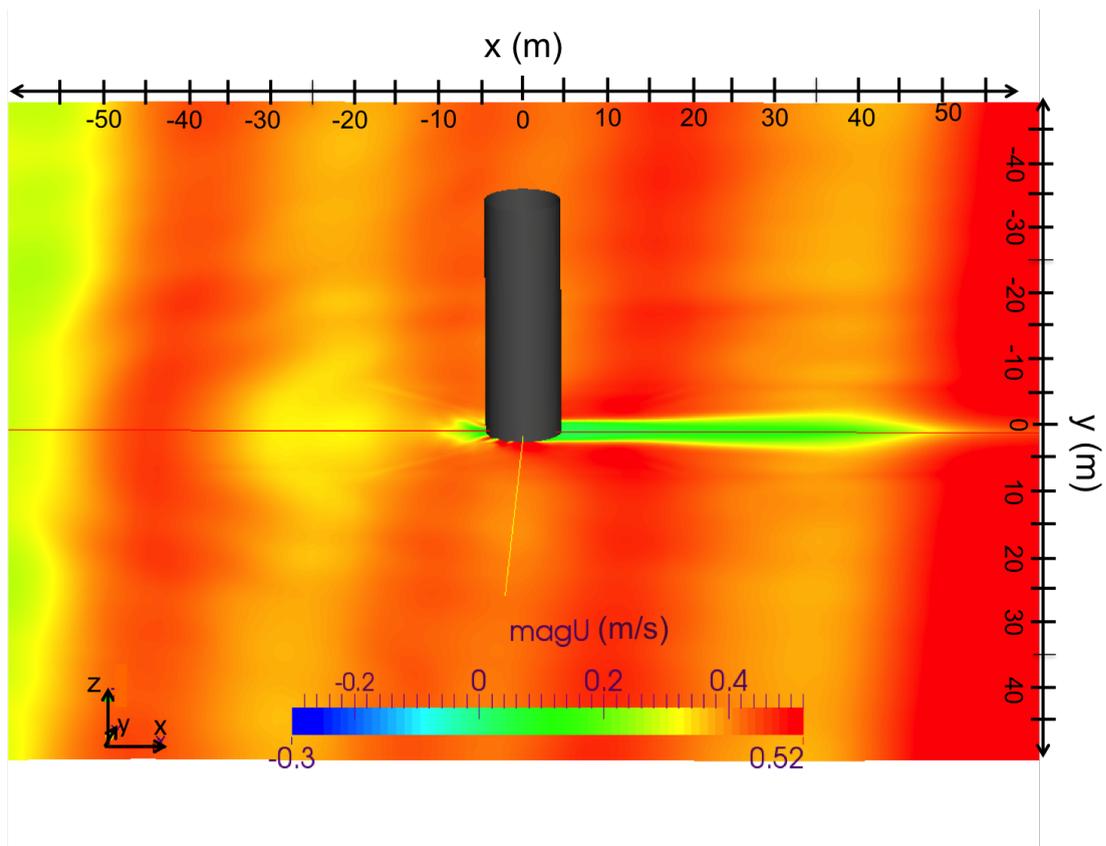
Figure 6.9: Paraview visualization of wave diffraction pattern showing wake formation in the vicinity of a large-diameter surface-piercing cylinder, representing a turbine monopile. Wave input is from the March 2016 data set.

files and peak frequencies of the horizontal and vertical velocity spectral functions obtained for the September, March, and June data sets are quite similar.

For the December data set, the numerical solution does not agree well with the analytical solutions, which have a second definite peak at about 0.4 Hz ($T_p \sim 7$ s). However, both the analytical and numerical results present a peak at ~ 0.15 Hz ($T_p \sim 2.3$ s). It was initially hypothesised that the higher-frequency waves were under-sampled in the wave direction, leading to dissipation of these higher-frequency waves over the length of the computational domain. A further theory suggested that

waves were under-sampled in the vertical direction due to the decrease in overall energy and wave height within the winter data set in comparison to the other three data sets.

Table 6.6 lists values of significant wave height H_s determined from the undisturbed and diffracted wave fields. The analytical and numerical diffracted wave spectra show a reduction from the incident wave spectrum.

Table 6.6: Significant wave heights for Teesside Farm covering all seasons over the 2015-2016 year

Date	$H_{s,\infty}$ (m)	$H_{s,\mathrm{D}}$ (m)	$H_{s,\mathrm{S}}$ (m)	$H_{s,\mathrm{N}}$ (m)
Sept. 2015	0.53	0.39	0.34	0.32
Dec. 2015	0.54	0.42	0.32	0.30
March 2016	0.89	0.63	0.59	0.56
June 2016	0.49	0.35	0.29	0.22

The agreement between the analytical diffracted significant wave height value and the numerical value for the diffracted significant wave height ranges from a difference of 6.3% for the March 2016 data set to 23.8% for the December 2015 dataset. However, it must be noted that the H_s value for the bimodal spectrum provides no directionality information and is therefore less reliable in providing information about the December sea state.

Analytical values for the water particle velocity components were calculated from the undisturbed wave spectrum S_η, and the diffracted wave spectrum $S_{\eta,\mathrm{D}}$. Numerical estimates of the diffracted water particle velocities were also obtained from the numerical model. Figure 6.11 presents the horizontal and vertical water particle velocity component spectra obtained over the four seasons. The subscript ∞ indicates the undisturbed spectrum, D the diffracted spectrum, and S and N are the numerical
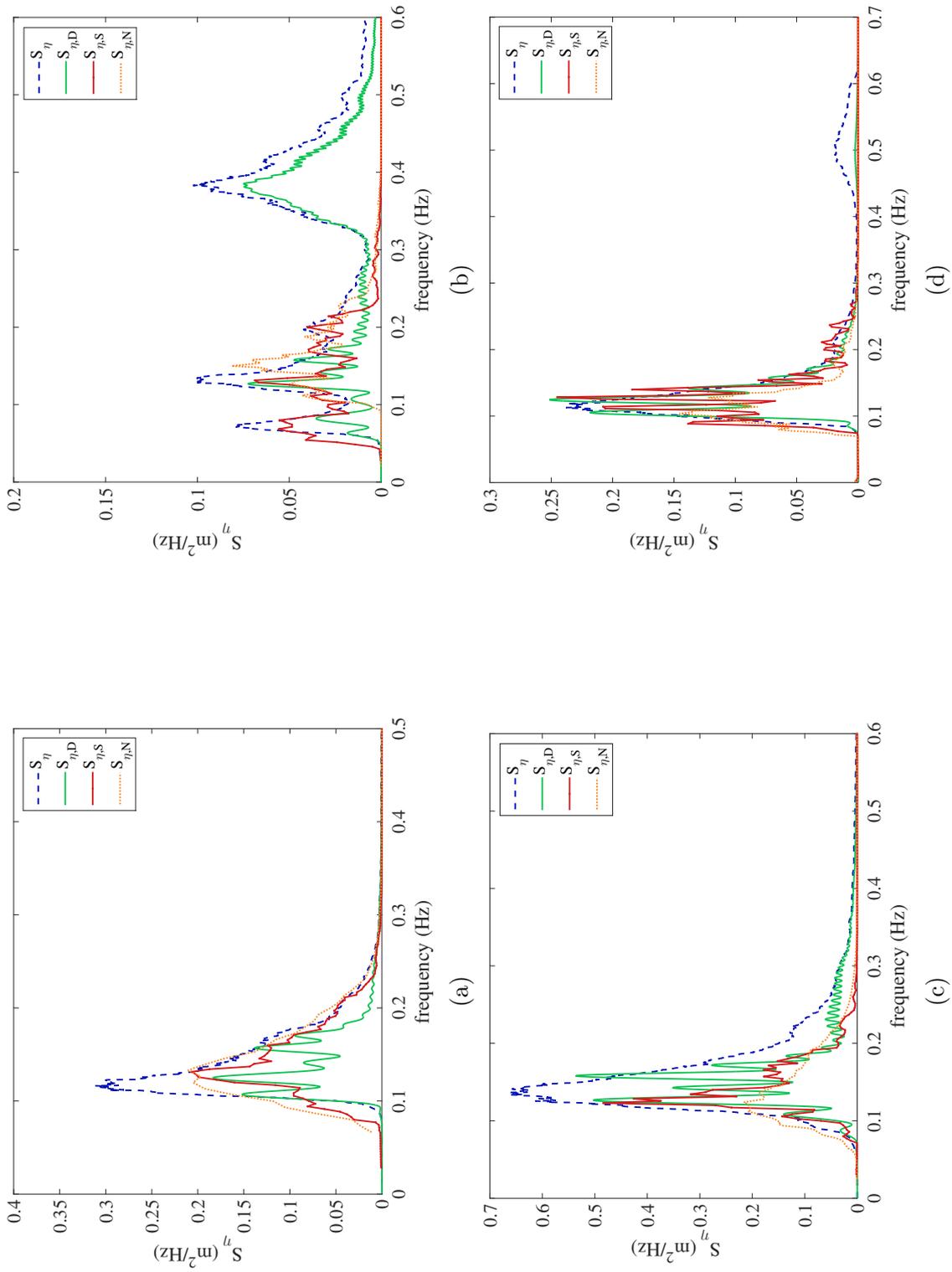
Figure 6.10: Surface elevation wave spectral density functions for the raw surface displacement data, S_η, diffracted wave spectrum $S_{\eta,D}$, numerical wave spectrum with a slip boundary condition, $S_{\eta,S}$, and the numerical wave spectrum using a no-slip boundary condition, $S_{\eta,N}$. Figures display wave spectrum data for (a) Autumn, (b) Winter, (c) Spring and (d) Summer.

spectra obtained using the slip and no-slip boundary conditions, respectively.

The forces acting on the idealised column were then considered. Table 6.7 lists the seasonal values for the surface Keulegan-Carpenter number KC, frequency parameter β, and the drag and inertia coefficients C_d and C_m. For all data sets, C_d and C_m were calculated using the method proposed by Wang (1968) (see Section 3.2.1). The method proposed by Borgman (1965) for calculating the wave force spectrum at a specific height on a circular cylinder should be equivalent to the Morison force density spectrum at the equivalent height. Comparisons of the in-line force spectra at height $z =$ -1.5 m on the cylinder were made.

The force spectrum was first calculated using (3.9) and the Morison equation (Morison et al., 1950) was applied to determine the time-dependent in-line force at the same height. A FFT was again utilised to determine the spectral distribution of the Morison equation at $z =$ -1.5 m. Figure 6.12 compares the force spectrum calculated through the Borgman method and the force spectrum determined from the time-dependent Morison equation. The spectral shape using all methods is very similar to the surface elevation spectral shape; a phenomena first noted by Wiegel et al. (1959).

Results for the non-dimensional coefficients used in the total in-line force spectrum over the length of the cylinder are presented in Table 6.7. Table 6.8 lists the peak spectral force value over the entire submerged length of the cylinder for each season using the different total force calculation methods outlined in Section 3.2. Values of C_d and C_m listed in Table 6.7 were utilised in the total in-line force calculation using the

(c) Spring velocity spectra
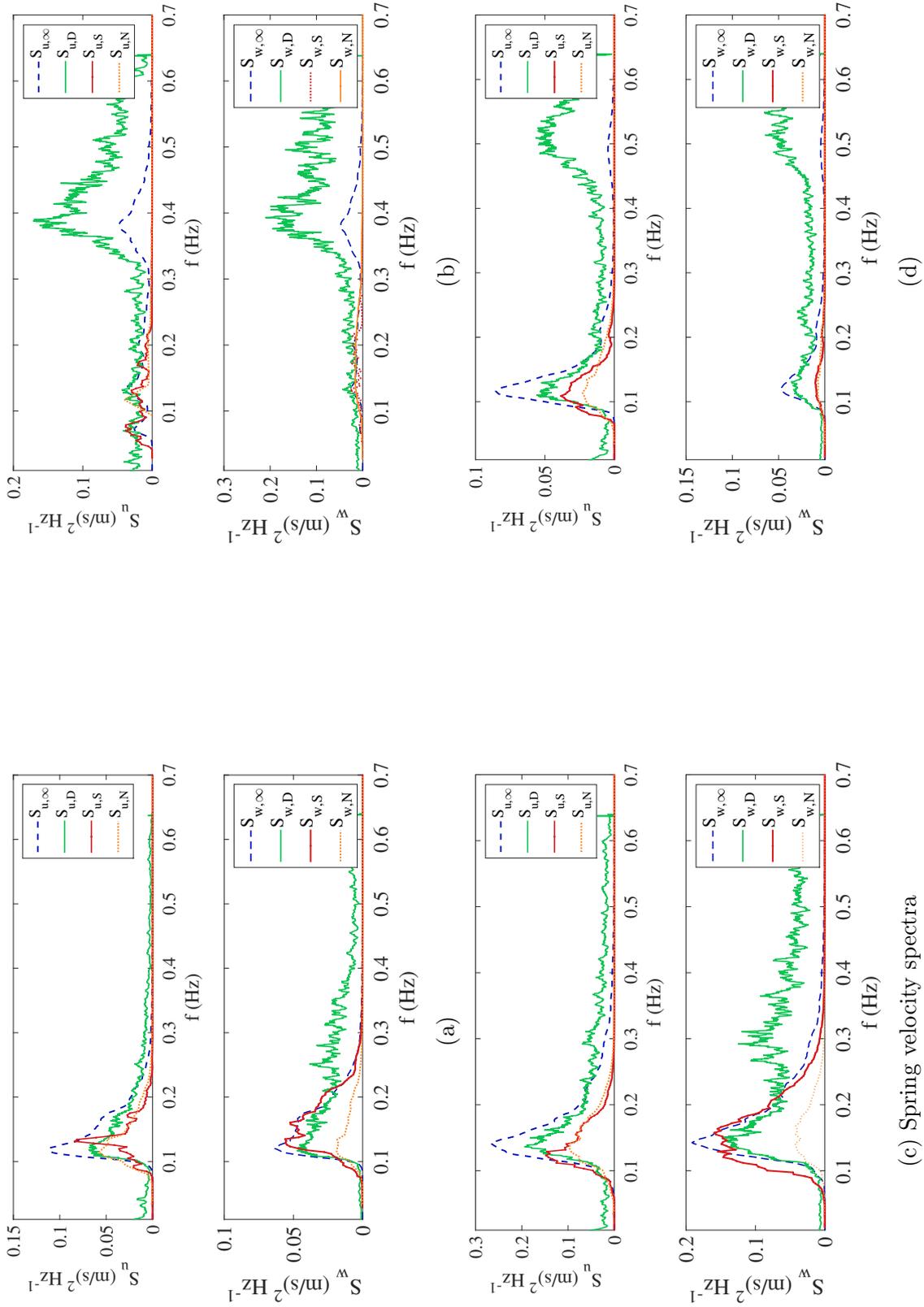
Figure 6.11: Predicted horizontal and vertical velocity component spectra for (a) Autumn, (b) Winter, (c) Spring and (d) Summer at a site in the southern North Sea. Horizontal components are denoted by S_u and vertical by S_w. The subscript ∞ refers to the undisturbed velocity spectrum, D is the diffracted velocity spectrum, S is the numerical spectrum using the slip condition, and N is the numerical spectrum using the no-slip condition.
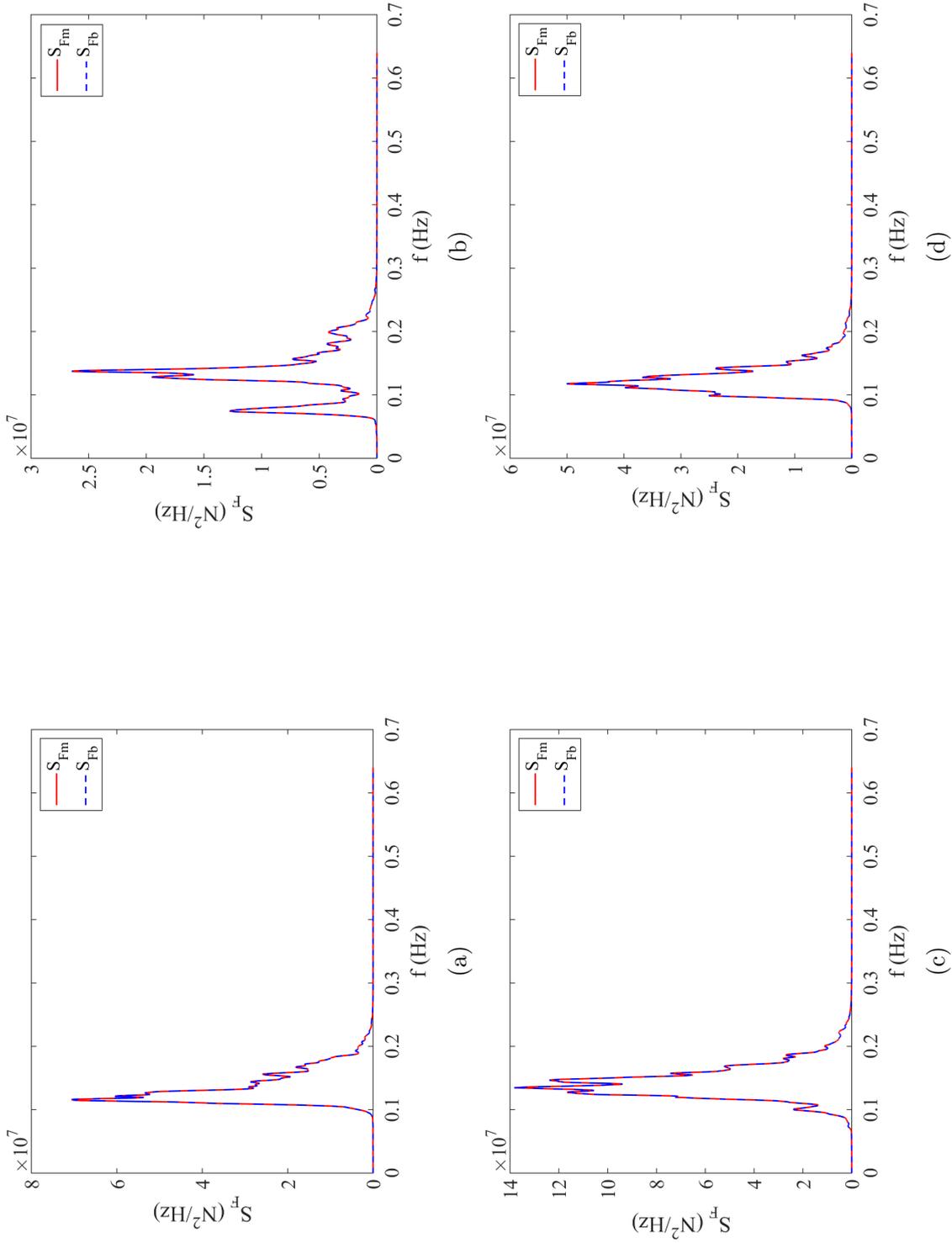
Figure 6.12: In-line force spectrum of wave during (a) Autumn, (b) Winter, (c) Spring and (d) Summer at submerged cylinder height $z = -1.5$ m, S_{Fm} is the Morison force spectrum and S_{Fb} is the force spectrum computed using the Borgman method introduced by Borgman (1965)

.

Morison equation (Morison et al., 1950).

Table 6.7: Non-dimensional parameter values for Teesside Farm covering all seasons over the 2015-2016 year

Date	KC	β	C_d	C_m
Sept. 2015	0.24	2.89×10^6	0.08	2.04
Dec. 2015	0.23	3.28×10^6	0.24	2.00
March 2016	0.35	3.48×10^6	0.05	2.04
June 2016	0.21	2.87×10^6	0.07	2.04

Table 6.8: Peak spectral force values for Teesside Farm covering seasons during the 2015-2016 year. Units are given in $^{\mathrm{GN}^2}/_{\mathrm{Hz}}$

Date	$m_0 \ (F_M)$	$m_0 \ (F_D)$	$m_0 \ (F_S)$	$m_0 \ (F_N)$
Sept. 2015	5.84	5.29	5.27	4.37
Dec. 2015	1.98	1.03	1.27	1.45
March 2016	6.15	5.29	5.27	4.37
June 2016	0.81	1.20	1.08	0.79

Spectra of the total force over the length of the cylinder are shown in Figure 6.13. The subscript M relates to the force estimate based on the Morison equation (3.6), subscript D denotes the estimate based on linear diffraction theory (3.20), and subscripts S and N refer to forces calculated through integration of the total surface pressure obtained numerically using slip and no-slip cylinder wall boundary conditions, respectively.

The C_d and C_m coefficients only changed minimally across the seasons. The low value of C_d shows that the drag term in the Morison equation provided a minimal contribution to the total force. This implies that diffraction theory is acceptable at providing force estimates for a typical large-diameter monopile in the southern North Sea. However, it should be noted that linear diffraction theory obviously omits the effects of steep, large-amplitude waves and high frequency diffracted waves.
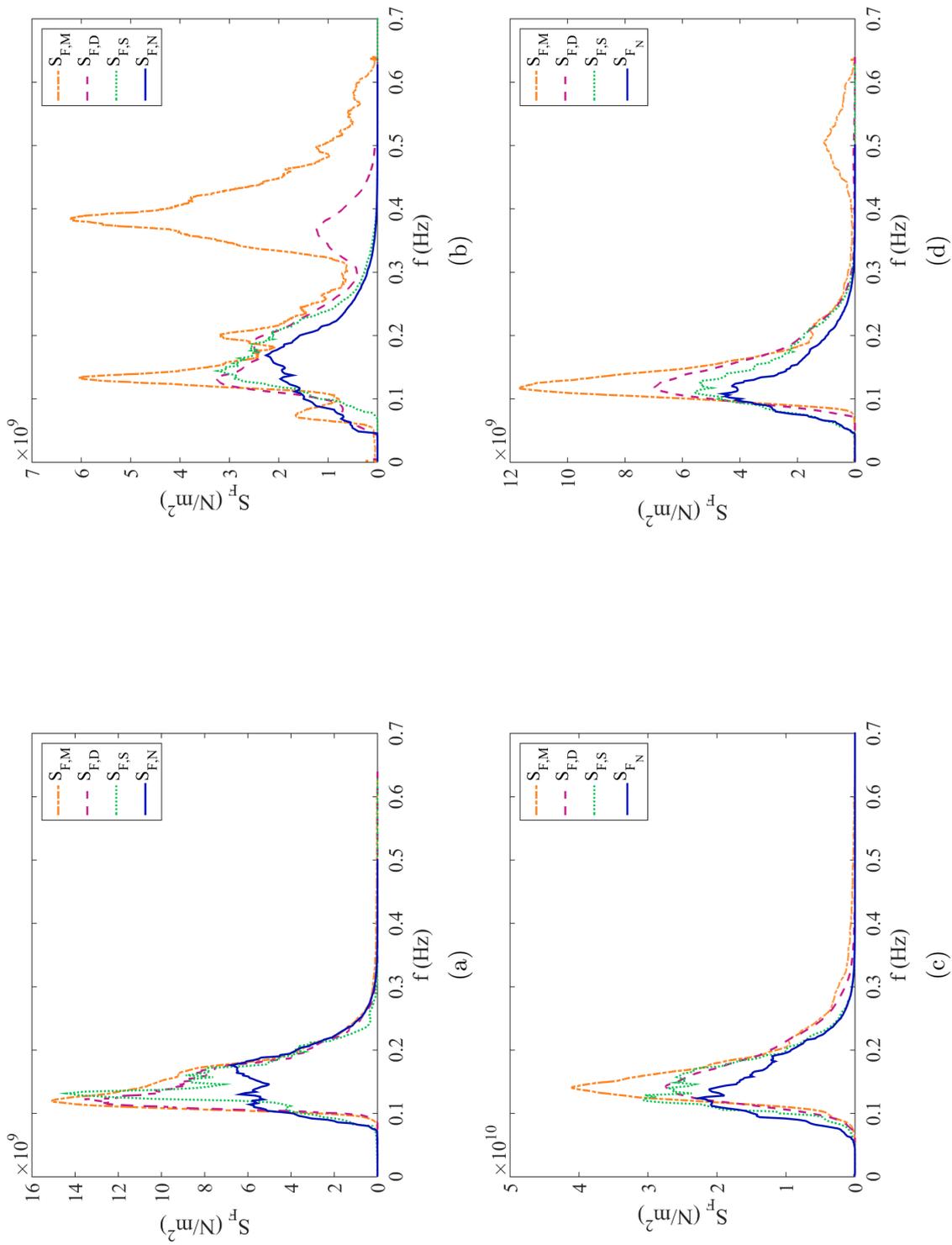
Figure 6.13: Total in-line wave force spectra for waves during (a) Autumn, (b) Winter, (c) Spring and (d) Summer at Teesside Offshore Wind Farm in the southern North Sea.

In all the wave, velocity, and force spectra considered, the modal wave period remained nearly constant throughout the year, with the exception of the bimodal sea state in December 2015 (and, to a lesser degree, June 2015). The OpenFOAM numerical spectra agree well with their analytical counterparts for the unidirectional sea states in September 2015, March 2016, and June 2016, but match less well in December 2015 (where the higher frequency force components are not apparent in the numerical spectrum, unlike the analytical spectrum). Numerical predictions obtained using slip and no-slip boundary conditions are generally similar over the range of cases considered, although the no-slip results show a small reduction in energy and diffracted wave field values due to viscous surface effects.

The results for the December 2015 dataset were unsatisfactory in comparison to the other three data sets, where the spectral shape of the numerically modelled surface elevation matches well with the measured wave data. It was hypothesised that complications arising from the December 2015 data set were due to the significant contribution of high-frequency waves, leading to a defined high-frequency peak.

As a consequence of efforts described previously to reduce the computational overhead, it is conceivable that the high-frequency waves within the regime were under-sampled in the wave direction. When constructing the mesh for the December 2015 data set, a compromise was made to sample the high-frequency waves with a minimum of 6 cells, far fewer than the minimum number of cells per wave for the unimodal distributions. However, it was recognised that simply increasing the number of cells per wave for the higher-frequency waves would greatly increase the computational overhead when both modal wave periods were included in

a single simulation, as the computational domain length must be specified by the larger modal wave period.

A further difficulty in simulating the December 2015 wave field was attributed to the small wave height, where values on the y-axis in figure 6.10a are much lower than those for the other three data sets. The mesh resolution in the vertical direction might therefore require increased refinement at the free surface.

In an attempt to successfully capture the second peak, significant efforts were made to improve the mesh resolution for the December 2015 data set. In the first effort, the cell length in the wave direction was divided in half to allow the shortest waves within the spectrum to be sampled by a minimum of 14 cells per wave in the wave direction. This mesh resolution also meant that the longest waves now contained approximately 180 cells in the wave direction. The mesh size was increased by approximately 70%, from 3.5M cells to 5.8M cells, significantly increasing computational overhead. A negligible improvement was seen in the results. The increase in computational overhead was not acceptable given the minimal changes in the results, and it was determined that increasing the cells in the wave direction did not affect the overall results enough to update the results. Only the slip boundary condition was tested for these simulations. Figure 6.15a presents the results from the increased mesh resolution in the wave direction.

A further two attempts were then made to improve the results by increasing the mesh resolution at the free surface. The first attempt aimed to apply a minimum of 8 cells per wave height. Again, the major issue was to increase the mesh resolution whilst maintaining acceptable mesh non-orthogonality and aspect ratio. An increase in the number of cells
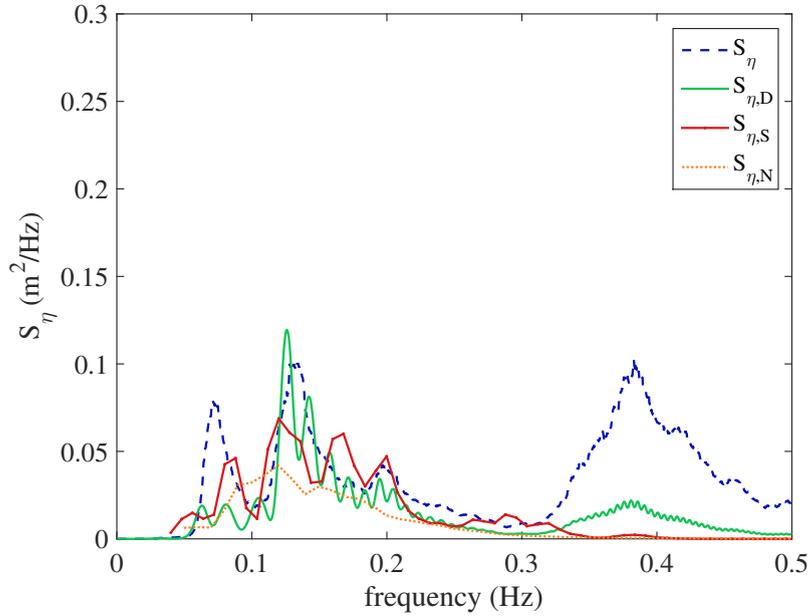
Figure 6.14: Surface elevation wave spectral density functions using increased cell density in the wave direction for the raw surface displacement data, S_η, diffracted wave spectrum $S_{\eta,D}$ and numerical wave spectrum with a slip boundary condition, $S_{\eta,S}$.

required a small increase in the wave direction as well to avoid deformed cells at the free surface. The increase in cell number was again significant and the mesh size for this simulation was 6.2M, greatly increasing the computational time.

This simulation did not offer enough improvement to the results and a final attempt was made to further refine the free surface mesh. The last attempt employed a minimum of 16 cells at the free surface, again attempting to increase the resolution in the vertical direction whilst attempting to preserve the mesh quality. Difficulties in maintaining an acceptable mesh through the quality checks meant that the mesh size reached approximately 14.4M cells, and the simulation time increased accordingly.

Results from this attempt were worse than previous attempts and it

is expected that the mesh density and quality introduced additional numerical errors and the individual frequencies within the lower-frequency waves were no longer visible. Figure 6.15 presents the results from these further two attempts to capture the high-frequency peak.
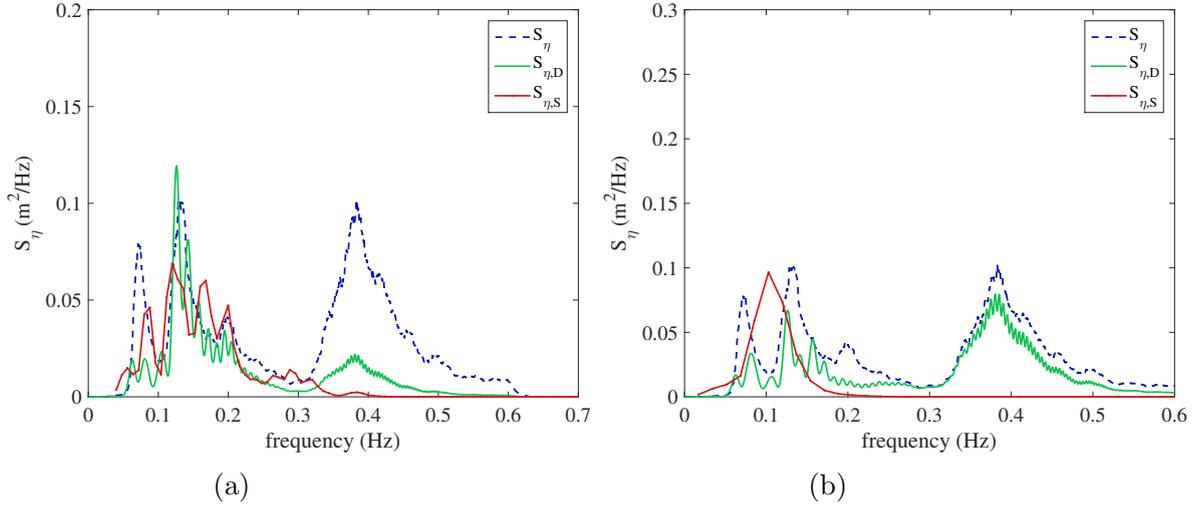
Figure 6.15: Surface elevation wave spectral density functions with (a) minimum 8 cells per wave height and (b) minimum 16 cells per wave height for the raw surface displacement data, S_η, diffracted wave spectrum $S_{\eta,D}$ and numerical wave spectrum with a slip boundary condition, $S_{\eta,S}$.

The results were again unsatisfactory and the poorer mesh aspect ratio likely introduced additional numerical errors. It is recommended that this is explored further in the future as a final determination on the suitability of OpenFOAM for capturing bimodal spectra has not been demonstrated here.

OpenFOAM behaves well for modelling waves with a unimodal distribution and models the wave field for the Autumn 2015 and Spring 2016 data sets very well, and also models the Summer 2016 data set with acceptable accuracy, although improvements can be made here as well to model the waves within the small high-frequency peak. The OpenFOAM model also captures the low-frequency waves within the December 2015

146

wave field.

6.6   Conclusions

OpenFOAM, Waves2Foam, and the input boundary condition *custom-Spectrum* were used to simulate the free surface time series for irregular unidirectional waves, based on *in situ* data from Teesside Offshore Wind Farm. Numerical and analytical predictions were compared against the *in situ* data through statistical and spectral analyses of the free surface elevation and velocity component time series. Four data sets, each of length 24 hours and corresponding to a different season of the year, at a sampling frequency $F_s = 1.28$ Hz during 2015/2016, were used to calibrate the input boundary condition. Following conversion of the wave buoy displacement time-series data from cm to m, a FFT was applied over a range of frequencies and the wave spectrum for each relevant value was calculated and smoothed with an MA filter (see Section 2.3). Total energy within the spectrum was then found through integration. From (2.32), the amplitude values for each frequency bin were calculated and used to determine the sea state at the boundary.

The analytically calculated sea state was compared statistically to the wave buoy data using (2.30). The sea state and statistical information has been presented for the following datasets:

1. Raw data set composed of the wave buoy displacement (η_{raw} time series and $S_{\eta,Raw}$) spectrum,

2. Analytical data set from equations (2.33)-(2.35) for calculation of the 2D undisturbed velocity components

3. Numerical data set from OpenFOAM predictions of the undisturbed η_{OF} time series, and $S_{\eta,OF}$, $S_{Ux,OF}$ and $S_{Uz,OF}$),

4. Comparison of analytical and numerical predictions for the local hydrodynamic wave field and incident wave force on a turbine monopile in the southern North Sea at Teesside Offshore Wind Farm.

It was found that, using *customSpectrum*, the simulations in Open-FOAM were capable of capturing the undisturbed significant wave height to within 10% of the raw displacement data (with the lowest percentage difference of 3.20% for the December significant wave height). The diffracted significant wave height was computed analytically and numerically and the results compared. The diffracted significant wave height $H_{s,D}$ showed a reduction from the undisturbed wave height $H_{s,\infty}$, effect was similarly seen in the numerical results. This is in broad agreement with Goda (1985) who found that an irregular wave diffraction solution should have a lower diffracted wave height than might be expected from a regular diffraction solution. Both numerical results using slip and no-slip boundary conditions displayed this reduction in wave height around the monopile as compared to the undisturbed wave elevation spectrum. The no-slip boundary condition showed a greater decrease in wave height due to the effect of viscosity on the cylinder wall.

Comparison tests undertaken using observed sea states for all four seasons at Teesside Offshore Wind Farm demonstrated satisfactory agreement between the linear diffraction theory and OpenFOAM estimates of wave, water particle velocity component, and force spectra for three of the datasets. The results were in relatively poor agreement for the De-

148

cember dataset corresponding to a bimodal wave distribution. Although significant efforts were made to improve the results for this dataset, further investigation is required and is beyond the scope of this work.

Despite difficulties modelling the wave field found in December 2015, OpenFOAM provides a good method for modelling a unimodal distribution, evidenced by the models of the wave fields from the autumn, spring and summer data sets. The numerical predictions of the diffracted wave field agree with the shape of the diffracted wave field formulated analytically, where energy due to waves at the individual frequencies are visible. OpenFOAM produces better results for the low-frequency waves in the vicinity of the cylinder than for the high-frequency waves. It was found that the results from the numerical model were minimally affected by the choice of slip or no-slip cylinder wall boundary condition.

The foregoing results confirm that the combination of *customSpectrum* and OpenFOAM provides reasonably accurate simulations of the sea state found at Teesside Offshore Wind Farm. The use of linear diffraction theory and CFD has been considered for determining the free surface elevation η, significant wave height H_s, and water particle velocity components u and w close to a surface-piercing vertical cylinder representative of an offshore wind turbine monopile situated in the southern North Sea. The total in-line force on the monopile has also been determined. Linear diffraction theory is fast to implement, but neglects nonlinearity and viscous effects. The CFD model is based on OpenFOAM and is expensive in terms of computational resources, but could resolve nonlinear and viscous effects. It should be noted that OpenFOAM was run using a constant value of kinematic fluid viscosity, which meant that the model was essentially laminar.

Chapter 7

Conclusions and
Recommendations

7.1 Preamble

As one of the fastest growing sources of marine renewable energy, off-
shore wind power has the potential for substantially increased output
from non-emitting sources. However, drawbacks in the development of
offshore wind power lie, to a large extent, in the high costs of operations
and maintenance (O&M). Increased costs are exacerbated by the marine
location of the turbines, with access to the turbines for maintenance be-
ing strongly dependent on weather and sea state conditions. Safe access
to offshore wind turbines for repair workers is a prerequisite for effective
repair and maintenance activities, which is vital in reducing the O&M
costs.

For monopile turbines, the crew transfer vessels used to transport re-
pair workers to offshore wind turbines must remain steady whilst abutted
against the support column for the duration of crew transfer. Unexpected
wave motion in the vicinity of the support column can disrupt the fric-

tional contact between the vessel fender and the transition piece on the turbine. If wave hydrodynamics overcome the frictional force, the vessel can slip away from the monopile, potentially endangering repair workers in transfer.

Advances in knowledge of the hydrodynamic wave field around an offshore wind turbine in any unidirectional sea state should allow forecasts to be made of vessel motion under operating conditions. Thus, the scope of this PhD research was to formulate a method for approximating the local hydrodynamic irregular wave field interacting with turbine monopiles, and subsequently provide the diffracted wave kinematics and incident wave force on the monopile, both of which affect vessel motion.

Underlying mathematical equations describing wave motion were presented, along with a discussion of ocean wave statistics and a methodology for obtaining time-dependent wave kinematics from a stationary sea state in the frequency domain. Methods were introduced for determining the in-line wave force incident on fixed small-diameter and large-diameter surface-piercing cylinders in waves; these included the formulation of equations for monochromatic and irregular wave fields. Details were also given of the numerical model that constituted the CFD package, OpenFOAM.

The numerical model was first verified through analysis of a steady current interacting with a surface piercing cylinder. Non-dimensional drag and inertia force coefficients, C_d and C_m, were determined from the numerical model for four different Re values and compared to experimental values to validate the numerical model. Simulations were run for $Re = 40$, 300, 3900 and 1×10^5 and the visualisations produced were compared to previous experimental and numerical results. The vortex

development and shedding patterns that were expected with increasing Re values were apparent in the numerical models.

Following verification of the numerical model for a steady unidirectional current interacting with a surface-piercing cylinder, OpenFOAM was employed to simulate numerically a linear wave field. The simulated wave parameters and cylinder diameter were chosen to represent expected wave periods at Teesside Offshore Wind Farm.

Waves2Foam, which includes an extension to the *interFoam* solver (included in the OpenFOAM release), called *waveFoam*, was used to generate simulated waves. Numerical model predictions were then compared to the analytical solution of monochromatic, regular waves, and excellent agreement was achieved regarding the free surface motion. Waves of four different wave periods (and corresponding wavelengths) were simulated interacting with a cylinder of constant diameter in order to explore different fluid-structure interaction effects and the influence due to diffraction.

Finally, the aforementioned linear wave theory was applied to an irregular sea state, according to measured *in situ* data from Teesside Offshore Wind Farm. The *customSpectrum* boundary condition developed as part of the present work allowed wave spectrum values to be input directly into the OpenFOAM solver, with each individual wave amplitude component calculated at the boundary.

From the spectral amplitude values, and the assumption of small-amplitude linear waves, superposition allowed the initial in-line velocity component u and vertical velocity component w to be directly evaluated at all control volume faces on the boundary. *customSpectrum* simulates the sea state from wave spectra determined for site observations of waves at the Teesside wind farm location, supplied by the operations team at

EDF Energy Renewables.

Numerically generated undisturbed waves were validated using analytical wave solutions for an irregular sea state. Statistical analysis of the free surface elevation and velocity components provided a reliable comparison between the raw *in situ* data, analytically calculated sea state, and the numerically generated sea state. Comparing the area under the spectral curve m_0 with the variance of the data σ^2 confirmed that stationary spectra represented the data time-series. The m_0 values for all spectra were found to agree closely with σ^2, confirming that *customSpectrum* gave a proper representation of sea states at the Teesside site.

The verified sea state was then used as the input condition for analysis (numerically and analytically) of ocean wave interaction with a surface-piercing fixed vertical cylinder, representing a wind turbine monopile support column. Wave forces incident on the cylinder were calculated through integration per unit length of the numerically simulated wave surface pressure and analytically using the diffraction formulation introduced by MacCamy and Fuchs (1954), and the Morison equation (Morison et al., 1950).

The non-dimensional force coefficients C_d and C_m required by the Morison equation were calculated using the method introduced by Wang (1968), discussed in Section 3.2.1. This method is appropriate when considering large Reynolds number values and low Keulegan-Carpenter number values, for which the fluid-structure interaction lies in the drag-inertia regime. Within this regime, it is very difficult to determine the force coefficient C_d because the flow experiences a "drag crisis", whereby the drag coefficient rapidly decreases when the Reynolds number increases to $Re \approx 1 \times 10^5$, before increasing again at $Re \approx 1 \times 10^6$.

Table 6.7 showed that the Reynolds number value of interest lies within or just beyond the drag crisis regime. Values for C_d and C_m calculated through the method presented by Wang (1968) appeared to give satisfactory results for the Morison force calculation. Although the Morison equation resulted in a larger estimate of the total force value in comparison to the diffraction solution, both calculation methods resulted in the same spectral shape.

The method introduced by Borgman (1965) for determining the force spectrum at a specific location on a cylinder provided an additional method for verifying that the correct spectral force shape was produced. It was seen that the force spectral shapes correlated closely with the shape of the surface elevation spectra, in agreement with previous observations of this phenomenon (see e.g. Wiegel et al. (1959)).

To calculate the irregular sea diffracted hydrodynamics and in-line wave force, it was assumed that the diffracted wave height in an irregular small-amplitude wave field could be derived from the superposition of the diffracted wave solution obtained for each individual wave component. The frequencies of radially outward-moving diffracted irregular waves corresponded to frequencies of incident waves, also seen in (Swan and Sheikh, 2014). By applying superposition, the linear irregular diffracted surface elevation was calculated analytically, neglecting viscous surface effects. The diffracted wave spectrum was then derived from the FFT of the diffracted surface elevation. From the diffracted wave spectrum, the resulting horizontal and vertical diffracted velocity components were computed.

Variances of the diffracted analytical values for η, u, w and the wave force were then compared to their numerically predicted counterparts,

obtained using OpenFOAM. Numerical values were obtained at selected positions in the flow domain using utilities such as numerical wave gauges and probes for measuring the values at specific points within the computational domain.

Through this method, the diffracted significant wave height $H_{s,D}$ was obtained from the diffracted wave spectrum, $S_{\eta,D}$. The linear diffraction analytical solutions were in good agreement with the numerical results using the fully nonlinear OpenFOAM model, provided a slip boundary condition was applied at the cylinder wall.

It was found that the numerical model was capable of generating a unidirectional wave field with the same frequency distribution found at Teesside Offshore Wind Farm, and analytical linear diffraction formulations provided satisfactory initial estimates for the diffracted wave elevation and velocity components, when compared to the numerical results. The numerical model behaved well for three out of the four data sets, where the most significant contribution to the total energy was within the lower-frequency waves. The numerical model behaved less well when there was a bimodal distribution and both high-frequency and low-frequency waves contributed considerably to the overall energy within the system.

7.2   Conclusions

The model showed that the measured sea state could be approximated satisfactorily using OpenFOAM coupled with the *customSpectrum* boundary condition implemented in the Waves2Foam package. A statistical analysis of the spectral distribution of the surface elevation obtained from

a single wave buoy was performed prior to numerical simulation. The variance of the data was shown to be equal to the zeroth-moment m_0. The distribution at Teesside Offshore Wind Farm was seen to change from a unimodal distribution for two data sets (September 2015 and March 2016) to a bimodal distribution for December 2015 and, to a lesser degree, June 2016.

Through superposition of linear waves with amplitudes a_n obtained from the spectral distribution, the sea state was formulated analytically, providing predictions for the horizontal and vertical velocity components relevant to wave loading. By comparison of the spectral shape of the surface elevation and 2-D velocity components, numerically generated waves using the *customSpectrum* inlet boundary condition were seen to show good agreement with the analytically established sea state.

In an open numerical wave tank with no monopile present, the numerically predicted significant wave height was within 5% of the significant wave height obtained from the wave buoy data spectral distribution for the September 2015, December 2015 and March 2016 data sets. The largest discrepancy was seen in the June 2016 data set, where the numerical significant wave height was 10% lower than the significant wave height from the wave buoy data. The agreement in the shape of the spectral distribution of the 2-D analytically formulated and numerically predicted velocity components also demonstrated the success of the numerical model in reproducing the desired sea state.

A slight reduction in the mesh density for the shorter wave periods present in the December 2015 bimodal distribution was allowed in order to lessen the computational overhead. However, this produced unsatisfactory results and three additional attempts were made to improve the

numerical model by increasing the mesh resolution first in the horizontal direction and then in the vertical direction. The immense increase in computational overhead did not warrant the trivial improvements in the results, and more work is required here to determine the suitability of OpenFOAM for capturing bimodal wave distributions. However, it can be noted that the OpenFOAM model does behave relatively well for waves at the low-frequencies within the December 2015 data set.

The numerical prediction and analytical formulation of the irregular wave field then allowed for several methods for calculating the wave loading to be employed. The Morison equation, which is the sum of the time-dependent in-line wave force along the submerged length of the cylinder, was determined analytically using seasonal irregular horizontal velocity and acceleration components. The Morison equation is appropriate for small-diameter cylinder where viscous forces are present, which is also modelled by the no-slip wall condition used for comparison in the numerical predictions. The spectral distribution of the Morison force at height $z = $ -1.5 m for each season agreed with the spectral force calculated at the same height presented by Borgman (1965).

The large-diameter analytical diffraction solution, which provided values for the diffracted surface elevation, horizontal and vertical diffracted velocity components and wave force due to diffraction, was formulated for the local sea state at Teesside Offshore Wind Farm. In addition to the no-slip condition used in some simulations, simulations were also undergone in which a slip condition was applied on the cylinder wall. The dominating inertial conditions of the slip condition should agree with those assumed in the linear diffraction formulation. Wave loading comparisons were again made in the frequency domain, where the spectral

distribution was obtained for each wave loading time-series calculation.

It was seen that the spectral distribution of the wave loading was of a similar shape to the surface elevation spectral distribution. The Morison equation gave higher estimates of force loading for 75% of the data sets than what was seen either through the diffraction formulation or the numerical prediction. Simulations in which a slip wall condition on the cylinder was used showed better agreement with the linear diffraction formulation than those where a no-slip wall condition was used. Despite some variation between the analytically and numerically predicted values of surface elevation, velocity components and wave force, the analytical solution appeared to provide a good basis approximation of the wave field in the vicinity of the turbine monopile. Numerical methods can provide more accurate predictions of a particular sea state interacting with a turbine monopile, and can consider nonlinear and viscous terms within the wave field that are neglected in the analytical solutions.

Analytical solutions, which are fast to implement in comparison to numerical solutions, provided good approximations to the wave motions relevant to vessel responses, such as the water particle velocity and acceleration components within the region. Although the model was designed for unidirectional seas, some success was achieved in simulating seas driven by bimodal wave spectra. However, despite the appearance of a second peak in the undisturbed numerical wave spectra, it should be emphasised that the accuracy of the model was, of course, greatly diminished for multi-directional or crossing seas that can results in a bimodal spectral distribution.

7.3 Recommendations for future research

7.3.1 Wave Directionality

The present analysis has assumed that the sea state is unidirectional. However, historical weather data in the region of interest indicate that the sea state is most likely to be multi-directional and subject to crossing seas. The close proximity to the shore (1.5 km) and shallowness of the offshore wind farm site (15 m) could exacerbate changes in the modal distribution, when external storm swells interact with the local sea state. Historical statistical weather data in the southern North Sea near the Teesside offshore wind farm site indicate a modal wave period in the range of $4 \text{ s} \lesssim T_p \lesssim 14 \text{ s}$, which corresponds to $25 \text{ m} \lesssim \lambda_p \lesssim 160 \text{ m}$, and a wind direction predominantly in the southwest direction in March and September, whereas the June data exhibit a larger spread in the northeast direction. The December data exhibit a more southerly dominated wind direction [1], the direction change accounting for the second peak in the spectrum. Guedes Soares (1984) found that bimodal spectra occur 5-40% of the time in the North Sea.

A better representation of the local sea state would therefore be to use a pair of directional spreading functions, one for each modality, to improve the accuracy of the computational model. However, data for this thesis were only available for a single wave buoy at one location, greatly limiting the degree to which directionality could be determined (McAllister et al., 2017). Whilst inclusion of directionality is beyond the scope of the present research project, a multidirectional model that can resolve the prevailing wind-wave-swell directions from single point wave

---

[1]see https://www.windfinder.com/windstatistics/Teesside

159

observations (see e.g. Adcock and Taylor (2009)) could be developed to improve the model.

It is thus recommended that future work be conducted to extend the model so that it can account for multidirectional, crossing sea states by including additional spreading functions or improving the approach to the numerical simulation. Inclusion of a spreading function would be best achieved by gathering *in situ* data at several locations simultaneously. Additionally, the values presented here are the results from a single year of data only; improvements could be made from a longer data sample, thereby taking into account climate affects that can occur over years rather than months.

A final suggestion to improve the numerical model in OpenFOAM to better capture the bimodal distribution could approach the waves within each peak separately. In this case, two separate simulations with two computational domains could be run for the same sea state where one simulation is based on the higher-frequency waves and the second focuses on the lower-frequency waves. Following the two separate simulations, the overall results could be combined into a single spectra, which should demonstrate the bimodal distribution.

7.3.2 Nonlinear and higher order diffraction effects

Other simplifications made in this research arose from the use of linear theories for calculating the diffraction effects. It is recommended that a higher-order diffraction method should be pursued in the future to predict the effect of wave nonlinearity (see e.g. Chau and Eatock Taylor (1992)), which is obviously important for vessel motions in the vicinity of the monopile.

Although the analytical solution and the numerical solution showed the same patterns of a decrease in diffracted wave height and wave particle kinematics in the vicinity of the monopile, inclusion of higher order terms in the diffraction formulation could reveal non-negligible higher harmonics. It is relevant to note that Stansberg and Kristiansen (2005) found that even for small-amplitude waves, linear diffraction theory applied to an irregular wave field gave results that did not agree with experimental data and a second-order diffraction solution was required to improve the results.

7.3.3 Extending the results to crew transfer vessel motion

It is recommended that a future study be carried out to approximate crew transfer vessel motions based on the diffracted hydrodynamic wave behaviour in the present models. Crew transfer vessel motion can be computed using a standard 2D vessel-motion method, such as strip theory, where it is assumed that the vessel displacement varies linearly with the diffracted wave velocities and accelerations (Journee and Pinkster, 2002). Conducting this work would require additional experimental or *in situ* data whereby the actual vessel motion under operating conditions could be monitored.

Furthermore, the transfer function derivation discussed in Section 3.3 could aid in the application of control theory, where it is assumed that the output ship motion is directly related to the input hydrodynamics. The transfer function, based on an input wave spectrum, could be applied to predict the diffracted wave spectrum, from which wave velocities and accelerations could be forecast for a larger spread of possible sea

161

states in the region. Use of control theory, perhaps coupled to machine learning for predicting the data for input sea states, could help better ship manoeuvring to be accomplished.

7.4   Final Observations

The methods presented here for determining the water particle kinematics close to a wind turbine support monopile from a wave spectrum should be useful in determining typical wave motions incident on a vessel, which ultimately helps vessel operators gain better control of the vessel, leading to safer crew transfer.

The numerical results demonstrated the capabilities of OpenFOAM in reproducing *in situ* wave conditions for a unidirectional sea state. The analytical results, which can be calculated relatively quickly with the formulation presented herein, also provided an in-depth understanding of the likely hydrodynamic field expected at the offshore wind farm site and at the monopile itself.

Engineers can benefit greatly by computing accurate site-specific actual wave conditions, rather than relying on parametric representations of the wave conditions. It is also beneficial to note the change between unimodal and bimodal spectra that occurs at the wind farm location throughout the year. Furthermore, use of a parametric representation of the sea state means that the adjustment between unimodal and bimodal spectra that occurs in the region would remain neglected.

Improved accuracy of significant wave height values at an offshore

wind farm is crucial to crew transfer vessel operators who rely solely on such information to determine the feasibility of accessing the turbines for repairs. Assembling a database of simulated sea states based on additional data collected at the offshore wind farm site could improve the calibration of *customSpectrum* and thus provide the input for more realistic simulation of vessel motion for a wider range of sea states.

With an enhanced knowledge of the hydrodynamics affecting crew transfer vessel motion and seasonal sea state data specific to an offshore wind farm location, improvements can be made to vessel motion algorithms. Additional information beyond the statistical significant wave height value may provide vessel operators with a greater opportunity to avoid dangerous conditions when approaching the turbine monopile and reduce economic losses due to incomplete repairs. The methodology presented here has great potential to help cut the overall O & M costs associated with offshore wind farms.

References

G. Kieffer and T. D. Couture. Renewable energy target setting. Technical report, International Renewable Energy Agency (IRENA), June 2015.

J. L. Sawin, F. Sverrisson, and W. Rickerson. Renewables 2015 - global status report. Technical report, Ren21, 2015.

C. Small and R. T. Nicholls. A global analysis of human settlement in coastal zones. *Journal of Coastal Research*, 19(3):584–599, Summer 2003.

I. Pineda. The European offshore wind industry - key trends and statistics 2015. Technical report, European Wind Energy Association (EWEA), 2016.

GWEC. Offshore wind. Technical report, Global Wind Energy Council (GWEC), 2016. URL `www.gwec.net/wp-content/uploads/2016/05/Global-offshore-1.pdf`.

L. Hong and B. Möller. Feasibility study of China's offshore wind target by 2020. *Energy*, 48(1):268–277, December 2012.

W. Krewitt, K. Nienhaus, C. Klessmann, C. Capone, E. Stricker, and W. Graus. Role and potential of renewable energy and energy efficiency for global energy supply. Technical Report (UBA-FB) 001323/E, Dessau-Rosslau: Federal Environment Agency (Umweltbundesamt), December 2009.

S. B. Capps and C. S. Zender. Estimated global ocean wind power potential from QuikSCAT observations, accounting for turbine characteristics and siting. *Journal of Geophysical Research*, 115, 2010.

M. Taylor, P. Ralon, and A. Ilas. The power to change: Solar and wind cost reduction potential to 2025. Technical report, International Renewable Energy Agency (IRENA), June 2016.

G. Corbetta, I. Pineda, and J. Moccia. The European offshore wind industry - key trends and statistics 2013. Technical report, European Wind Energy Association, 2014.

I. B. Sperstad, E. E. Halvorsen-Weare, M. Hoffman, L. M. Nonas, M. Stalhane, and M. Wu. A comparison of single- and multi-parameter wave criteria for accessing wind turbines in strategic maintenance and logistics models for offshore wind farms. In *EERA DeepWind' 2014, 11th Deep Sea Offshore Wind R&D Conference*, volume 53, pages 221–230, 2014.

S.-P. Breton and G. Moe. Status, plans and technologies for offshore wind turbines in Europe and North America. *Renewable Energy*, 34 (3):646–654, 2009.

G. J. W. van Bussel, A. R. Henderson, C. A. Morgen, B. Smith, R. Barthelmie, and K. Argyriadis. State of the art and technology trends for offshore wind energy: Operation and maintenance issues. In *Proceedings of offshore wind energy special topic conference*, Brussels, Belgium, December 2001.

S. Kostecki. Random vortex method in numerical analysis of 2D flow around circular cylinder. *Studia Geotechnica et Mechanica*, 36:57–63, 2014.

Y. Dalgic, I. Lazakis, and O. Turan. Investigation of optimum crew transfer vessel fleet for offshore wind farm maintenance operations. *Wind Engineering*, 39(1):31–52, 2015a.

B. Maples, G. Saur, M. Hand, R. van der Pietermann, and T. Obdam. Maintenance strategies to reduce the cost of offshore wind energy installation. Technical report, National Renewable Energies Laboratory (NREL), 2013.

V. Baagøe-Engels and J. Stentoft. Operations and maintenance issues in the offshore wind energy section: An explorative study. *International Journal of Energy Sector Management*, 10(2):245–265, 2016.

J. Browell, I. Dinwoodie, and D. McMillan. Forecasting for day-ahead offshore maintenance scheduling under uncertainty. In *European Safety and Reliability Conference*, 2016.

J. J. Nielsen and J. D. Sorensen. On risk-based operation and maintenance of offshore wind turbine components. *Reliability Engineering and System Safety*, 96:218–229, 2011.

M. Scheu, D. Matha, M. Hofmann, and M. Muskulus. Maintenance strategies for large offshore wind farms. *Energy Procedia*, 24:281–288, 2012.

R. Auckland and R. Garlick. Wind farm service vessels (WFSVs) - an analysis of supply and demand. Technical report, 4COffshore, 2015.

E. E. Halvorsen-Weare, C. Gundegjerde, I. B. Halvorsen, L. M. Hvattum, and Lars Magne Nonås. Vessel fleet analysis for maintenance operations at offshore wind farms. *Energy Procedia*, 35:167–176, January 2013.

M. Hoffman. A review of decision support models for offshore wind farms with an emphasis on operation and maintenance strategies. *Wind Energy*, 35(1):1–16, 2011.

IEA. Technology roadmap - wind energy. Technical report, International Energy Agency (IEA), Paris, 2013.

L.F. Chen, J. Zang, A. J. Hillis, G. C. J. Morgan, and A. R. Plummer. Numerical investigation of wave-structure interaction using OpenFOAM. *Ocean Engineering*, 88:91–109, 2014.

P. Agarwal and L. Manuel. Incorporating irregular nonlinear waves in coupled simulation and reliability studies of offshore wind turbines. *Applied Ocean Research*, 33:215–227, 2011.

W. Finnegan and J. Goggins. Numerical simulation of linear water waves and wave-structure interaction. *Ocean Engineering*, 43:23–31, 2012.

T. Josse, A. Billet, and S. B. Leen. Prediction of supply vessel motion during transfer to a fixed structure. In *Proceedings of the 30th International Conference on Ocean, Offshore and Arctic Engineering*, June 2011.

M. König, D. Ferreira Gonzalez, M. Abdel-Maksoud, and A. Düster. Numerical investigation of the landing manoeuvre of a crew transfer vessel to an offshore wind turbine. *Ships and Offshore Structures*, 12, 2017.

J. R. Morison, M. P. O'Brien, J. W Johnson, and S. A. Schaaf. The force exerted by surface waves on piles. *Journal of Petroleum Technology*, 189:149–154, 1950.

R. C. MacCamy and R. A. Fuchs. Wave forces on piles: a diffraction theory. Technical Report 69, U.S. Army Beach Erosion Board Technical Memo, 1954.

J. Feuchtwang and D. Infield. Offshore wind turbine maintenance access: a closed-form probablistic method for calculating delays caused by seastate. *Wind Energy*, 16:1049–1066, 2012.

Y. Dalgic, I. Lazkis, I. Dinwoodie, D. McMillan, and M. Revie. Advanced logistics planning for offshore wind farm operation and maintenance activities. *Ocean Engineering*, 101:211–226, 2015b.

O. M. Faltinsen. *Sea Loads on Ships and Offshore Structures*. Cambridge University Press, 1990.

T. Sarpkaya. Force on a circular cylinder in viscous oscillatory flow at low Keulegan-Carpenter numbers. *Journal of Fluid Mechanics*, 165: 61–71, 1986.

R. G. Dean and R. A. Dalrymple. *Water Wave Mechanics for Engineers and Scientists*, volume 2. World Scientific Publishing Co. Pte. Ltd., Covent Garden, London WC2H 9HE, 1991.

T. Sarpkaya and M. Isaacson. *Mechanics of wave forces on offshore structures*. Van Nostrand Reinhold Co., 1981.

M. L. McAllister, V. Venugopal, and A. G. L. Borthwick. Wave directional spreading from point field measurements. *Proceedings of the Royal Society A*, 473:20160781, 2017.

S. K. Chakrabarti. *Hydrodynamics of Offshore Structures*. Springer-Verlag, 1987.

W. J. Pierson and L. Moskowitz. A proposed spectral form for fully developed wind seas based on the similarity theory of S. A. Kitaigorodskii. *Journal of Geophysical Research*, 69:5181–5190, 1964.

K. Hasselmann, T. P. Barnett, E. Bouws, H. Carlson, D. E. Cartwright, K. Enke, J. A. Ewing, H. Gienapp, D. E. Hasselmann, P. Kruseman, A. Meerburg, P. Miller, D. J. Olbers, K. Richter, W. Sell, and H. Walden. Measurements of wind-wave growth and swell decay during the Joint North Sea Wave Project (JONSWAP). *Ergnzungsheft zur Deutschen Hydrographischen Zeitschrift Reihe*, 8(12):95, 1973.

C. L. Bretschneider. Wave variability and wave spectra for wind-generated gravity waves. Technical Memorandum 118, Beach Erosion Board, U.S. Army Corps of Engineers, Washington D.C., USA, 1959.

A. Papoulis. *Probability, Random Variables, and Stochastic Processes*. McGraw-Hill, Inc., United States, 3rd edition, 1991.

B. M. Sumer and J. Fredsøe. *Advanced Series on Ocean Engineering - Hydrodynamics Around Cylinderical Structures*, volume 26. World Scientific Publishing Co. Pte. Ltd., 2006.

Y. Goda. *Random Seas and Design of Maritime Structures*. The University of Tokyo Press, Tokyo, Japan, 1985.

S. A. Hughes and E. F. Thompson. Coastal engineering technical note: Directional wave spectrum using cosine-squared and cosine 2s spreading functions. Technical report, U.S. Army Engineer Waterways Experiment Station, 1986.

T. A. A. Adcock and P. H. Taylor. Estimating ocean wave directional spreading from an Eulerian surface elevation time history. *Proceedings of the Royal Society A*, 465:30833102, 2009.

V. Venugopal, J. Wolfram, and B. T. Linfoot. Wave kinematics factor in real and simulated storms. *Ocean Engineering*, 32:623–650, 2005.

C. Swan and R. Sheikh. The interaction between steep waves and a surface-piercing column. *Philosophical Transactions of the Royal Society A: Mathematical, Physical and Engineering Sciences*, 373(2033), 2014.

M. M. Zdravkovich. *Flow Around Circular Cylinders. Volume 1: Fundamentals*. OUP Oxford, 1997.

J. R. Chaplin. Hydrodynamic damping of a cylinder at $\beta \approx 10^6$. *Journal of Fluids and Structures*, 14:1101–1117, 2000. doi: doi:10.1006/jfls. 2000.0318.

L. Johanning, P. W. Bearman, and J. M. R. Graham. Hydrodynamic damping of a large scale surface piercing circular cylinder in planar oscillatory motion. *Journal of Fluids and Structures*, 15:891–908, 2001. doi: doi:10.1006/jfls.2001.0388.

T. Sarpkaya. Hydrodynamic damping. Technical Report Technical report No. NPS/TS-0406, Naval Postgraduate School, Monterey, CA 93943, 2006.

A. Roshko. Experiments on the flow past a circular cylinder at very high Reynolds numbers. *Journal of Fluid Mechanics*, 10:345–356, 1961.

P. W. Bearman, M. J. Downie, J. M. R. Graham, and E. D. Obasaju. Forces on cylinders in viscous oscillatory flow at low Keulegan-Carpenter number. *Journal of Fluid Mechanics*, 154:337–356, 1985.

H. Schlichting. *Boundary Layer Theory*. McGraw-Hill Book Co., New York, 1960.

C. Y. Wang. On high frequency oscillating viscous flows. *Journal of Fluid Mechanics*, 32:55–68, 1968.

T. Sarpkaya. Forces on cylinders near a plane boundary in a sinusoidally oscillating fluid. *Journal of Fluids Engineering*, 98:499–505, 1976.

H. Ishida and Y. Iwagaki. Wave forces induced by irregular waves on a vertical circular cylinder. *Coastal Engineering*, 16:2397–2414, 1978.

L. E. Borgman. The spectral density for ocean wave forces. In *Proceedings of the Special Conference on Coastal Engineering*, pages 147–182, 1965.

F. P. Chau and R. Eatock Taylor. Second-order wave diffraction by a vertical cylinder. *Journal of Fluid Mechanics*, 240:571–500, 1992.

Wayne A. Fuller. *Introduction to Statistical Time Series*. Wiley series in probability and statistics, 2nd edition, 1996.

H. K. Versteeg and W. Malalasekera. *An Introduction to Computational Fluid Dynamics: The finite volume method*. Pearson-Prentice Hall, 2007.

H. Jasak. Openfoam: Open source CFD in research and industry. *International Journal of Naval Architecture and Engineering*, 1:89–94, 2009.

P. Higuera, J. L. Lara, and I. J. Losada. Realistic wave generation and active wave absorption for Navier-Stokes models application to Open-FOAM. *Coastal Engineering*, 71:102–118, 2013.

D. A. Lysenko, I. S. Ertesvag, and K. E. Rian. Modeling of turbulent separated flows using OpenFOAM. *Computers and Fluids*, 80:408–422, 2013.

J. Davidson, M. Cathelain, L. Guillemet, T. Le Huec, and J. Ringwood. Implementation of an OpenFOAM numerical wave tank for wave energy experiements. In *Proceedings of the 11th European Wave and Tidal Energy Conference, 6-11th September*, Nantes, France, 2015.

J. H. Ferziger and M. Peric. *Computational Methods for Fluid Dynamics*. Springer-Verlag, 2002.

H. Rusche. *Computational Fluid Dynamics of Dispersed Two-Phase Flows at High Phase Fractions*. Phd thesis, Imperial College of Science, Technology & Medicine, 2002. URL http://powerlab.fsb.hr/ped/kturbo/OpenFOAM/docs/HenrikRuschePhD2002.pdf.

O. Ubbink and R. I. Issa. A method for capturing sharp fluid interfaces on arbitrary meshes. *Journal of Computational Physics*, 153(1):26–50, 1999.

N. G. Jacobsen, D. R. Fuhrman, and J. Fredsøe. A wave generation toolbox for the open-source CFD library: OpenFOAM. *International Journal for Numerical Methods in Fluids*, 70:1073–1088, 2011.

C. W. Hirt and B. D. Nichols. Volume of Fluid (VOF) method for the dynamics of free boundaries. *Journal of Computational Physics*, 39: 201–225, 1981.

H. G. Weller, G. Tabor, H. Jasak, and C. Fureby. A tensorial approach to computational continuum mechanics using object-oriented techniques. *Computers in Physics*, 12(6):620–631, November 1998.

H. Jasak. *Error Analysis and Estimation for the Finite Volume Method with Applications to Fluid Flows*. PhD thesis, Imperial College of Science, Technology and Medicine, London, 1996.

R. Courant, K. Friedrichs, and H. Lewy. On the partial difference equations of mathematical physics. *IBM Journal of Research and Development*, 11(2):215–234, 1967.

R. I. Issa. Solution of the implicitly discretized fluid flow equations by operator-splitting. *Journal of Computational Physics*, 62:40–65, 1985.

S. V. Patanker. *Numerical heat transfer and fluid flow*. McGraw-Hill, 1980.

B. van Leer. Towards the ultimate conservative difference scheme, V.A. second order sequel to Godunov's Method. *Journal of Computational Physics*, 87:408–463, 1979.

T. Sarpkaya. *Wave Forces on Offshore Structures*. Cambridge University Press, 2010.

C. Norberg. An experimental investigation of the flow around a circular cylinder: influence of aspect ratio. *Journal of Fluid Mechanics*, 258: 287–316, 1994.

ICHEC. Fionn, August 2018. URL `https://www.ichec.ie/about/infrastructure/fionn`.

C. J. Greenshields. *OpenFOAM - The Open Source CFD Toolbox v. 2.4.0 User guide*. OpenFOAM Foundation Ltd. & CFD Direct Ltd., 21st May 2015.

C. Geuzaine and J.-F. Remacle. Gmsh: a three-dimensional finite element mesh generator with built-in pre- and post-processing facilities. *International Journal for Numerical Methods in Engineering*, 79(11): 1309–1331, 2009.

M. Braza, P. Chassaing, and H. H. Minh. The numerical study and physical analysis of the pressure and velocity fields in the near wake of a circular cylinder. *Journal of Fluid Mechanics*, 165:79, 1986.

C. Wieselsberger. New data on the laws of fluid resistance. Technical report, National Advisory Committee for Aeronautics, 1922.

P. Beaudan and P. Moin. Numerical experiments on the flow past circular cylinders at sub-critical Reynolds numbers. Technical report, Thermosciences Division, Dept. of Mech. Engr., Stanford University, 1994.

M. Rahman, M. Karim, and A. Alim. Numerical investigation of the unsteady flow past a circular cylinder using 2-D finite volume method. *Journal of Naval Architecture and Marine Engineering*, 4:27–42, 2007.

C. J. Apelt. The steady flow of a viscous fluid past a circular cylinder at Reynolds Numbers 40 and 44. Aeronautical Research Council Reports and Memoranda 3175, Ministry of Aviation, London: Her Majesty's Stationary Office, October 1958.

B. N. Rajani, A. Kandasamy, and S. Majumdar. Numerical simulation of laminar flow past a circular cylinder. *Applied Mathematical Modelling*, 33:1228–1247, 2009.

S. Mayer, A. Garapon, and L. S. Sorensen. A fractional step method for unsteady free-surface flow with applications to non-linear wave dynamics. *International Journal for Numerical Methods in Fluids*, 28(2): 293–315, 1998.

G. Chapalain, R. Cointe, and A. Temperville. Observed and modeled resonantly interacting progressive water-waves. *Coastal Engineering*, 16(3):267–300, 1992.

R. L. Wiegel, K. E. Beebe, and J. Moon. Ocean wave forces on circular cylindrical piles. *Journal of Hydraulics Division, ASCE*, 124(1):89–113, 1959.

C. Guedes Soares. Representation of double-peaked sea wave spectra. *Ocean Engineering*, 11:185–207, 1984.

T. Stansberg and T. Kristiansen. Non-linear scattering of steep surface waves around vertical colums. *Applied Ocean Research*, 27(2):65–80, 2005.

J. M. J. Journee and J. Pinkster. *Introduction to Ship Hydrodynamics*. Delft University of Technology, 2002.